PONTIFÍCIA UNIVERSIDADE CATÓLICA
DO RIO DE JANEIRO

**Felipe Almeida da Silva**

# Optical tweezers and structured light: trapping microparticles in a dark focus

**Dissertação de Mestrado**

Dissertation presented to the Programa de Pós–graduação em Física of PUC-Rio in partial fulfillment of the requirements for the degree of Mestre em Física.

Advisor: Prof. Thiago Barbosa dos Santos Guerreiro

Rio de Janeiro
May 2023

**PONTIFÍCIA UNIVERSIDADE CATÓLICA**
DO RIO DE JANEIRO

**Felipe Almeida da Silva**

# Optical tweezers and structured light: trapping microparticles in a dark focus

Dissertation presented to the Programa de Pós–graduação em Física of PUC-Rio in partial fulfillment of the requirements for the degree of Mestre em Física. Approved by the Examination Committee:

**Prof. Thiago Barbosa dos Santos Guerreiro**
Advisor
Departamento de Física PUC-Rio

**Prof. Antonio Zelaquett Khoury**
UFF

**Dr. Cyril Laplane**
Macquarie University

**Prof. Gabriel Horacio Aguilar**
UFRJ

**Prof. Walter Margulis**
CETUC – PUC-Rio

Rio de Janeiro, May 10th, 2023

**Felipe Almeida da Silva**

The author graduated in Physics from Pontifícia Universidade Católica do Rio de Janeiro in 2020 with a Complementary Studies diploma in Mathematics.

To my parents, for their love and strength.
If it was hard for me, it was harder for them.

## Acknowledgments

Para agradecer aos principais responsáveis por toda a minha jornada, decidi escrever esta parte em português. Como grande parte dos brasileiros, meus pais não terminaram o ciclo básico de estudos e não aprenderam um segundo idioma. Mesmo assim me incentivaram desde criança a seguir o caminho que hoje resulta nesta dissertação.

Quero agradecer ao meu pai por ser um homem correto, resiliente e extremamente trabalhador. Agradeço a minha mãe pelo seu amor inigualável, pelos os atos de serviço, as orações, por todos beijos, abraços e conselhos. Meus pais fizeram tudo o que puderam para que eu e meu irmão tivéssemos mais escolhas do que eles tiveram e me enche de orgulho poder dedicar este trabalho a eles.

Eu também agradeço ao meu irmão por todos os momentos em que estivemos juntos. Um dia a gente não vai mais dividir o mesmo quarto e eu vou sentir muito a sua falta.

Agradeço aos bons amigos que fiz durante a vida. Em especial, aos meus melhores amigos, Venancio e Galvão, que estão comigo desde o dia em que decidi fazer física. Eles acompanharam de perto os meus sonhos, os meus fracassos, os meus sucessos e os meus novos sonhos.

E falando em novos sonhos, eu sou levado a pensar no grande amor da minha vida. Gisele tem papel fundamental em toda a minha trajetória na física. Com ela eu dividi todas as minhas inseguranças e medos. Ela me incentivou a persistir quando eu estava quase destindo da graduação. Ela esteve comigo em todos os momentos. E certamente também estará nos próximos.

Quero agradecer aos meus amigos de laboratório: os que já se formaram e os que estão comigo todos os dias. Obrigado por toda a ajuda e companherismo. Eu fiz grandes amigos trabalhando no laboratório, eu me senti querido aqui e jamais vou esquecer tudo isso.

Por fim, quero agradecer ao meu professor, orientador, paraninfo e grande amigo, Thiago. Sem exigir nada, ele me recebeu no laboratório e confiou em mim há quatro anos atrás. Eu não sabia nada sobre eletromagnetismo, mecânica quântica, parafusos, porcas, eu não sabia falar inglês e nem mesmo a nota mínima para fazer Iniciação Científica eu tinha. O Thiago foi o primeiro físico a acreditar em mim e muitas vezes as pessoas só precisam de alguém que acredite nelas.

## Abstract

Almeida da Silva, Felipe; Barbosa dos Santos Guerreiro, Thiago (Advisor). **Optical tweezers and structured light: trapping microparticles in a dark focus**. Rio de Janeiro, 2023. 88p. Dissertação de Mestrado – Departamento de Física, Pontifícia Universidade Católica do Rio de Janeiro.

Optomechanics, the study of light-induced forces upon matter, has seen tremendous advances in recent years with broad implications to all natural sciences. Optical tweezers, for instance, are now widely used in physics, chemistry and biology to trap nano- and micro-objects with a refractive index greater than of its surrounding medium using typically Gaussian laser beams. Generalizing these techniques, recent works began to explore higher-order states of the electromagnetic field and its superpositions for optical trapping, creating beams with customized phase, mode and amplitude. These new degrees of freedom allows for optical potentials beyond the harmonic approximation, enabling virtually arbitrary potential forms and even time-dependent forces capable of inducing controlled motion on the trapped object. Within this context of structured light beams, we can explore not only the attractive forces between light and matter but the repulsive ones that arise when the particle's refractive index is smaller than that of its medium. In this work we explore both scenarios by creating holographic beams with a Spatial Light Modulator (SLM). Specifically, we focus on the implementation of the dark focus beam, or optical bottle beam, where particles may find equilibrium in a region with no incidence of light. Experimental results are presented and compared to Lorentz-Mie numerical simulations and possible applications of these inverted optical tweezers in optomechanics and biology are discussed.

## Keywords

Optomechanics;    Optical tweezer;    Structured light.

# Resumo

Almeida da Silva, Felipe; Barbosa dos Santos Guerreiro, Thiago. **Pinças ópticas e luz estruturada: aprisionando micropartículas em um foco escuro**. Rio de Janeiro, 2023. 88p. Dissertação de Mestrado – Departamento de Física, Pontifícia Universidade Católica do Rio de Janeiro.

Optomecânica, o estudo de forças induzidas pela luz sobre a matéria, teve grandes avanços nos últimos anos com diversas implicações sobre todas as ciências naturais. Pinças ópticas, por exemplo, são amplamente usadas na física, química e biologia para aprisionar nano e micropartículas com índice de refração maior do que o meio que a cerca usando, em geral, feixes Gaussianos. Generalizando essa técnica, trabalhos recentes começaram a explorar estados de ordem maior dos feixes eletromagnéticos e suas superposições para aprisionamento óptico, criando feixes com fase, modo e amplitude ajustáveis. Esses novos graus de liberdade permitem o uso de potenciais arbitrários e até mesmo forças dependentes do tempo capazes de induzir movimento controlado no objeto aprisionado. Nesse contexto de feixes estruturados, nós podemos explorar não apenas as forças atrativas entre luz e matéria, mas também as forças repulsivas que ocorrem quando o índice de refração da partícula é menor que o do meio circundante. Neste trabalho vamos explorar ambos cenários a partir da criação de feixes holográficos com um Modulador Espacial de Luz (SLM). Mais especificamente, vamos focar na implementação do feixe de foco escuro, ou feixe de garrafa, onde as partículas encontram equilíbrio em uma região sem incidência de luz. Resultados experimentais são apresentados e comparados com simulações numéricas baseadas na teoria de Lorentz-Mie e possíveis aplicações dessas pinças óticas inversas são discutidas em optomecânica e biologia.

## Palavras-chave

Optomecânica;    Pinça ótica;    Luz estruturada.

# Table of contents

# List of figures

# List of tables

*Viver é partir, voltar e repartir.*

**Emicida**, *Trecho da música É Tudo Pra Ontem.*

# 1
# Introduction

## Optical tweezers

One of the greatest scientific discoveries of all time is that light carries momentum as first experimentally demonstrated in the early 1900s [1]. Moreover, later experiments proved that light can transfer both linear and angular momentum even to macroscopic objects [2], opening a new horizon to the study of radiation pressure forces.

With the advent of laser technology in the 1960s, the study of radiation pressure using coherent light beams became straightforward and a pioneer in this field was the 2018 Nobel laureate Arthur Ashkin. He has demonstrated that a focused laser beam can be used to confine dielectric micrometer particles, first with a pair of counter-propagating beams [3] and later with a single-beam gradient force [4, 5]. His works extended to the optical trapping of atoms [6], which inspired future works on laser cooling [7], and the first observation of optical levitation in air and vacuum [8] that evolved into an entire research field called levitodynamics [9].

The confinement of dielectric particles with light became known as optical tweezers and since then, it has found many applications in a variety of scientific fields as biology, also pioneered by Ashkin with his works manipulating bacteria and single cells [10, 11]. Several works have been done analyzing the physical properties of cell membranes [12–15] that can help to create a correlation between healthy and unhealthy cells, contributing to a better understanding of human diseases as malaria and cancer, with a potential role in the detection and diagnosis of human diseases [16].

Optical tweezers have also been widely used in physics as force sensors [17–20] and to study quantum interactions between light and matter in well-isolated systems [21–24]. The ability to control the motion of mechanical modes through interaction with light is the main feature of the optomechanics field.

**Structured light**

Beyond the intrinsic momentum, light has also other degrees of freedom such as amplitude, phase and polarization. The ability to control these features is a recent topic of research referred to as structured light [25]. One of the first implemented methods to modulate the phase of an incident beam was by using spiral phase plates [26], that despite creating helicoidal wavefronts were not designed to divide modulated and non-modulated beams.

Holography techniques, as first established by the 1971 Nobel Prize laureate Dennis Gabor, even before the invention of the laser [27], is a more general way to customize the phase and amplitude of an optical mode, with no intermediate material or specific production step. The introduction of liquid crystal spatial light modulators (SLM) offered real-time amplitude and phase control by computer-generated holograms. Since then, spatial degrees of freedom have been exploited in superpositions between different optical modes to generate two-dimensional intensity patterns in the transversal plane of an optical beam, typically in the focal plane. Some approaches combine the phase modulators with the independent customization of polarization enabling three dimensional control of the electric field, known as fully-structured light fields [28].

**This work**

In the last few years, huge progress has been done by combining beam shaping with optical trapping [29], opening up novel possibilities to study the interaction between light and matter in liquid environments or vacuum. Beyond the standard optical tweezers, structured light beams can induce controllable motion and create time-dependent optical potentials ruling the dynamics of micro- and nanoparticles [28].

Rotation of these tiny objects due to the transfer of angular momentum is also of great interest, because of its potential applications such as optically driven micromachines or motors [29]. In addition to spin angular momentum (SAM) carried by beams with circularly polarized light one can, for instance, induce orbital angular momentum (OAM) with annular intensity beams [30–32] to a birefringent particle, causing them to rotate about its own axis as well as rotate about the trapping beam axis due to the helicoidal wavefronts of the trapping beam [33] .

In this dissertation, we will be concerned with creating, aligning, calibrating and measuring the properties of optical tweezers with structured light in

the regime of attractive and repulsive interactions.The content of this work was arranged as steps towards the first experimental implementation of a stable dark focus tweezer (DFT) [34], presented in Chapter 4.

We begin in Chapter 2 with a brief overview of the theory of laser beam propagation and its transverse modes, followed by an experimental protocol to create structured light beams with an SLM. We also introduce a formalism to understand how the exchange of momentum between light and matter can result in a gradient force.

In Chapter 3 we implement from scratch an optical tweezer setup that we use throughout this entire work. We discuss protocols to align and calibrate the optical tweezer and present some results with Gaussian and structured light modes. We work in the attractive forces regime, where the particle finds an equilibrium point in the brightest point of a laser beam, hence the name bright tweezers.

Finally, in Chapter 4 we introduce the DFT. We move to a repulsive forces regime where the particle is confined in a region with a dark focus surrounded by light in all directions as illustrated in Fig. 1.1. We discuss the viability of the experiment and then show the obtained results.

To conclude, in Chapter 5 we discuss possible future research directions with structured light tweezers for both, the bright and dark tweezers.
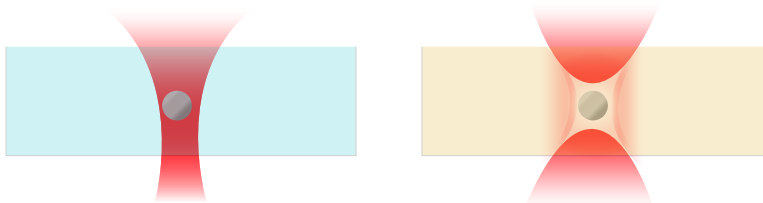


Figure 1.1: Schematic representation of the Gaussian and dark focus tweezer.

# 2
# An overview of structured light

The first step towards a structured light tweezer is understanding the physics behind laser beam propagation and its transverse modes, originating from the laws of electromagnetism. In this chapter, we present the wave propagation formalism in the paraxial (weak focusing) approximation and explain how it gives rise to the Hermite-Gauss (HG) and Laguerre-Gauss (LG) modes. We also describe the apparatus used to experimentally generate these modes and their linear combinations in the laboratory, the spatial light modulator. Finally, in the last section we introduce the optical forces arising from the exchange of momentum between light and particles that will be used throughout this thesis.

## 2.1
## Paraxial waves

The easiest way of thinking about light is by considering a bundle of thin arrows propagating linearly in the same direction in free space. This is the principal idea behind geometric optics. As we discover that light propagates according to a wave equation this heuristic idea falls apart and we need to consider the transverse profiles of a light beam. Consider the well-known wave equation for a fixed polarization vector,

$$\nabla^2 \boldsymbol{u} - \frac{1}{c^2}\frac{\partial^2 \boldsymbol{u}}{\partial t^2} = 0, \tag{2-1}$$

where $c = c_0/n_m$ represents the speed of light in a certain medium with refractive index $n_m$, $c_0$ is the speed of light in vacuum and $\boldsymbol{u}$ specifies the electric field profile according to $\vec{E} = \boldsymbol{u}\hat{\epsilon}$ for a given polarization vector $\hat{\epsilon}$. We will refer to the solutions of this equation, $\boldsymbol{u} = u(\vec{r}, t)$, as wavefunctions.

We assume the wavefunctions have a harmonic time dependence, i.e., they oscillate with a well-defined frequency $\omega$, hence the name *monochromatic light*. It is convenient to represent the wavefunction $\boldsymbol{u}$ in terms of a generic complex function $\boldsymbol{U} = U(\vec{r}, t) = R(\vec{r})e^{i\omega t}$ where $R(\vec{r})$ is the complex amplitude of the wave. Note that $\boldsymbol{u} = Re\{\boldsymbol{U}\} = \frac{1}{2}(\boldsymbol{U} + \boldsymbol{U}^\dagger)$ and we can always work with complex functions instead of their real counterparts, and take the real part whenever necessary. Substituting $U(\vec{r}, t)$ into the wave equation leads us to the

Helmholtz equation,
$$\nabla^2 U(\vec{r}, t) + k^2 U(\vec{r}, t) = 0, \tag{2-2}$$
where we have defined the wavenumber $k = \omega/c = 2\pi/\lambda$. Note that the wavenumber depends on the medium in which the wave is traveling and from now on we write $k_m = n_m \omega / c_0$.

We would now like to find out which restrictions are imposed by the wave equation, Eq. (2-2), upon the electric field's spatial distribution. Consider the ansatz,
$$R(\vec{r}) = A(\vec{r}) e^{-ikz}. \tag{2-3}$$
A theoretical idealization of electromagnetic waves are the plane waves, for which $A(\vec{r}) = A_0 e^{ik_x x + ik_y y}$. We can think of plane waves as infinite, constant wavefronts defined by the constant-phase plane $\phi = \vec{k} \cdot \vec{r}$. This idealization, despite being very convenient, does not exist in nature.

Although laser beams can have similarities to plane waves, their intensity profile varies in the radial direction as they propagate through space. Importantly, the energy distribution in the beam is not uniform unlike in plane waves. These differences between plane waves and what we will call paraxial waves is codified in the amplitude profile function $A(\vec{r})$, for which we now derive an equation. Substituting Eq. (2-3) into Eq. (2-2) leads to [35],
$$\frac{\partial^2 A(\vec{r})}{\partial x^2} + \frac{\partial^2 A(\vec{r})}{\partial y^2} + \frac{\partial^2 A(\vec{r})}{\partial z^2} - 2ik \frac{\partial A(\vec{r})}{\partial z} = 0. \tag{2-4}$$
We assume $A(\vec{r})$ varies slowly along the beam propagation, which means that for a small distance $\Delta A(\vec{r}) = \frac{\partial A(\vec{r})}{\partial z} \Delta z$ where $\Delta z = \lambda$. We can write it as:
$$\frac{\partial A(\vec{r})}{\partial z} \lambda \ll A(\vec{r}) \tag{2-5}$$
and its derivative with respect to the $z$-direction can be used to simplify Eq. (2-4),
$$\frac{\partial^2 A(\vec{r})}{\partial z^2} \ll k \frac{\partial A(\vec{r})}{\partial z}, \tag{2-6}$$
to find the so-called paraxial Helmholtz equation for weak focusing beams,
$$\nabla_T^2 A(\vec{r}) - 2ik \frac{\partial A(\vec{r})}{\partial z} = 0, \tag{2-7}$$
where $\nabla_T^2 = \frac{\partial^2}{\partial x^2} + \frac{\partial^2}{\partial y^2}$ is the transverse Laplace operator.

From now on, we will refer to $A(\vec{r})$ as simply the electric field at a given polarization, $E(\vec{r})$. We will also be interested in the optical intensity of a laser beam, given by $I(\vec{r}) = \frac{n_m \epsilon_0 c}{2} |E(\vec{r})|^2$. As we will soon see, we are capable of experimentally generating arbitrary wavefunction profiles by superposing solutions of the paraxial Helmholtz equation.

## 2.2
## The Gaussian beam

The simplest solution of the paraxial wave equation, and one of the most common in optical applications, is the Gaussian Beam. The corresponding wavefunction reads,

$$E_{Gauss}(\rho, z) = E_0 \frac{\omega_0}{\omega(z)} \exp\left[\frac{-\rho^2}{\omega(z)^2}\right] \exp\left[ik_m z + ik_m \frac{\rho^2}{2R(z)} - i\zeta(z)\right], \quad (2\text{-}8)$$

where $R(z)$, $\zeta(z)$, $\omega_R$ and $\omega(z)$ are called wavefront radius, Gouy phase shift, Rayleigh length and beam width, respectively. These are given by,

$$R(z) = z\left(1 + \frac{z_R^2}{z^2}\right), \quad (2\text{-}9\text{a})$$

$$\zeta(z) = \arctan\left(\frac{z}{z_R}\right), \quad (2\text{-}9\text{b})$$

$$\omega(z) = \omega_0 \sqrt{1 + \frac{z^2}{z_R^2}}, \quad (2\text{-}9\text{c})$$

$$z_R = \frac{\pi \omega_0^2}{\lambda_m}. \quad (2\text{-}9\text{d})$$

Figure 2.1 shows a representation of the Gaussian beam, with special emphasis on the beam width $\omega(z)$. The width has a minimum value, namely the beam waist $\omega_0$, right at the origin of our coordinate system. The Rayleigh length $z_R$ defines the range over which the transverse extent of the beam remains approximately constant, also known as depth of the focus, painted blue in Fig. 2.1. For $z \gg z_R$, the beam width can be approximated as $\omega(z) \approx \frac{\lambda_m}{\pi \omega_0} z$ and its linear coefficient is called numerical aperture (NA),

$$\text{NA} = \frac{\lambda_m}{\pi \omega_0}. \quad (2\text{-}10)$$

The optical intensity of a monochromatic Gaussian beam is given by,

$$I_{Gauss}(\rho, z) = I_0 \frac{\omega_0^2}{\omega(z)^2} \exp\left[-\frac{2\rho^2}{\omega(z)^2}\right], \quad (2\text{-}11)$$

where we define $I_0 = \frac{n_m \epsilon_0 c}{2}|E_0|^2$ The Gaussian intensity distribution can be seen in Fig. 2.2a). The intensity is maximum at the central point at a beam waist distance from the origin $r = \omega_0$ decreases by a factor of $1/e^2$.
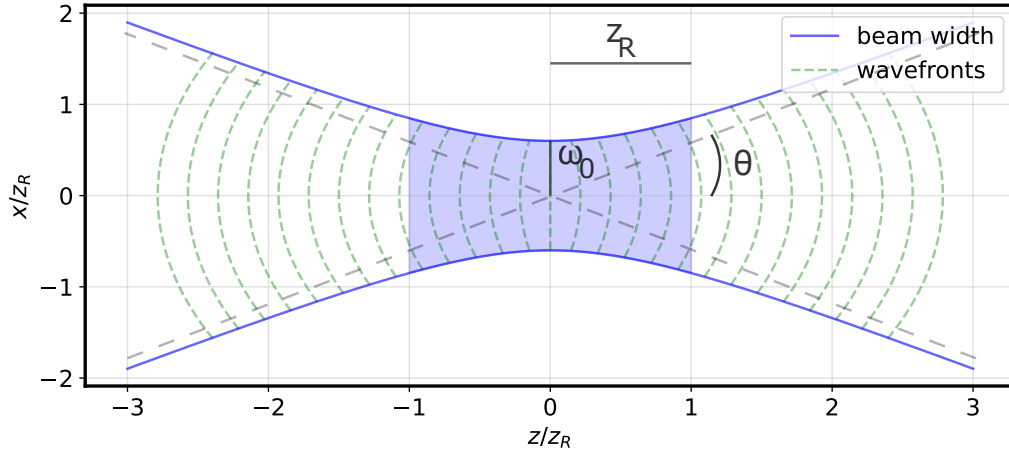
Figure 2.1: Schematic representation of Gaussian beam propagation.

## 2.3
## Higher-order modes

### 2.3.1
### Laguerre-Gauss modes

Laguerre–Gaussian (LG) modes are a set of solutions to the paraxial wave equation in cylindrical coordinates, and are the main modes of the electromagnetic field studied in this work. Their nomalized transverse profiles present rotational symmetry along the axial direction and are defined as,

$$
\begin{aligned}
E_{p,\ell}^{LG}(\rho,\phi,z) =& E_0 \frac{\omega_0}{\omega(z)} \exp\left[-\frac{\rho^2}{\omega(z)^2}\right] \exp\left[ik_m z + ik_m \frac{\rho^2}{2R(z)} - i\zeta(z)\right] \\
& \left(\sqrt{2}\frac{\rho}{\omega(z)}\right)^{|\ell|} L_p^{|\ell|}\left(\frac{2\rho^2}{\omega(z)^2}\right) \exp\left[-i(2p+\ell)\zeta(z)\right] \exp\left[i\ell\phi\right],
\end{aligned}
$$

(2-12)

where $L_p^{|\ell|}$ are the associated Laguerre polynomials, indexed by a non-negative integer $p$ and an azimuthal integer $l$. The first Laguerre polynomials are,

$$L_0^l(x) = 1,$$ (2-13a)

$$L_1^l(x) = -x + \ell + 1,$$ (2-13b)

$$L_2^l(x) = \frac{x^2}{2} - (\ell+2)x + \frac{(\ell+1)(\ell+2)}{2},$$ (2-13c)

$$L_3^l(x) = \frac{-x^3}{6} + \frac{(\ell+3)x^2}{2} - \frac{(\ell+2)(\ell+3)x}{2} + \frac{(\ell+1)(\ell+2)(\ell+3)}{6}.$$ (2-13d)

An interesting property of the LG modes is their intrinsic rotational orbital angular momentum (OAM) of $\ell\hbar$ per photon associated with the phase term $\exp(i\ell\phi)$. For $\ell \neq 0$, the electric field presents an inclined wavefront in the axial direction [29, 36], which can be absorbed by objects placed along the propagation axis and hence experiencing a torque. A rotating trapped particle, for instance, can find applications in driven motors and biology experiments and will be discussed in the Chapter 3. Note that this orbital angular momentum is different from the angular momentum acquired due light's polarization, referred to as spin angular momentum (SAM) [37]. A beam of circularly polarized light carries a value of $\pm\hbar$ per photon where the sign depends on its handedness.

The optical intensity of LG modes is,

$$I_{p,\ell}^{LG}(\rho,\phi,z) = I_0 \frac{\omega_0^2}{\omega(z)^2} \exp\left[-\frac{\rho^2}{\omega(z)^2}\right] \left(\frac{2\rho^2}{\omega(z)^2}\right)^{|\ell|} \left[L_p^\ell\left(\frac{2\rho^2}{\omega(z)^2}\right)\right]^2, \qquad (2\text{-}14)$$

and are plotted at the focal plane in Fig. 2.2, for different indices $p, \ell$.
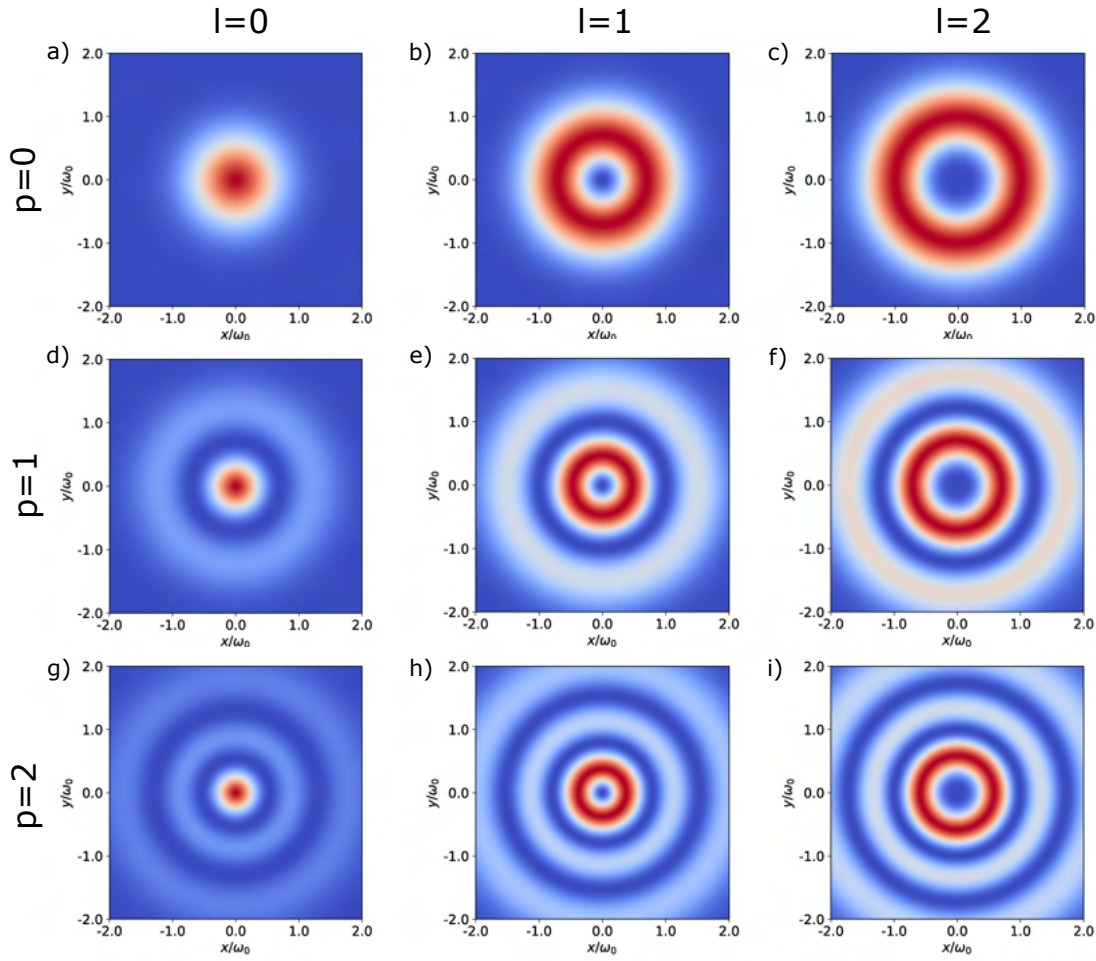
Figure 2.2: Intensity profiles of Laguerre-Gaussian modes at the focal plane for various indices $p, \ell$.

### 2.3.2
### Hermite-Gauss modes

Hermite-Gauss modes are another set of solutions of the paraxial wave equation in Cartesian coordinates. The associated wavefunctions are,

$$
E_{m,n}^{HG}(x, y, z) = E_0 \frac{\omega_0}{\omega(z)} \exp\left[-\frac{(x^2+y^2)}{\omega(z)^2}\right] \exp\left[ik_m z + ik_m \frac{(x^2+y^2)}{2R(z)} - i\zeta(z)\right]
$$
$$
H_m\left(\sqrt{2}\frac{x}{\omega(z)}\right) H_n\left(\sqrt{2}\frac{y}{\omega(z)}\right) \exp[-i(m+n)\zeta(z)],
$$

$$(2\text{-}15)$$

where $H_m$ and $H_n$ are the Hermite polynomials associated to the non-negative indices $m$ and $n$ determining the shape of the beam profile in the $x$ and $y$ directions, respectively. The first Hermite polynomials are,

$$
H_0(x) = 1,
$$

$$(2\text{-}16\text{a})$$

$$H_1(x) = x, \tag{2-16b}$$

$$H_2(x) = x^2 - 1, \tag{2-16c}$$

$$H_3(x) = x^3 - 3x. \tag{2-16d}$$

The optical intensity of a HG mode is,

$$I_{m,n}^{HG}(x,y,z) = I_0 \frac{\omega_0^2}{\omega(z)^2} \exp\left[-\frac{\rho^2}{\omega(z)^2}\right] H_m\left(\sqrt{2}\frac{x}{\omega(z)}\right)^2 H_n\left(\sqrt{2}\frac{y}{\omega(z)}\right)^2, \tag{2-17}$$

and the are plotted in the focal plane in Fig. 2.3 for different indices. We adopted $\rho^2 = x^2 + y^2$ for simplicity.
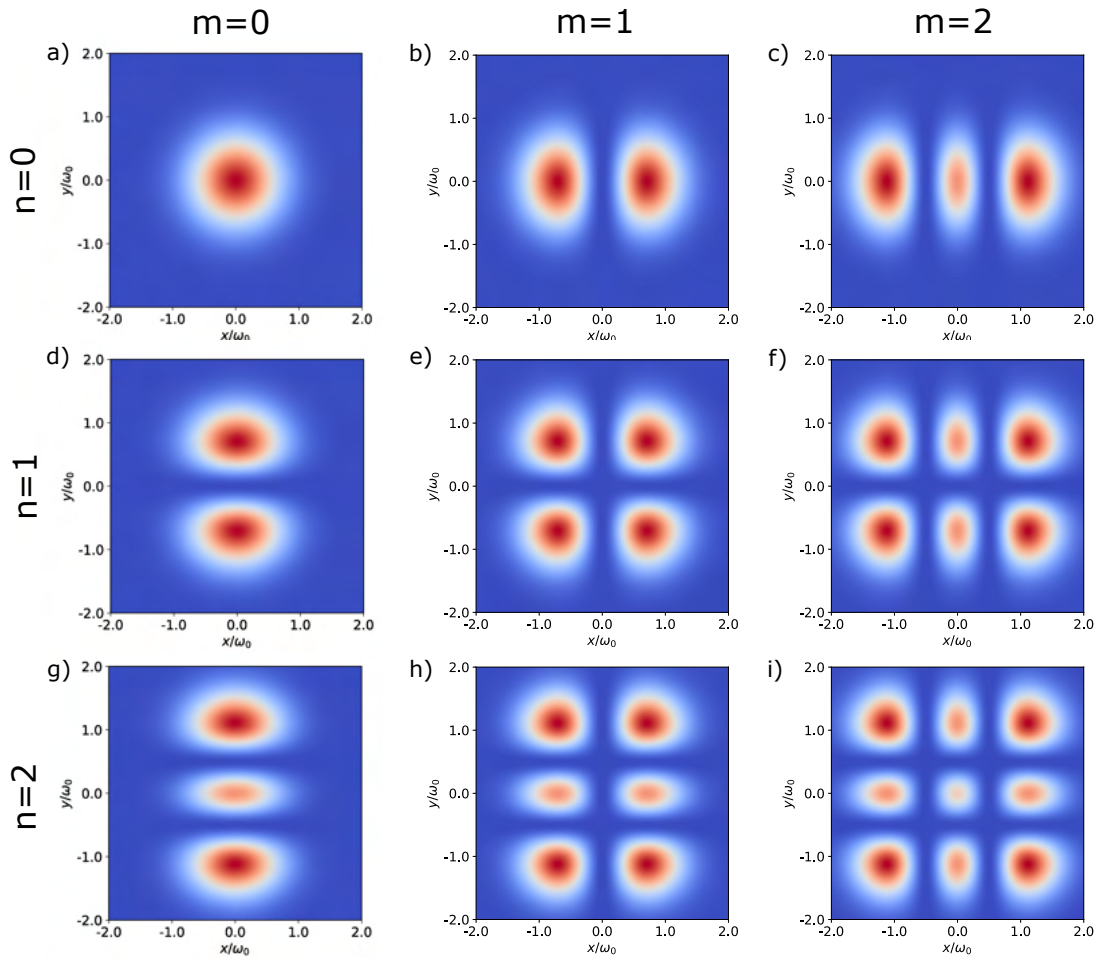


Figure 2.3: Hermite-Gaussian modes.

## 2.4
## Superpositions

Both the LG and HG sets of modes form a complete orthogonal basis of solutions for Eq. (2-7). Thus, any transverse light field profile can be written

as a linear combinations of elements of these basis. These superpositions will vary along the axial propagation direction, according to the phase evolutions of each of the individual modes [38].

In this section we briefly present an example of a specially engineered superposition that can be used in novel forms of optical trapping. In particular, we present the superposition used in the dark focus trapping experiment, as further discussed in Chapter 4, the Optical Bottle Beam.

### 2.4.1
### The Optical Bottle Beam (OBB)

The Optical Bottle Beam (OBB) is an example of superposition of two Laguerre-Gauss modes as first introduced by A. Arlt and M. Padgett [39]. Combining a Gaussian $LG_{0,0}$ and $LG_{p,0}$ modes with $p = 1$ or $p = 2$ with a relative phase of $\pi$ results in an optical beam with a dark central focus surrounded by a bright region in all directions, as a one can see in Fig. 2.4a) for an OBB with $p = 1$ and Fig. 2.4b) for $p = 2$.
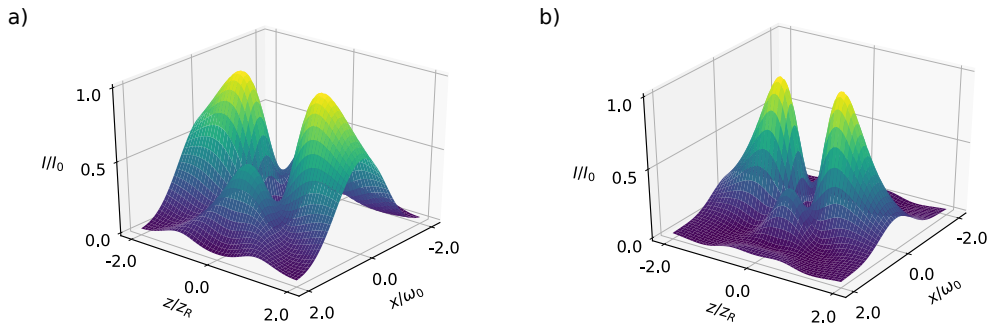
Figure 2.4: Intensity landscape in the $xz$ plane of the optical bottle beam for a) $p = 1$ and b) $p = 2$

The resulting electric field and the corresponding intensity for the OBB are,

$$
\begin{aligned}
E_{\text{OBB},p}(\rho, z) =& E_0 \frac{\omega_0}{\omega(z)} \exp\left[-\frac{\rho^2}{\omega(z)^2}\right] \exp\left[ik_m z + ik_m \frac{\rho^2}{2R(z)} - i\zeta(z)\right] \\
& \left[1 - L_p^0\left(\frac{2\rho^2}{\omega(z)^2}\right) e^{-i(2p+l)\zeta(z)}\right],
\end{aligned}
\tag{2-18}
$$

$$
\begin{aligned}
I_{\text{OBB},p}(\rho, z) =& I_0 \frac{\omega_0^2}{\omega(z)^2} \exp\left[-\frac{2\rho^2}{\omega(z)^2}\right] \\
& \left[1 - 2\cos\left(2p \arctan \frac{z}{z_R}\right) L_p^0\left(\frac{2\rho^2}{\omega(z)^2}\right) + L_p^0\left(\frac{2\rho^2}{\omega(z)^2}\right)^2\right].
\end{aligned}
\tag{2-19}
$$

The Gouy phase $\zeta(z)$ defines interference patterns in the intensity distribution of the resulting mode in Eq. (2-19). Figure 2.5 illustrates the dark region in the x and z-direction for $p = 1$ and $p = 2$. We define the width W and height W of the OBB as the distance between peaks of light intensity in the radial and axial directions, respectively. Direct calculation shows that these are given in terms of the beam waist as $W = 2\omega_0$, $H = 2z_R$ for $p = 1$ and $W = 2\sqrt{2 - \sqrt{2}}\omega_0$, $H = \sqrt{2}z_R$ for $p = 2$. Both plots in Fig. 2.4 consider a beam with numerical aperture NA= 0.6 propagating in the vacuum, $n_m = 1.0$.
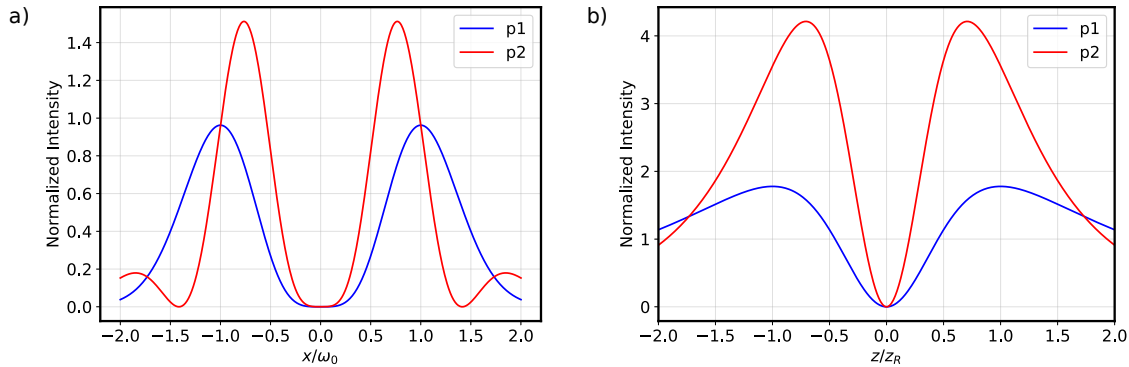


Figure 2.5: Intensity profiles of the optical bottle beam for a) $p = 1$ and b) $p = 2$.

## 2.5
## Experimental holographic beams

There are a variety of different techniques to produce higher modes of the electric field, such as spiral phase plates [26], metamaterials, digital mirror devices (DMD) and spatial light modulators [28, 29, 40]. In this work, we create HG and LG modes using a SLM (Pluto-NIR-015), an electronic device based on a nematic liquid crystal display able to induce phase modulation in an incident Gaussian beam. In this section we present a tutorial for aligning and calibrating the SLM, but first a small digression is made necessary, in order to understand certain practical laboratory notions such as collimated beams, thin lenses and telescopes.

## 2.5.1
## Collimated beams

As discussed in the previous sections, plane waves are not solutions of the paraxial equation and provide only an approximation in certain situations. However, geometric optics concepts are very useful in the laboratory. Consider, for instance, light propagating as a bundle of rays whose divergence angle $\theta$

can be so small such that $\sin\theta \approx \theta$. These are collimated light beams. Consider the thin lens equation,

$$\frac{1}{f} = \frac{1}{h} + \frac{1}{h'}, \qquad (2\text{-}20)$$

where $f$ is the lens' focal distance and $h$, $h'$ are the object's distance and image's distance from the lens, respectively. For an object placed exactly at the lens' focal distance, its image forms at infinity, meaning the light rays are parallel. In our experiments, we collimate laser beams by focusing at a very distant point, typically on the order of a few meters. We obtain a good approximation of a collimated beam by this procedure.

Figure 2.6a) illustrates this idea for a beam waist $\omega_0$ at the focal distance $f_1$ of a thin lens. The output beam is collimated and its size can be calculated according to the divergence angle $\theta_1$. Moreover, it can be extended to Gaussian parameters by considering the numerical aperture, Eq. (2-10),

$$\omega_c = f_1 \tan\theta_1 = \frac{f_1\lambda}{\pi\omega_0}. \qquad (2\text{-}21)$$

The output beam is then focused by a second lens at a distance $f_2$. Repeating the same calculation we find a relation between the image and the initial waist with magnification $M = f_2/f_1$,

$$\omega_o = f_2 \tan\theta_2 = \frac{f_2\lambda}{\pi\omega_c} = \frac{f_2}{f_1}\omega_0. \qquad (2\text{-}22)$$
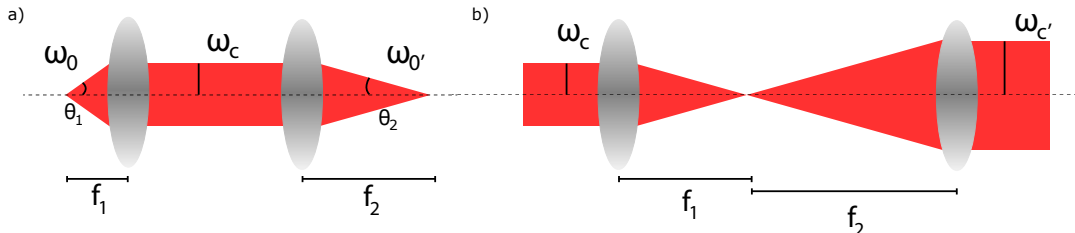


Figure 2.6: Geometric approximations in the laboratory. a) Transformation of beam waist by a pair of lenses. b) Magnification of a collimated laser beam.

Figure 2.6b) describes a telescope. An initially collimated beam is sent through a pair of lenses that are placed at a distance given by the sum of their focal lengths, $f_1 + f_2$. The output beam is increased (decreased) according to the values of $f_1$ and $f_2$,

$$\omega_c' = \frac{f_2}{f_1}\omega_c. \qquad (2\text{-}23)$$

From now on, these considerations concerning laser beams with small divergence angles, as well as collimated beams, will be used frequently throughout the next sections. A more detailed description of rays propagation in free space and their transformation by optical elements can be calculated using the ABCD matrix formalism [41].

### 2.5.2
### Spatial light modulator

The SLM employed in this work consists in an electronic display made of $1920 \times 1080$ pixels. Each pixel is an individually controllable cell made of liquid crystal. Liquid crystals are materials formed by a large number of randomly distributed rod-like molecules orientated along a fixed direction, a configuration known as the nematic phase The orientation of the molecules can be changed and reorganized by the application of an external electric field [42]. This induces a programmable birefringence in each pixel, enabling a spatial-dependent phase modulation of an impinging light field [43].

To formulate a mathematical model for the transformation $t(x, y)$ applied by the SLM, consider an incident optical mode $u_0 = A_0 \exp(i\phi_0)$, with $A_0 = A_0(x, y)$ and $\phi_0 = \phi_0(x, y)$ being the amplitude and phase of an incoming optical mode, respectively. A modulated beam $u_1 = A_1 \exp(i\phi_1)$ with $A_1 = A_1(x, y)$ and $\phi_1 = \phi_1(x, y)$ is obtained by applying the transformation $t(x, y)$ such that [44],

$$t(x, y) = \frac{A_1}{A_0} \exp \left( i \underbrace{(\phi_1 - \phi_0)}_{=\mathcal{P}_{ph}(x,y)} \right), \tag{2-24}$$

where we defined $\mathcal{P}_{ph}(x, y)$, the phase distribution applied to the incoming beam. As the SLM efficiency is never perfect, we add a diffraction grating pattern $\mathcal{P}_{dg}$ to divide modulated and non-modulated modes,

$$\mathcal{P}_{dg}(x, y) = \frac{2\pi}{\lambda}(x \sin \alpha + y \sin \beta), \tag{2-25}$$

where $\alpha$ and $\beta$ are the diffraction angles in $xz$ and $yz$ planes, respectively. Increasing the distance between diffracted beams avoids unwanted interference ensuring a good-quality mode. The resulting complete SLM transformation is then,

$$t(x, y) = \frac{A_1}{A_0} \exp \left( i(\mathcal{P}_{ph} + \mathcal{P}_{dg}) \right). \tag{2-26}$$

This transformation is set by using a LabVIEW script, whose graphic interface is shown in Fig. 2.7a). It allows us to configure the output radius, phase and mode of a horizontally polarized beam. The script calculates the phase pattern associated with Eq. (2-26) for the desired mode. Fig. 2.7b) shows an example of the calculated pattern $LG_{0,1}$ in the absence of grating ($\mathcal{P}_{dg} = 0$) and Fig. 2.7c) with grating for optimized operation. Both patterns were artificially colorized for better visualization
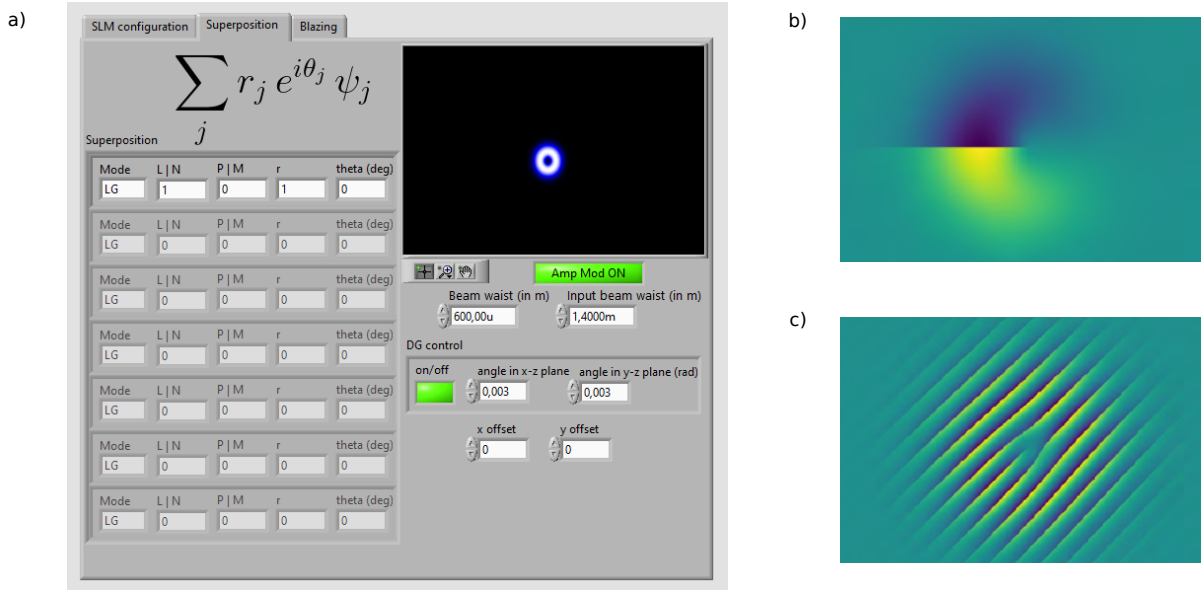
Figure 2.7: Labview script for beam modulation. a) SLM controller interface. b-c) Example of the calculated pattern displayed in the SLM screen. $LG_{0,1}$ phasing pattern is produced with b) no grating and c) grating pattern enabled.

### 2.5.3
### Calibrating the SLM

The proper operation of the LabVIEW script relies on a fine calibration procedure. A horizontally polarized Gaussian Beam impinges in the center of the SLM's screen with a small incidence angle $\theta_{inc}$, as close as possible to the normal, $\theta_{inc} \leq \pi/18$. The reflected beam $u_1(x, y)$ is then forwarded to a pair of lenses $f_1$ and $f_2$ in order to create a setup similar to a 4f imaging system [35] assuming $f_1 \neq f_2$. Hence, in addition to a magnification factor, the optical mode at a distance $2f_1 + 2f_2$ reads:

$$u_3(x, y) \propto u_1\left(-\frac{f_1}{f_2}x, -\frac{f_1}{f_2}y\right), \qquad (2\text{-}27)$$

where $u_3(x, y)$ is the resulting mode we shall analyze. In this work we use $f_1 = 20\,\text{cm}$ and $f_2 = 25\,\text{cm}$ creating a telescope with a magnification of 1.25. Fig. 2.8 illustrates the setup

As stated in the last subsection, the SLM is not 100% efficient. In the absence of a diffraction grating, the output beam is a mixture of a Gaussian beam and the required mode, both propagating in the same direction. By turning on the grating control, the zero-order of propagation is a Gaussian mode and the first order is the produced beam, whose deviation angle $\alpha$ and $\beta$, defined in Eq. (2-26), can be empirically adjusted in $xz$ and $yz$ planes, respectively. Calibrating these parameters is key to obtaining a well-defined mode. Wavefronts tend to interfere with other modes if a small deviation angle
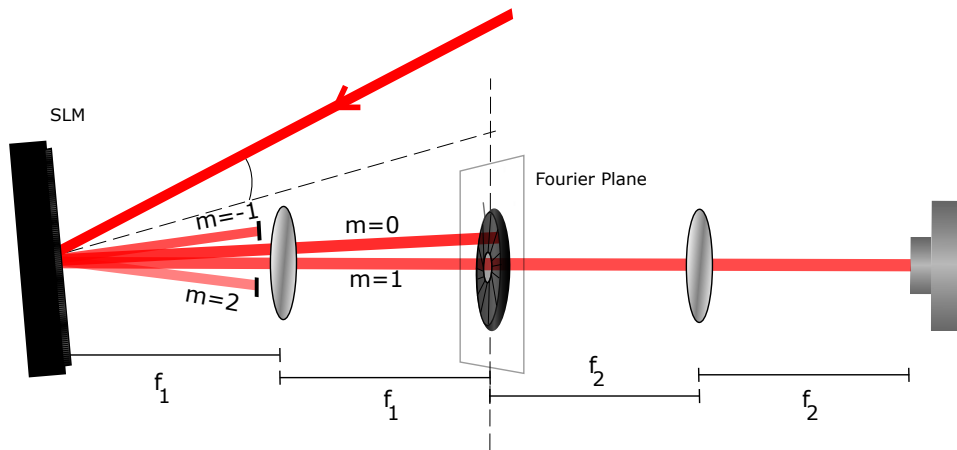
Figure 2.8: Schematic representation of the SLM's transformation

is chosen. Nevertheless, a high deviation angle creates a huge separation from the reflected and previously aligned Gaussian beam. Once the modulated beam was selected, an iris should be aligned at a distance $2f_1$ to create a spatial filter preventing unwanted interference between the modes. Finally, a blazing diffraction angle can be configured to improve the fraction of the total power that is transmitted for a specific order of propagation

### 2.5.4
### Visualizing patterns

A CCD camera is positioned at a distance of $2f_1+2f_2$ to inspect the beam's transverse profile, $|u_3(x,y)|^2$. Its quality is based on its expected distribution and symmetry. From now on all the calculated modes are artificially painted using the colormap "coolwarm" (predominantly light-blue, red) and all the experimental mode are shown in the scale "viridis" (predominantly blue, green and yellow).

In addition to being able to visualize the beam profile, we also want to know the properties of the modulated beam such as its beam waist $\omega_0$. To precisely know such parameters, it is essential to calibrate the pixels of the employed CCD camera in physical unties.

The calibration process consists of sending a laser beam to the CCD camera fixed at a translational stage with micrometer precision. We shift the position of the camera and save the respective image. The RGB levels associated with the colorful image are mapped in grayscale to obtain all the information and noise of each pixel in a single vector for each direction. We then fit a Gaussian distribution to the vector corresponding to each direction and save the mean value found in the curve fit. Fig. 2.9 shows this procedure for a certain

frame of a Gaussian beam.

a)



b)



c)
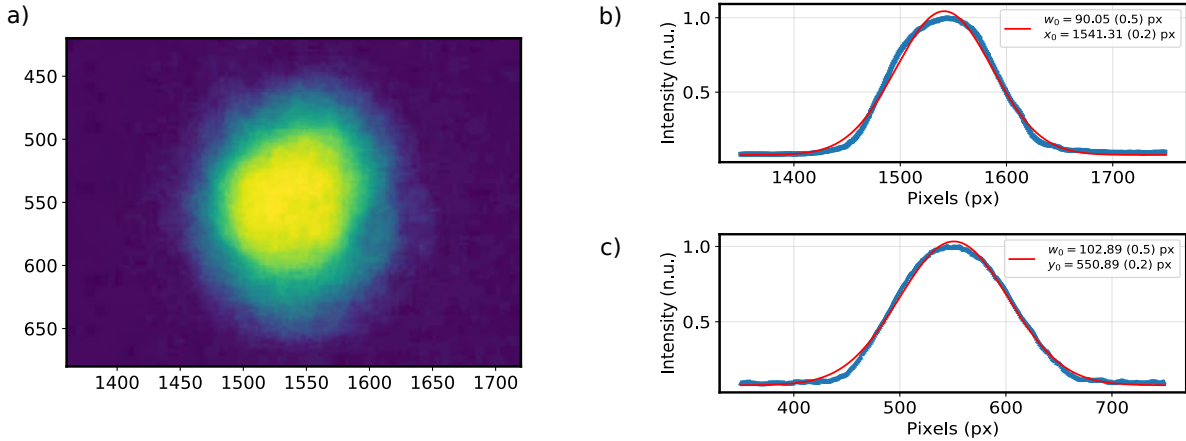


Figure 2.9: Curve fit for Gaussian beam. a) Experimental Gaussian beam. b-c) Curve fitting of b) $x$ and c) $y$ directions.

We then repeat this process for a few different positions and find a linear curve whose angular coefficient defines the conversion factor between pixels and our physical unit, say $\mu$m. We use two different cameras through this work, which we name CCD 01 (Image camera) and CCD 02 (Mode Monitor). We first calibrated CCD 02 starting from different positions in the propagation direction to be sure the value found was not affected by misalignment between the camera and the laser beam. The lines show the same conversion factor of $a_{CCD02} = (1.99 \pm 0.01)\,\mu$m/px for both experiments in which the initial position of the camera was shifted by $30\,$cm. CCD 01 is also characterized by the same procedure but shifting the magnified image of a trapped particle instead of a Gaussian beam's image. We found a factor $a_{x,CCD01} = 2.83\,\mu$m/px and and $a_{y,CCD02} = 2.80\,\mu$m/px, as shown in Fig. 2.10. These calibrations will be used in Chapters 3 and 4.

a)



b)
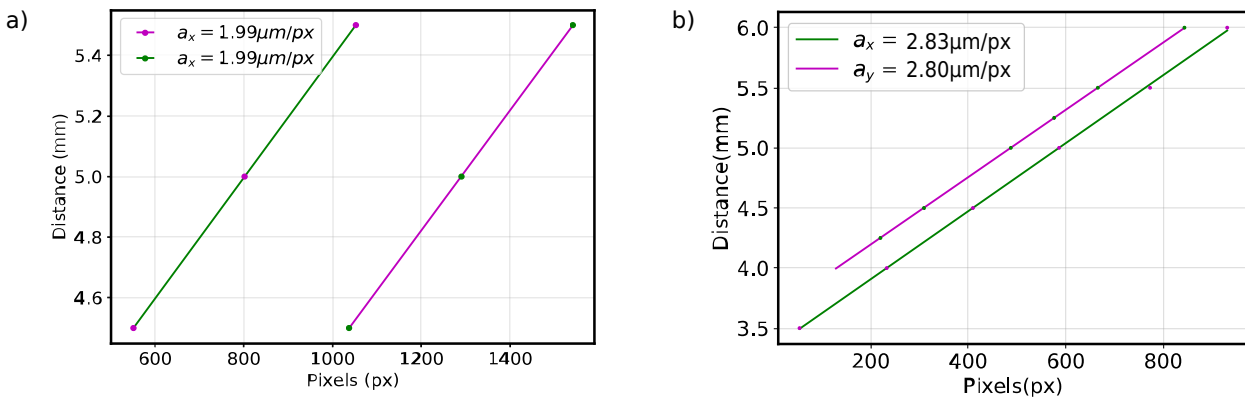


Figure 2.10: Pixel calibration for a) $a_{CCD02}$ and b) $a_{CCD01}$

With the camera properly calibrated, it is possible to evaluate the parameters of the beam. For example, Fig 2.9b-c) shows the beam waist
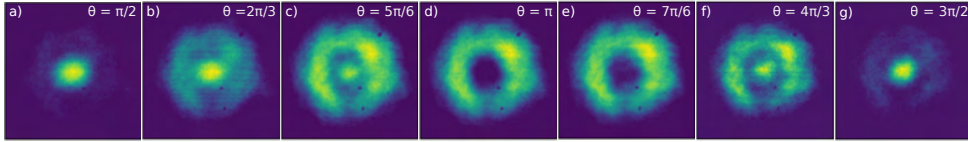
Figure 2.11: OBB experimental frames with $p = 1$.
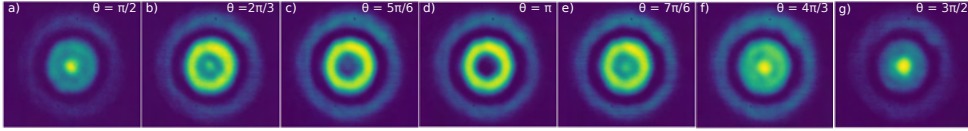


Figure 2.12: OBB experimental frames with $p = 2$.

$\omega_0$ fitted in pixels, which can now be converted to $\omega_{0,x} = (180.1 \pm 1.0)\,\mu$m and $\omega_{0,y} = (204.8 \pm 1.0)\,\mu$m. The modulated beam presents an asymmetry in both axes, with an aspect ratio of about 1.14. We now extend this procedure to calculate the beam profile of the OBB in its original focal point.

Fig. 2.11 and Fig. 2.12 show profiles of the experimental OBB produced using LG modes with $p = 1$ and $p = 2$, respectively. To simulate a beam translation in the axial direction, we vary the relative phase $\theta$ between the modes to mimic the intensity distribution near the focal plane. Fig. 2.13 shows the one dimensional intensity distribution in the dark focus plane (Fig.2.11d) and Fig. 2.12d)) for OBB with $p = 1$ in Fig. 2.11a) and $p = 2$ in Fig. 2.11b).
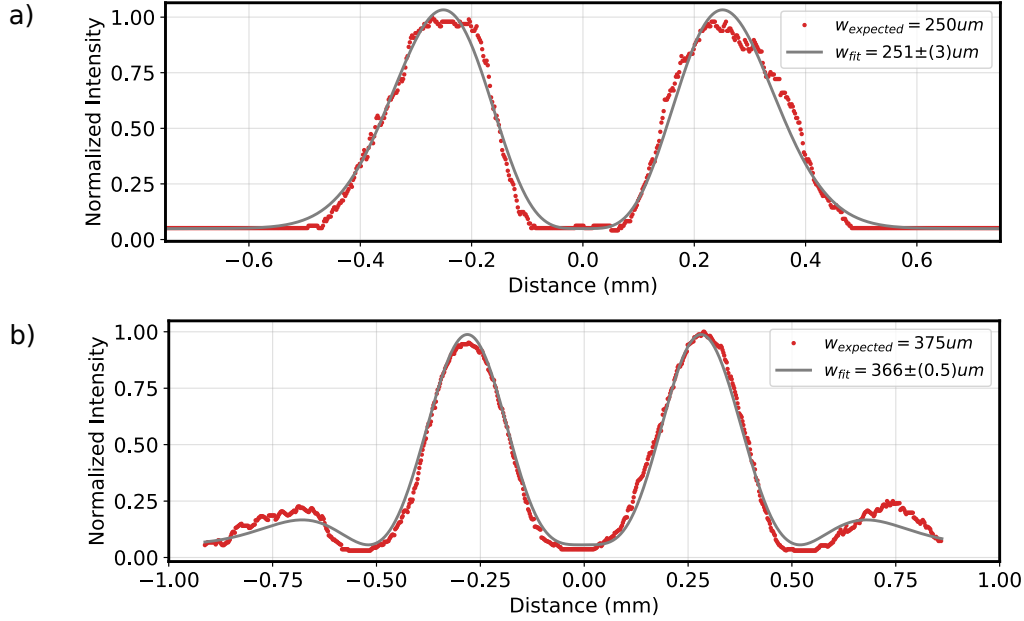
Figure 2.13: Intensity distribution in the dark focus plane for a) the OBB produced with and LG mode with $p = 1$ and b) $p = 2$.

## 2.6
## A bridge to optomechanics

Armed with the theory of laser beam propagation, we can finally move towards optomechanics. From a semi-classical point of view, a light beam with power $P$ carries $N = P/(pc)$ photons per second with momentum $\boldsymbol{p} = \hbar k \hat{\boldsymbol{u}}$ where $\hat{\boldsymbol{u}}$ is a unit vector indicating the beam propagation direction. In the absence of absorption, i.e., considering photons are elastically scattered by an object, the absolute magnitude of their momentum remains the same, by its direction can be changed. This results in a recoil force acting on the object. Suppose, for instance, an optical ray impinges with normal incidence on a particle and it its completely reflected backwards. Its total exchange of momentum per second is $-2N\boldsymbol{p}$ and hence, the recoil force applied on the particle is $\boldsymbol{F}_{ref} = 2P/c\ \hat{\boldsymbol{u}}$. In this section we explore the exchange of light's momentum with dielectric nanoparticles and discuss the conditions under which these optical forces can confine particles.

### 2.6.1
### Geometric optics approximation to optical forces

To generalize the normal incidence case, suppose a light beam $\boldsymbol{r_0}$ with power $P$ hits a dielectric sphere of radius $R$ at an angle of incidence $\theta$. Assume $R$ is much greater than the wavelength of the light $\lambda$, i.e., $R \gg 10\lambda$.

As illustrated in Fig. 2.14, part of the incident power is reflected, $PR$, and the remaining power is transmitted, $PT$, where $R$ and $T$ are the Fresnel reflection and transmission coefficients of the surface at angle $\theta$ [45]. We choose a material such that most of the beam is transmitted inside the sphere, $\boldsymbol{r_{t,0}}$, acquiring a new angle of propagation according to Snell's law. The ray $\boldsymbol{r_{t,0}}$ travels inside the object until it reaches the opposite boundary. At this point, most of the beam is transmitted again acquiring an angle $\alpha$ of propagation with relation to the incident beam. The reflected beam keeps traveling inside the sphere repeating the process until all light escapes from the sphere.
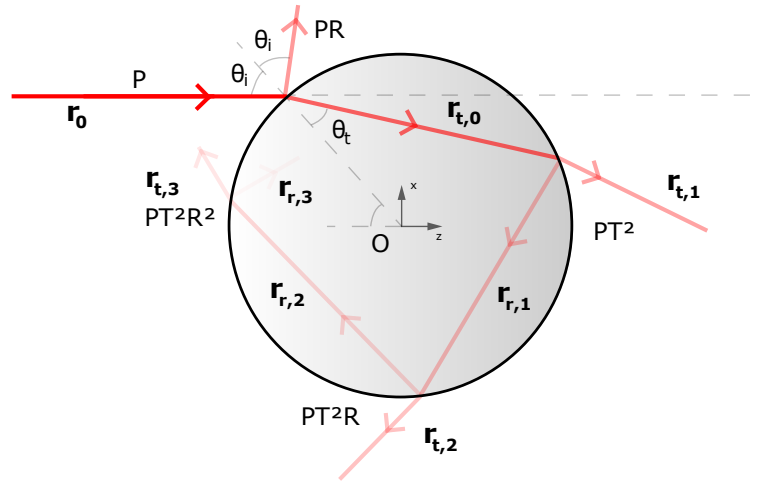


Figure 2.14: Geometry for evaluating the total forces acting on the sphere due a single incident ray.

The total force acting on the sphere due to this ray is [46]:

$$\boldsymbol{F}_{ray} = \frac{n_i P}{c}\hat{\boldsymbol{r}}_0 - \frac{n_i R P}{c}\hat{\boldsymbol{r}}_{r,0} - \sum_{n=0}^{\infty} \frac{n_i P T^2 R^n}{c}\hat{\boldsymbol{r}}_{t,n}, \qquad (2\text{-}28)$$

where $\hat{\boldsymbol{r}}_0$, $\hat{\boldsymbol{r}}_{r,0}$ and $\hat{\boldsymbol{r}}_{t,n}$ are the unit vectors representing the direction of $\boldsymbol{r_r}$, $\boldsymbol{r_{r,0}}$ and $\boldsymbol{r_{t,n}}$, respectively. $PT^2 R^n$ is transmitted power at each internal reflection $n$. All terms are proportional to the refractive index of the medium $n_i$ and it is written in order to state clearly that the momentum of the light beam inside the sphere does not matter for the total force calculation [46]. Although there are discussions on the definition of a photon's momentum inside a material – known as the Abraham–Minkowski dilemma [47] – we only measure the momentum difference between incident and outgoing photons, evaluated in the same medium.

The first two terms in Eq. (2-28) refer to the force applied in the particle due to the momentum exchange from the light beam. This pushes the particle on the direction of the beam propagation, and is thus called the scattering force, $\boldsymbol{F}_{scatt}$. The third term results in multiple transmissions. As $|T| < 1$, the

first terms in the summation are higher than the remaining ones, implying a stronger force in the $-\boldsymbol{r}_{t,1}$ and $-\boldsymbol{r}_{t,2}$ directions, pushing the particle in Fig. 2.14 upwards.

We can extend these ideas to a generic pair of converging rays, say $a$ and $b$, as illustrated in Fig.2.15. Let us ignore, for simplicity, the effects of surface reflection, say cosidering a perfectly transparent object. In that case, forces $F_a$ and $F_b$ are only due to refraction and point in the direction of momentum change. Fig. 2.15 shows a restoring force pulling the particle toward the focal point of the beam, assumed as the origin $O$ in the figure.
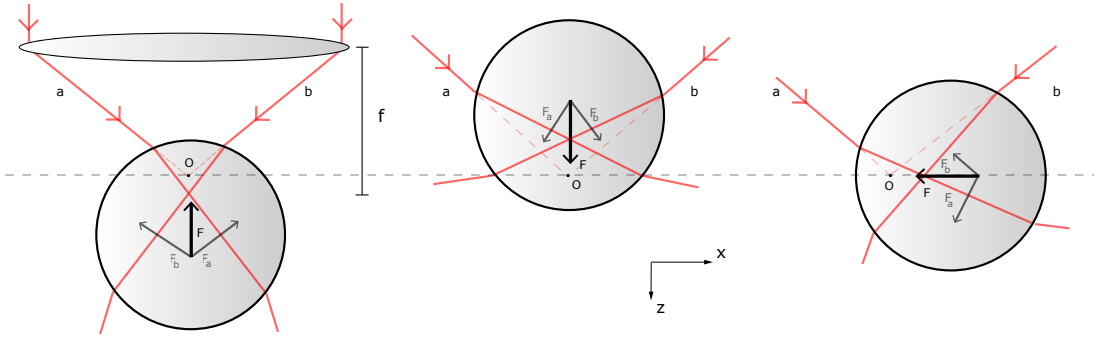


Figure 2.15: Qualitative view of the interaction between focused light and a dielectric sphere.

Note that, according to the definition given in Section 2.1, intensity is stronger in the focal point, due to the minimum size of the beam (for Gaussian beams this is the waist). The particle is then attracted to the maximum point of intensity of the laser beam [5].

This discussion provides us with a qualitative understanding of optical forces, but strictly speaking it is valid only in the geometric optics regime, when $R \gg \lambda$. To go beyond that, we need to consider the dipole regime, when the beam wavelength is much larger than the particle's radius.

### 2.6.2
### Dipole regime

When a dielectric particle with radius $R \ll \lambda/10$ is placed in an electric field, positive and negative charges $q$ are rearranged in an induced dipole, $\boldsymbol{p} = qd\hat{\boldsymbol{u}}$, where we suppose it can be approximated by two point charges of mass $m$ separated by distance $d$ and $\hat{\boldsymbol{u}}$ is a unit vector with its orientation. The equations of motion governing this situation are,

$$\frac{m}{2}\frac{d^2\boldsymbol{r}_+}{dt^2} = +q\operatorname{Re}\left\{\boldsymbol{E}(\boldsymbol{r}_+,t) + \frac{d\boldsymbol{r}_+}{dt} \times \boldsymbol{B}(\boldsymbol{r}_+,t)\right\},$$
$$\frac{m}{2}\frac{d^2\boldsymbol{r}_-}{dt^2} = -q\operatorname{Re}\left\{\boldsymbol{E}(\boldsymbol{r}_-,t) + \frac{d\boldsymbol{r}_-}{dt} \times \boldsymbol{B}(\boldsymbol{r}_-,t)\right\},$$

(2-29)

where we have defined $\boldsymbol{r}_+$ and $\boldsymbol{r}_-$ as the position vectors of positive and negative charges, respectively. As usual, the electric and magnetic fields are $\boldsymbol{E}$ and $\boldsymbol{B}$, respectively.

Summing both equations enables us to find the equation of motion for the center of mass coordinate $\boldsymbol{r}_d = \frac{\boldsymbol{r}_+ + \boldsymbol{r}_-}{2}$. As the particle is much smaller than the wavelength, we can expand both fields in Taylor series up to first order, obtaining [45, 48],

$$\boldsymbol{E}(\boldsymbol{r}_\pm, t) \approx \boldsymbol{E}(\boldsymbol{r}_d, t) + ((\boldsymbol{r}_\pm - \boldsymbol{r}_d) \cdot \nabla)\boldsymbol{E}(\boldsymbol{r}_d, t),$$
$$\boldsymbol{B}(\boldsymbol{r}_\pm, t) \approx \boldsymbol{B}(\boldsymbol{r}_d, t) + ((\boldsymbol{r}_\pm - \boldsymbol{r}_d) \cdot \nabla)\boldsymbol{B}(\boldsymbol{r}_d, t).$$

By substituting these expressions in the equation of motion for the center of mass, we find

$$m\frac{d^2\boldsymbol{r}_d}{dt^2} = (\boldsymbol{p} \cdot \nabla)\boldsymbol{E}(\boldsymbol{r}_d, t) + \frac{d\boldsymbol{p}}{dt} \times \boldsymbol{B}(\boldsymbol{r}_d, t) + \frac{d\boldsymbol{r}_d}{dt} \times (\boldsymbol{p} \cdot \nabla)\boldsymbol{B}(\boldsymbol{r}_d, t). \quad (2\text{-}30)$$

For non-relativistic dipoles, the third term can be neglected. We average the resulting equation to neglect terms oscillating much faster than the dipole's natural frequency. Under these approximations, the equation of motion for a dielectric particle subject to optical forces becomes,

$$m\frac{d^2\boldsymbol{r}_d}{dt^2} = \frac{\text{Re}\{\alpha\}}{4}\nabla|\boldsymbol{E}_i(\boldsymbol{r}_d)|^2 + \frac{k_0 \text{Im}\{\alpha\}}{2\epsilon_0 c}\text{Re}\left\{\boldsymbol{E} \times \frac{\boldsymbol{B}}{\mu_0}\right\} - \frac{ck_0 \text{Im}\{\alpha\}}{4\epsilon_0}\nabla \times \boldsymbol{s}_d$$
$$(2\text{-}31)$$

where we have introduced the real and imaginary polarizability of the particle, $\alpha$, also known in the static limit as the Clausius-Mossotti relation, $\alpha_{\text{CM}} = 4\pi\epsilon_0 R^3(n_R^2 - 1)/(n_R^2 + 2)$ [49]. The polarizability appears here as a proportionality constant to the electric field, $\boldsymbol{p} = \alpha\boldsymbol{E}$, and it acquires a correction due to the dipole's response to the oscillating field. This is known as the radiative reaction correction [46], and it reads,

$$\alpha \approx \alpha_{\text{CM}}\left\{1 - i\frac{k_0^3\alpha_{\text{CM}}}{6\pi\epsilon_0}\right\}^{-1}. \quad (2\text{-}32)$$

We have also introduced the time-averaged spin density of the incoming wave, $\boldsymbol{s}_d$. This component is associated with the angular momentum of light due to polarization gradients, SAM,

$$\boldsymbol{s}_d = i\frac{\epsilon_0}{2\omega}\boldsymbol{E} \times \boldsymbol{E}^\dagger. \quad (2\text{-}33)$$

As we are concerned only with linear polarized beams, the spin-curl force will not be further discussed.

Finally, it is possible to associate the first two terms in Eq. (2-31) with the

gradient and scattering forces, respectively. The first term is proportional to the optical intensity gradient of a laser beam and the second term is proportional to the Poynting vector, that by definition points in the propagation direction of an the electromagnetic wave. We define the particle-medium refractive index ratio $m = n_p/n_m$, which plays a major role in the next chapters as it determines the sign of the gradiend and scattering optical forces.

The final expressions for the scattering and gradient forces are,

$$\boldsymbol{F}_{scat}(\boldsymbol{r}) = \hat{\boldsymbol{z}}\frac{128\pi^5 R^6}{3c\lambda^4}\left(\frac{m^2-1}{m^2+2}\right)^2 n_m^5 I(\boldsymbol{r}), \qquad (2\text{-}34)$$

$$\boldsymbol{F}_{grad}(\boldsymbol{r}) = \frac{2\pi n_m R^3}{c}\left(\frac{m^2-1}{m^2+2}\right)\nabla I(\boldsymbol{r}), \qquad (2\text{-}35)$$

Since the gradient force is conservative, we can define the optical potential:

$$V(\boldsymbol{r}) = -\frac{2\pi n_m R^3}{c}\left(\frac{m^2-1}{m^2+2}\right)I(\boldsymbol{r}). \qquad (2\text{-}36)$$

This equation states a linear relation between the optical potential of a laser beam and the mechanical energy of a conservative force field. When a tiny particle is nearby the local maximum of an optical mode, such as a Gaussian beam, it is pulled towards the focal point. To confine such particle in a stable optical trap, the local maxima have to be $|V_{0,min}| \gtrsim 10K_0$ [41] where $K_0 = 3k_B T/2$ is the average kinetic energy of a particle in thermal equilibrium with its surrounding medium. In the next chapter we will explore optical potentials not only in the Gaussian mode but for all possible two-dimensional structured light intensity distributions at the focal point.

### 2.6.3
### Generalized Lorenz-Mie theory

So far we have discussed optical forces in two extreme regimes where their expressions assume simplified forms, namely the geometric optics and dipole regimes. Instead, for particles with sizes comparable to the wavelength of the laser beam, $R \approx \lambda$, none of the above descriptions holds true and we need to use the so-called Generalized Lorenz-Mie theory. The optical forces and torques are results of the transfers of momentum and angular momentum from the electromagnetic field to the particle, being essentially a problem of computing the light scattering patterns of outgoing fields given the input patterns. A full discussion of the general scattering problem and the Maxwell stress tensor that describes the interaction of light and matter can be found in Ref. [46].

In this work, we are concerned with numerical solutions to this problem. Assuming the response of the trapped particle is linear with the scattered field,

i.e. the material has no gain or nonlinear optical properties, the relationship between the incident and scattered fields must be linear, allowing a simple matrix equation $\boldsymbol{P} = \boldsymbol{T}\boldsymbol{A}$, where $\boldsymbol{P}$ and $\boldsymbol{A}$ represent the outgoing and incoming fields, respectively, and the T-matrix $\boldsymbol{T}$ carries the information on the physical properties of the particle and the light wavelength. This way, we only need to calculate $\boldsymbol{T}$ once for a given geometry of the trapped object [50]. Force and torque fields are then calculated as a function of position within the tweezer. In the following chapters we use the OTT toolbox developed in Ref. [50] to perform these calculations with microparticles.

# 3
# Bright Tweezers

Highly focused laser beams can be used to trap and hold tiny dielectric particles. The so-called optical tweezers, or Gaussian tweezers as we will refer to, have many applications due to their use as force sensors [18–20]. To perform all of these tasks it is essential to perfectly align the laser beam within a high numerical aperture lens and determine the force exerted by the light on a trapped particle. By using a Gaussian beam whose Taylor expansion implies in a quadratic polynomial intensity, we can model the potential applied to the trapped particle as harmonic. Due to the randomness introduced by the medium, the spring constant is usually obtained by measuring statistical quantities associated to the particle's displacements so one needs to be able to record it as a function of time.

In this chapter we describe the implementation of an optical tweezer setup from scratch, capable of trapping dielectric particles in a liquid medium. We describe the alignment process and two independent calibration methods based on high and slow sampling frequency detectors, the power spectrum density (PSD) and the potential analysis, respectively. Moreover, we introduce the SLM to apply a variety of structured light tweezers relying on the attractive force of the light when the particle is inside a medium with a smaller refractive index, $n_p > n_m$. To join all those types of optical tweezers we coin the name bright tweezers.

## 3.1
## Experimental setup

The experimental setup for generating a Gaussian tweezer can be seen in Fig. 3.1. A 780 nm CW laser (Toptica DL-pro) pumps a tapered amplifier (Toptica BoosTa) yielding a linear polarized beam in the output of a single-mode, polarization maintaining high-power optical fiber with an approximate total power of 1.5 W. The output beam is collimated by an aspheric lens and passes through a half-wave plate, $(\lambda/2, 1)$, and a polarizing beam splitter (PBS), PBS1. The transmitted beam is horizontally polarized and passes trough a second half-wave plate $(\lambda/2, 2)$. The beam is then modulated by the SLM and is sent trough a pair of lenses of focal lenghts $L1 = 20$ cm and $L2 = 25$ cm; these

lenses preserve the SLM transformation and serve the purpose of magnifying the generated mode by a factor of 1.25. The laser beam is divided by a second PBS (PBS2) in which the reflected signal is directed to the optical trap and the transmission is sent to a CCD (Mode Monitor) for imaging the modulated beam and performing stability measurements of the structured light mode.

The reflected beam is sent through an oil immersion objective, (OBJ1, Olympus UPlanFLN 100x adjustable NA = 0.6 - 1.3) of focal length $f_{OBJ1} = 1.8\,\mathrm{mm}$. The beam is focalized inside the sample. In this chapter we use $SiO_2$ beads of radius $R = 575\,\mathrm{nm}$ (microParticles GmbH) with refractive index $n_p = 1.45$ immersed in a water solution, with a refractive index of $n_m = 1.33$. Since $n_p > n_m$, the optical forces are attractive – i.e. the particles are attracted by the field intensity maxima. The light scattered by the trapped particle is collected by a second objective lens (OBJ2, Olympus PlanN 10x, NA = 0.25) and sent to a quadrant photodetector (QPD, New Focus 2931). This QPD generates signals proportional to the particle's radial and axial displacements [51]. Images of the particles are produced by focusing light from an LED into the sample, collecting it with OBJ1 and focusing onto a CCD (Image) with a doublet lens L3 of focal distance $f_3 = 15$ cm. We also added a filter (SPF) to avoid unwanted $780\,\mathrm{nm}$ back reflected light in the Image CCD.
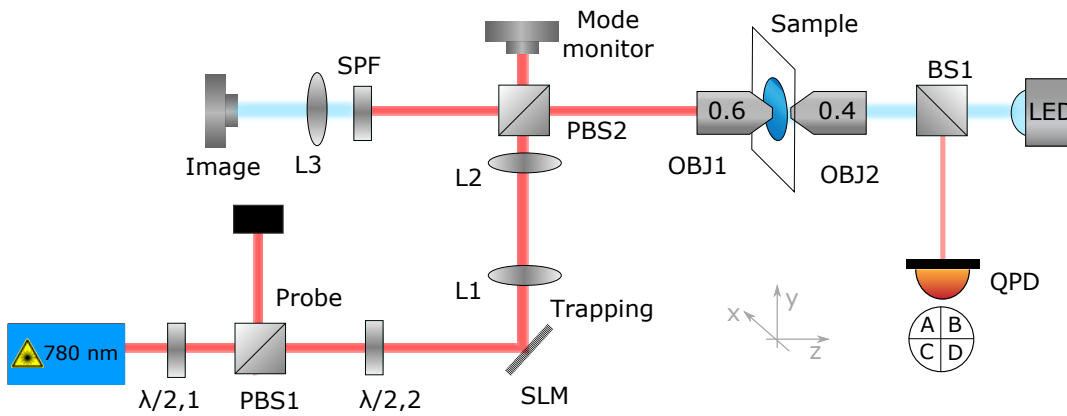
Figure 3.1: Schematic drawing of the setup for optical trapping with structured light beams. A 780 nm CW laser is split into orthogonal polarizations by a $\lambda/2$ and a PBS. The vertically polarized component of the beam is modulated by a spatial light modulator (SLM), sent through a pair of lenses $L_1$ and $L_2$ for magnification and directed to a microscope objective (NA = 0.6), to generate the optical trap. For bright tweezer experiments, the horizontally polarized component is blocked by a laser dump. The trapping beam passes through the sample and is collected by a second microscope objective (NA = 0.4) and used to detect the motion of a trapped microparticle with a quadrant photodiode (QPD). Image of the trapped particle is obtained by focusing light from an LED onto the particle, subsequently collected by the trapping objective, filtered by a short pass filter (SPF) and focused onto a CCD (Image) using lens $L_3$.

### 3.1.1
### Aligning the optical tweezer

To maximize the optical force, it is essential to perfectly align the beam at perpendicular incidence with respect to the objective. A first rough alignment method consists in making the beam pass through two closed pin-holes (closed apertures). As shown in Fig. 3.2, our setup is mounted in a vertical cage where it is possible to fix these adjustable apertures in the place of the objectives OBJ1 and OBJ2.

With a pair of two manually steerable mirrors, M1 and M2 in the Fig. 3.2, it is possible to align the beam following a simple 'beam walk' procedure. First, adjust the position of both mirrors in order to have the laser beam hitting the center of the mirror (optical elements are usually optimised for a beam impinging at their centers). Next, fix the mirrors when the reflected beam is passing through the center of both pin holes. Then, by using the screws of M1, center the beam on closed PH1. Open PH1 and center PH2 using mirror M2. Repeat the previous two steps iteratively. In a final step, shut both pin holes and maximize the transmitted power using a power meter placed above PH2.
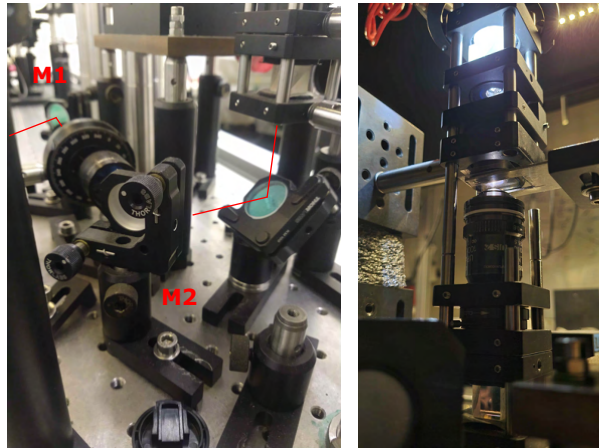
Figure 3.2: Alignment procedure of the experimental setup.

Then we remove the pin holes and place both objectives again.

After the above rough alignment procedure, fine adjustments are made by visualizing a reflected interference pattern between the incident laser beam and its reflection from a glass-air interface, produced in a CCD camera [46, 52]. Once a symmetric pattern is obtained, such as the one presented in Fig. 3.3, the optical tweezer is properly aligned.
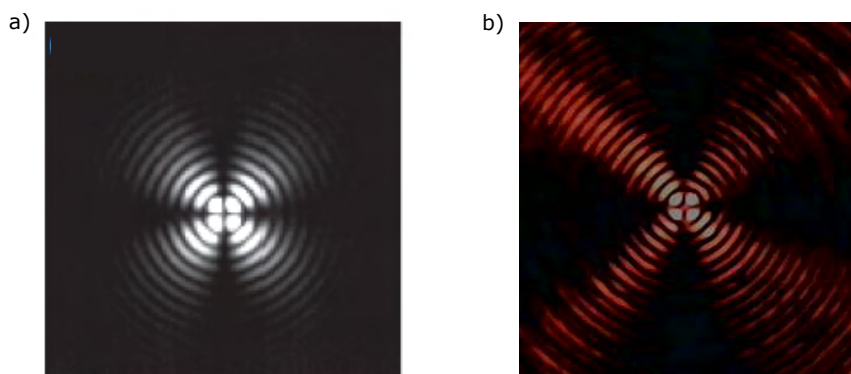


Figure 3.3: Reflected image of the interference pattern generated from a beam strongly focused on a glass slide. a) Image from Ref. [46] comapred to b) the pattern seen in our laboratory.

### 3.1.2
### Position tracking

The particle's position can be measured by a digital camera – as the one we previously calibrated in Section 2.5 – see Fig. 2.10b). Our digital cameras use a charge-coupled device (CCD) sensor to capture images. These detectors are

made with silicon chips that create arrays of photosensitive sites. The incident light generates charge packets at these sites that are then moved around the chip before being converted to a voltage output [46]. This method limits the readout speed and leads to unwanted effects such as saturation in which a relatively high amount of charges spread into neighboring pixels, creating large areas with bright spots. While taking images of the trapping beam, it is crucial to certify that the CCD is not saturated.

The imaging system is created according to Fig. 3.1. An LED is used to focalize light inside the sample and is then collected by a pair of lenses OBJ1 and L3, with focal lenghs $f_{OBJ1} = 1.8\,\text{mm}$ and $f_{L3} = 150\,\text{mm}$, respectively. We can use the geometric optics formalism discussed in Section 2.5 to calculate the magnification of the image measured by CCD 01. As the trapped particle is typically near the focal point of the objective, we have a scenario similar to Fig. 2.6, where the image has a magnification $M = 83.33$. Figure 3.4a) shows a typical frame recorded with our imaging system. We applied a colormap scale for contrast enhancement. The positions of the particle can be calculated by fitting the centroid of the intensity distribution in each frame. Assuming the particle intensity profiles on the CCD are Gaussian, we can find the mean values of $x$ and $y$ directions with sub-pixel resolution, in the nanometer scale. Following the Gaussian distribution as written in Eq. (2-11) we can also define $\omega_0 = 2\sigma$ where $\sigma$ is the standard deviation and $\omega_0$ is the radius $R$ of the magnified particle. We find $\omega_0 = (16.98 \pm 0.4)\,\text{px}$ for the $x$-direction and $\omega_0 = (15.43 \pm 0.3)\,\text{px}$ for the $y$-direction, in agreement with a mean radius of $R = (16.2 \pm 0.3)\,\text{px}$. By applying the conversion factor $a_{CCD01} = 2.82\,\mu\text{m/px}$, this implies a magnified diameter of $2R = (91.2 \pm 2.0)\mu m$. The particle diameter can then be determined by dividing the diameter of the particle in the image by the magnification factor $M$, yielding the value $2R = (1.09 \pm 0.02)\mu m$. This is in excellent agreement with the nominal value for our spheres, confirming our calibration methods are good.

In some cases it may be challenging to obtain a good-quality image. Misalignment of the LED the transmission coefficient for white light in certain fluids can be a major source of problems. Moreover, external perturbations or effects of optical force may shift the equilibrium position of a trapped particle, slightly moving it away from the objective focal plane, causing image distortions (see Chapter 4 for an example of such problem). To mitigate these limitation we can apply image processing techniques [53]. Figure 3.5a) shows a bad quality image. To improve signal-to-noise ratio, we apply a histogram equalization transformation that adjusts the global contrast of the original image [53], as shown in Fig. 3.5b). In the following we apply two filters iteratively: a median
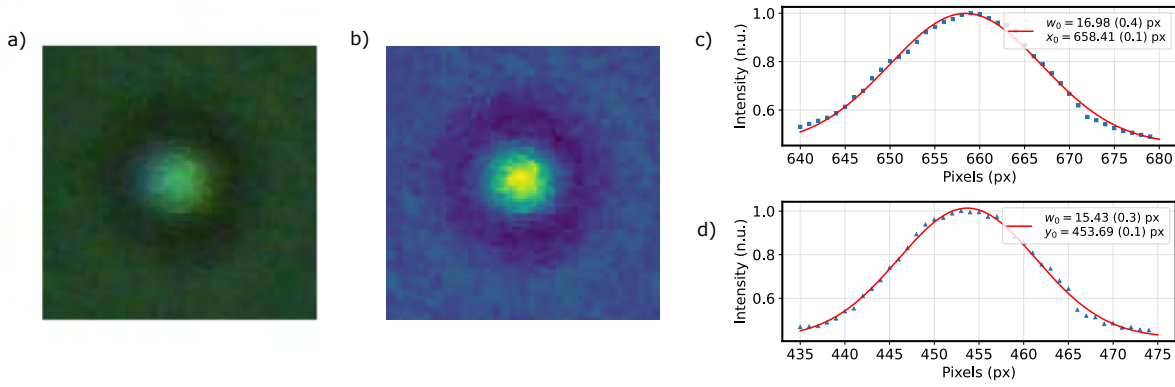
Figure 3.4: Detecting centroid of a CCD image. a) Original image. b) Colorized image, for better visualization. c-d) Gaussian fits to the intensity levels in c) $x$ and d) $y$ directions.

blurring filter calculates the mean value of all pixels in the neighborhood of a central one and replaces it with this mean value. This filter is widely used to remove the so-called salt-and-pepper noise - randomly occurring white and black pixels that are generally caused by sharp and sudden disturbances in the image signal [54] - present in Fig. 3.5b). A second filter, the Gaussian blurring, is applied; this is very similar to the first filter, but instead of using a simple mean it calculates a weighted mean based on a Gaussian distribution. The final result is shown in Fig. 3.5c). Note that the salt-and-pepper noise was removed as well as the two black dots in the right center of the images that we later discovered to be an imperfection in the camera.

Next we apply a color mask to select the desired circle and execute a Canny edges algorithm to detect the contours considering only circles with realistic values of radius, as shown in Fig. 3.5d-e). Fig. 3.5f) shows the final result. This process returns the centroid and radius of the particle agreeing with the first model.

Once the tweezer is aligned and we are capable of measuring the position of a trapped particle, we need to calibrate the optical forces exerted by the beam on the trapped particle. This calibration then allows us to use the tweezer as a force sensor. When a particle is optically trapped in a Gaussian beam, it is subjected to an approximately harmonic potential and hence, to a restoring force proportional to its displacements. The calibration of an optical trap consists of the determination of the stiffness constant $k_i$ ($i = x, y, z$) of the various directions defining the three-dimensional harmonic potential. In general, these spring constants depend both on the properties of the light beam and the particle. In the next two sections, we discuss the procedure to calibrate such force based on two different methods: one employing a slow data acquisition detector (sampling rates on the order of Hz) based on a CCD and the second using a quadrant QPD, with a fast acquisition rate (sampling rates on the

order of dozens of kHz).
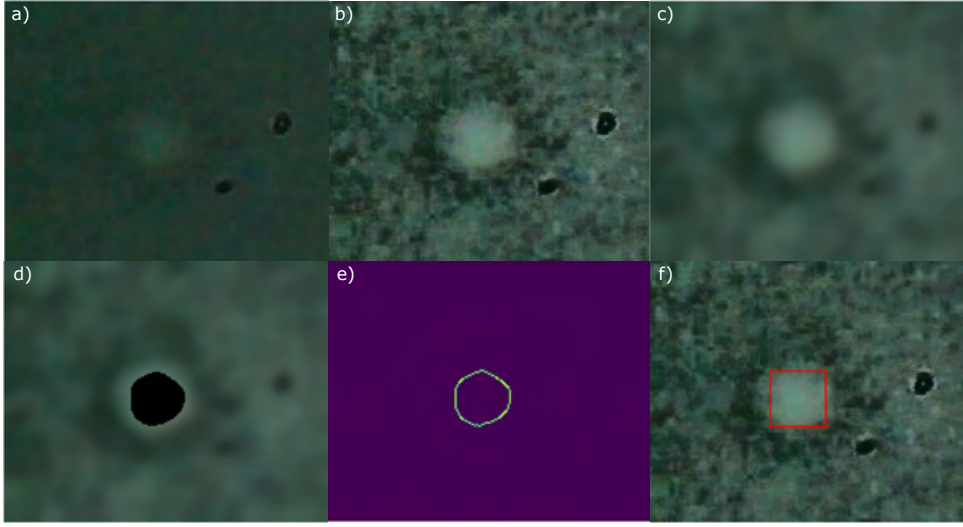


Figure 3.5: Image processing techniques applied to particle detection. a) Original image. b) Increasing the contrast. c) Applying a median filter and a Gaussian filter. d) Application of a color mask to select the desired circle. e) Applying a Canny edges transformation in the image to extract the contours that exists in the modified image. f) Final result.

## 3.2
## Potential analysis

In thermal equilibrium and in the limit that conservative forces dominates over dissipative forces, we can implement the potential analysis method. This method works for generic confining potentials $U(r)$ and is based on the probability density $\rho(r)$ of finding the particle at a given position $r$. According to the Maxwell-Boltzmann distribution,

$$\rho(r) = \rho_0 \exp\left(-\frac{U(r)}{k_b T}\right),\tag{3-1}$$

where $\rho_0$ is a normalization factor ensuring $\int_0^\infty \rho(r)dr = 1$, $T$ is the temperature of the medium in which the particle is immersed and $k_b$ is Boltzmann's constant. The potential can be reconstructed by taking the natural logarithmic of the above equation,

$$U(r) = -k_B T \ln\left(\frac{\rho(x)}{\rho_0}\right).\tag{3-2}$$

The probability distribution $\rho(r)$ can be obtained by acquiring large data-sets of the particle's position; note the coordinates of the particle need not be uncorrelated [55], meaning this method works independently of the detector's acquisition time $\Delta t = t - t_0$ and the characteristic relaxation time

for a particle in a harmonic potential in the overdamped regime, $\tau = \gamma/k$. So long as the system is in equilibrium, the potential analysis can be employed as a characterization method, regardless of the harmonic approximation. As a final remark, this method does not rely on any knowledge of the particle or medium properties, in contrast to other methods such as the power spectrum density analysis.

## 3.3
## Power spectrum density

Among the most employed techniques to calibrate optical tweezers is the power spectrum density [55, 56]. In contrast to the potential analysis method, it has the advantage of working in the frequency domain, which enables one to filter sources of noise such as mechanical perturbations and electronic noise. As a first example, consider Fig. 3.6, where an unwanted modulation introduced by the SLM can be singled out and filtered.
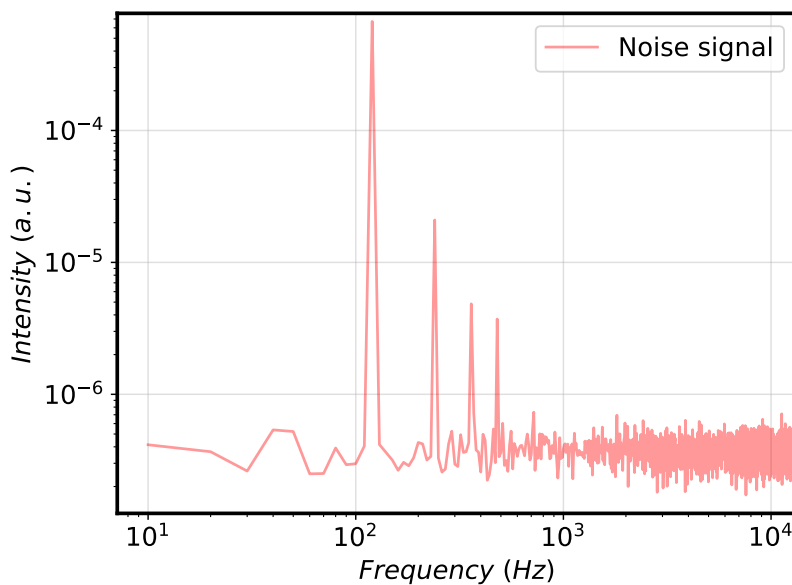
Figure 3.6: Raw PSD of a beam modulated by the SLM displaying unwanted time-dependent modulations between 100 Hz and 1 kHz. The PSD is obtained by averaging 10 traces of the QPD SUM signal in the time-domain, at a sampling frequency of $25kHz$. We can see well-defined peaks corresponding to 120 Hz, 240 Hz, 360 Hz and 600 Hz frequencies. We systematically eliminate these peaks for all measurements from now on. Note the highest oscillation peak occurs at 120 Hz, and originates from the intensity of ambient light modulated by the 60 AC electricity grid.

Beyond characterizing the noise in the setup, the PSD method can be used

to calibrate a harmonic oscillator subject to Brownian motion. The motion of a sphere of radius $R$ and mass $m$ confined in a harmonic potential is described by the Langevin equation,

$$m\ddot{x}(t) + \gamma_0 \dot{x}(t) + kx(t) = (2k_B T \gamma_0)^{1/2} \eta(t), \qquad (3\text{-}3)$$

where $x(t)$ is the trapped particle's stochastic trajectory, $\gamma_0$ the friction coefficient, $k$ the spring constant and $T$ the temperature of the medium in which the particle is immersed. The term $(2k_B T \gamma_0)^{1/2} \eta(t)$ represents a Brownian force modeled as a random Gaussian process at temperature $T$. The $\eta(t)$ factor is defined such that for all $t$ and $t'$,

$$\langle \eta(t) \rangle = 0 \; ; \; \langle \eta(t), \eta(t') \rangle = \delta_{t,t'}. \qquad (3\text{-}4)$$

We can calculate $\gamma_0$ using Stokes's law,

$$\gamma_0 = 6\pi \rho \nu R, \qquad (3\text{-}5)$$

where $\rho$ is the fluid's density and $\nu$ the kinematic viscosity. Eq. (3-3) can be simplified by considering the trapped microsphere is immersed in water. In this case, inertia plays no role in the dynamics of the microparticle, and the damping forces are much more pronounced than inertial ones. We can introduce the Reynolds number, which quantifies the ratio of typical inertial forces to viscous force [57],

$$\frac{\text{inertial forces}}{\text{viscous forces}} \approx \mathcal{R} = \frac{Rv}{\nu}. \qquad (3\text{-}6)$$

For water, $\nu \approx 10^{-2}\,\text{cm}^2/\text{s}$, while $v \approx 30\,\mu\text{m/s}$, which implies $\mathcal{R} \approx 10^{-4}$. Hence we simplify Langevin's equation to:

$$\dot{x}(t) + 2\pi f_c x(t) = (2D)^{1/2} \eta(t), \qquad (3\text{-}7)$$

where we introduced the corner frequency $f_c = k/(2\pi\gamma)$ and diffusion constant $D = k_B T/\gamma_0$. Note that Eq. (3-7) refers to overdamped systems, typically of wet tweezers, while Eq. (3-3) refers to more general cases as levitated nanospheres in vacuum where the drag coefficient is much smaller [58, 59].

In the following we repeat the procedure detailed in Ref. [56]. We calculate the Fourier transform of $x(t)$, $\tilde{x}_k$,

$$
\begin{aligned}
\tilde{x}_k(f_k) &= \int_{-T_{msr}/2}^{T_{msr}/2} dt\, x(t) e^{i2\pi f_k t} \\
&= \frac{(2D)^{1/2} \tilde{\eta}_k}{2\pi(f_c - if_k)},
\end{aligned}
\qquad (3\text{-}8)
$$

where $T_{msr}$ is the recording time of $x(t)$. The PSD is then conveniently calculated through the square modulus of $\tilde{x}_k$ divided by $T_{msr}$. For a harmonic potential, the PSD assumes a Lorentzian form,

$$P_k(f) \equiv \frac{|\tilde{x}_k|^2}{T_{msr}} = \frac{D|\tilde{n}_k|^2 T_{msr}}{2\pi^2 T_{msr}(f_c^2 + f_k^2)}$$
$$= \frac{D/(2\pi^2)}{(f_c^2 + f_k^2)}, \tag{3-9}$$

where we have used $\langle \tilde{\eta}_k \rangle = 0$ and $\langle \tilde{\eta}_k * \tilde{\eta}_l \rangle = T_{msr}\delta_{k,l}$ since $\eta(t)$ is an uncorrelated random variable.

In fact, the experimental data is sampled at frequency $f_{sampling} = 1/\Delta t$ and hence the measured trajectory is a discrete time series. Although Eq. (3-9) fits experimental data for $0 < f_k \leq f_{Nyq}$, where $f_{Nyq} \equiv f_{sampling}/2$, it should only be considered in the case of $f_c \ll f_{Nyq}$. Out of this interval, aliasing effects becomes more expressive and one should implement the aliased Lorentzian curve [56], calculated through a discrete Fourier transform of $x(t)$,

$$P_{k,aliased}(f) = \frac{(\Delta x^2 \Delta t)}{1 + c^2 - 2c \, \cos(2\pi k/N)}, \tag{3-10}$$

where we have defined the constants:

$$c \equiv \exp(-\pi f_c/f_{Nyq}), \tag{3-11a}$$

$$\Delta x \equiv \left( \frac{(1 - c^2)D}{2\pi f_c} \right)^{1/2}. \tag{3-11b}$$

Note that Eq.3-10 becomes the Lorentzian curve in the limit that $f_c \ll f_{Nyq}$ and $|f_k| \ll f_{Nyq}$.

Although some groups measure the PSD with cameras, typically with high sampling rate CMOS sensors [60], the usual procedure is to use photodetectors or QPDs although the latter is characterized for having a typical low frequency response above $100\,\mathrm{kHz}$. In the next subsections we introduce the working principle of a position-sensitive detector and a knife-edge detector based on two photodetectors as an alternative to a QPD sensor.

### 3.3.1
### Position sensitive detectors

A QPD has a linear relation between position and current across its active area. When seed by an input optical mode, internal electrodes provide independent current signals named $I_A$, $I_B$, $I_C$ and $I_D$ providing three outputs $X(t)$, $Y(t)$ and $SUM(t)$ related as,

$$X(t) = \frac{I_A + I_D - (I_B + I_C)}{I_A + I_B + I_C + I_D}, \tag{3-12a}$$

$$Y(t) = \frac{I_A + I_B - (I_C + I_D)}{I_A + I_B + I_C + I_D}, \tag{3-12b}$$

$$SUM(t) = I_A + I_B + I_C + I_D. \tag{3-12c}$$

Particle displacements inside the optical trap induce small deviations in the scattered beam, which can be read in the QPD. This information is obtained by dividing $X(t)$ by $S(t)$ and $Y(t)$ by $S(t)$ for each time $t$ to get $\alpha_x x(t)$ and $\alpha_y y(t)$, respectively. The constants $\alpha_x$ and $\alpha_y$ are conversion factors from units of voltage to a physical unit of lenght, and $x(t)$, $y(t)$ are the particle's coordinates at each time $t$. To characterize these constants we need to replace $x(t)$ for $\alpha_x x(t)$ in Eq. (3-7) giving rise to the same Lorentzian curve with a new factor,

$$P_k(f) = \alpha_x^2 \frac{D/(2\pi^2)}{(f_c^2 + f_k^2)}. \tag{3-13}$$

Hence, by assuming the medium's temperature is known and calculating the drag coefficient using Eq.(3-5), we fit our experimental data with Eq. (3-9) to find the empirical value $D_{exp}$ and divide it by the theoretical diffusion coefficient $D$ to obtain,

$$\alpha_x = \sqrt{\frac{D_{exp,x}}{D}}, \tag{3-14a}$$

$$\alpha_y = \sqrt{\frac{D_{exp,y}}{D}}. \tag{3-14b}$$

When the distance $h$ between the trapped particle and the surface is well known, one can also calculate the drag coefficient using [41]

$$\gamma_s(T) = \frac{\gamma(T)}{1 - \frac{9}{16}\left(\frac{R}{h}\right) + \frac{1}{8}\left(\frac{R}{h}\right)^3 - \frac{45}{256}\left(\frac{R}{h}\right)^4 - \frac{1}{16}\left(\frac{R}{h}\right)^5}. \tag{3-15}$$

In our experiment, although we cannot determine exactly the value of $h$, it is surely much bigger than particle radius $R$. Assuming then $R/h \longrightarrow 0$ we can safely use Eq. (3-5) to calculate $\gamma_0$.

Fig 3.7 shows the PSD of bright Gaussian tweezer presenting corner frequencies $f_{c_x} = (942.4 \pm 23.8)\,$Hz and $f_{c,y} = (931.8 \pm 22.3)\,$Hz, which agree to each other within the uncertainty. The PSD was numerically calculated from time series of the particle motion using the Welch method, and fitted by an Aliased Lorentzian (Eq.(3-10)). Each point (error bar) in the figure is the mean value (standard deviation) obtained from 10 PSD's. Each of these PSD's is calculated by averaging 10 measured traces with a sampling frequency of

25 kHz.
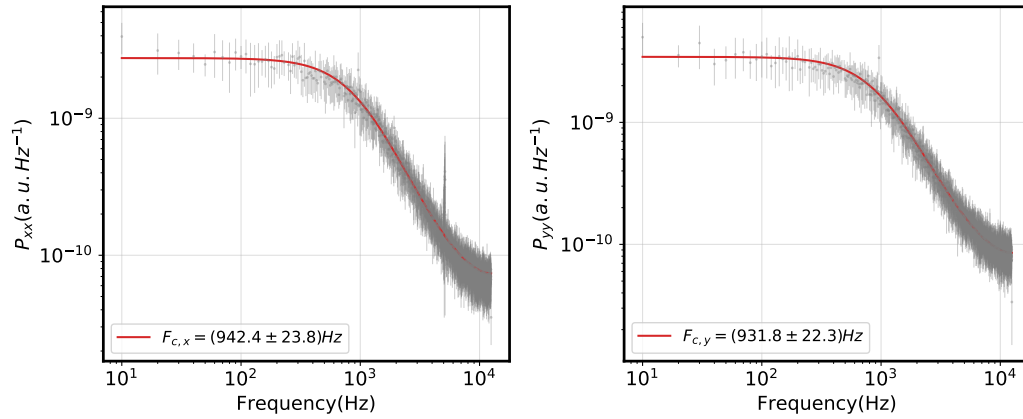


Figure 3.7: Measured PSDs and the resulting fits for a Gaussian tweezer experiment.

We fit a Lorentzian curve with a constant noise term; we find $\alpha_x = (3.56 \pm 0.08) \times 10^5$ m/V and $\alpha_y = (3.94 \pm 0.08) \times 10^5$ m/V. The error bars are calculated based on the estimated standard deviation of the fitted parameters. For completeness, we show examples of the particle's trajectories from which we obtained these measurements in Fig. 3.8.
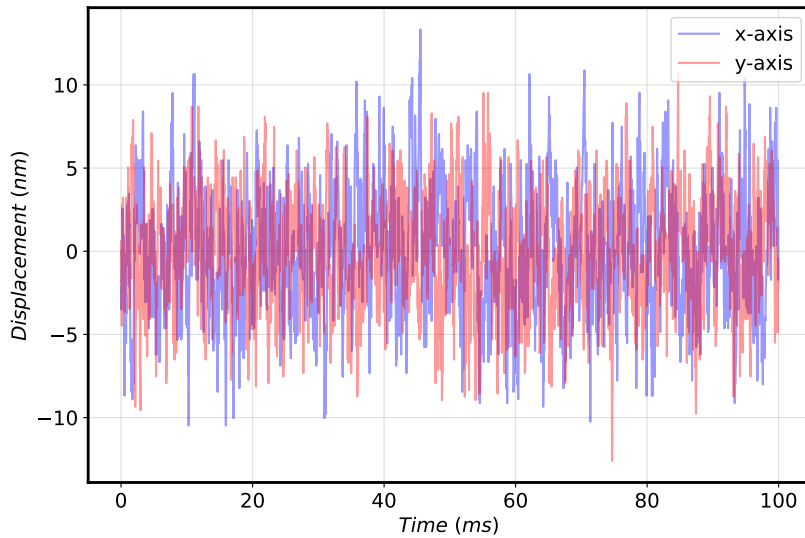


Figure 3.8: Example traces of the particle stochastic trajectory.

### 3.3.2
### Knife-Edge detector

An interesting alternative to a QPD sensor is the knife-edge detector [61]. In this detection setup, the collected beam is divided into two paths with an additional beam splitter. One of the beams is focused on a photodetector

yielding a signal $S(t)$, proportional to the beam's total power $P(t)$. The other beam is partially blocked by a thin plate, denoted as a knife, such that half of the beam power in that path is blocked when the particle is at the center of the trap. The other half that passes through the knife is focused on a second regular photodetector.

Once again we explore the fact that deviation angles from the scattered light are proportional to the particle's position. As the first detector is insensitive to these variations, the second detector gives us a signal $X_k(t)$ containing a term proportional to both $P(t)$ and $x(t)$ and an offset term relative to the detected power $P(t)$ when the particle is not radially displaced. Due to possible electronic noise sources, we add two variables $\eta_X(t)$ and $\eta_S(t)$ for $X$ and $S$ channels,

$$\frac{X_k(t)}{S(t)} = \frac{(\beta_0 + \beta_x x(t))\, P(t) + \eta_x(t)}{\beta_S P(t) + \eta_S(t)}, \tag{3-16}$$

where we have defined $\beta_0$, $\beta_x$ and $\beta_S$ proportionality constants. In the following we assume the amplitude of the electronic noise in the $S$ Channel is much smaller than the total power, $|\eta_S(t)| \ll S(t)$. We then Taylor expand,

$$\begin{aligned}\frac{X_k(t)}{S(t)} &\approx ((\beta_0 + \beta_x x(t))\, P(t) + \eta_x(t))\left(1 - \frac{\eta_S(t)}{\beta_S P(t)}\right)\\ &\approx \frac{\beta_0}{\beta_S} + \frac{\beta_X}{\beta_S}x(t) + \frac{1}{\beta_S\langle P(t)\rangle}\eta_X(t) - \frac{\beta_0}{\beta_S^2\langle P(t)\rangle}\eta_S(t),\end{aligned} \tag{3-17}$$

where we have considered the variations in $X_k(t)$ due to radial displacement is much smaller than the half beam's signal, $|\beta_x x(t) P(t)| \ll \beta_0 P(t)$ which means $\beta_x x(t)\eta_S(t)/\alpha_s$ term can be neglected. Terms with multiplicative noise factors are also neglected. Finally, we also considered the variations in $P(t)$ due to axial displacements are much smaller than $P(t)$ and hence we neglect it by just adopting $\langle P(t)\rangle$ instead.

Since $x(t)$, $\eta_X(t)$ and $\eta_S(t)$ are all independent of each other, the power spectrum of the above equation is the sum of the power spectrum of each one of the components. Considering $\eta_X(t)$ and $\eta_S(t)$ as independent white noise, the PSD of the third and fourth term in Eq. (3-17) are constant terms in the overall power spectrum. Hence, the resulting PSD should be fitted to an aliased Lorentzian added to a constant term [61].

The knife-edge detector allows one to measure the position of a trapped particle using regular photodetectors with higher bandwidth than QPDs and other similar position-sensitive devices [61]. The derivation was done for the $x(t)$ direction but it can be extended for the $y(t)$ just by rotating the knife in an orthogonal orientation and repeating the procedure. Actually, it is possible

to instantaneously fully calibrate the optical trap with three independent silicon detectors. Combining these setups with low-noise electronics opens the possibility of calibrating even levitated nanoparticles when higher oscillation frequencies are accessed. This technique is an extension of the use of knife-edge detection proposed in the field of high-speed atomic force microscopy [62].
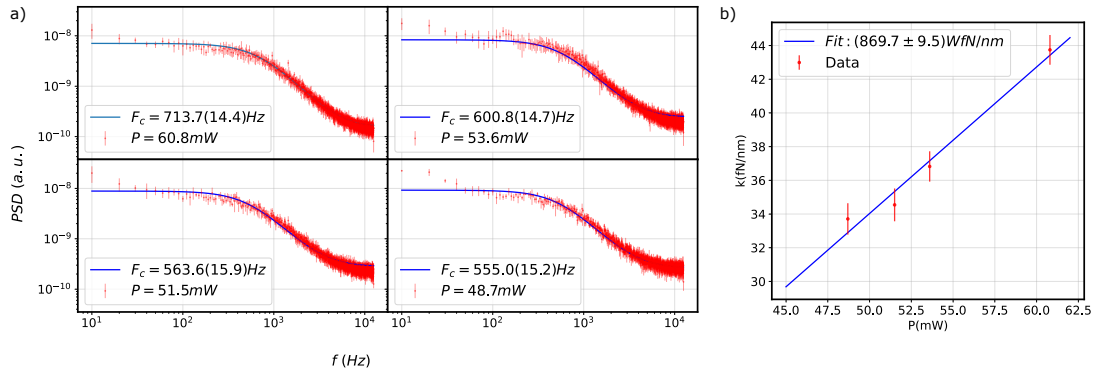


Figure 3.9: Gaussian tweezer for different trapping powers a) Measured PSD and the resultant fit. b) Spring constant as a function of trapping power.

## 3.4
## Structured light tweezer

Beyond the Gaussian beam, the ability to customize the phase and amplitude of an electric field has been widely used in optical tweezers in the last few years [29]. Structured light beams present numerous possibilities to study the interaction between light and matter due to transfer of OAM, induced motion via time-dependent optical potentials and even manipulation of nanometer-sized targets.

In this section, we discuss two ideas for optical trapping with structured light in bright tweezers. We first analyze a nonlinear tweezer, that is, an optical beam exerting a harmonic potential plus a quartic perturbation, as in a Duffing oscillator. Next, we present the Bean Beam experiment: a superposition of a Laguerre-Gauss and a Gaussian mode that, upon variation of relative phase, produces rotating pattern capable of inducing circular motions of a trapped particle. This has been previously demonstrated using silica microspheres and Chinese hamster chromosomes in an interferometer-based setup [63]. We present our experimental results for the bean-beam experiment as well as an idea to calibrate the mode's NA based on measurements of the particle's trajectory.

### 3.4.1
### Non-linear tweezer

We have so far treated the Gaussian tweezer as a harmonic potential, but in fact there are higher order corrctions to the harmonic potential which can become important for large particle displacements. In this scenario, a Rayleigh particle $R < \lambda/10$ may be subject to nonlinear forces that to a first approximation induce a shift in the particle's corner frequency in both the overdamped and underdamped regimes [64]. Similar behaviors have been observed by previous works using different approaches: by measuring the expected shift in the PSD [65] and the particle's trajectory out-of-equilibrium, in the transient time in which the variance of the particle's position increases depending on the oscillator's parameters [66].

In Gaussian tweezers, these nonlinear effects are small, however, it is possible to enhance nonlinearities using external electric feedback [67] or structured light beams. Consider for instance a superposition between $LG_{0,0}$, $LG_{1,0}$ and $LG_{2,0}$ [64],

$$\boldsymbol{E}_{nl} = \boldsymbol{E}_{Gauss} + A_1 \boldsymbol{E}_{1,0}^{LG} + A_2 \boldsymbol{E}_{2,0}^{LG}, \tag{3-18}$$

where amplitudes $A_1, A_2$ are real coefficients. To eliminate coupling between axial and radial directions we may have [64],

$$A_2 = \frac{-15 - 8A_1 + \sqrt{220 + 220A_1 + 49A_1^2}}{5}. \tag{3-19}$$

Taylor expanding the intensity of this beam to the fourth order around the origin leads us to a three-dimensional extension of a Duffing oscillator,

$$\frac{I(\rho, z)}{I_0} = k + k_{\rho^2}\frac{\rho^2}{\omega_0^2} + k_{\rho^4}\frac{\rho^4}{\omega_0^4} + k_{z^2}\frac{z^2}{z_R} + k_{z^4}\frac{z^4}{z_R^4}, \tag{3-20}$$

where $k_{\rho^2}, k_{\rho^4}, k_{z^2}$ and $k_{z^4}$ are functions of $A_1$ which can be tuned over a wide range of values [64]. Figure 3.10 shows the intensity pattern of this structured mode in the axial direction and Fig. 3.11 shows its intensity distribution in $x$ and $z$ directions along with the optical force applied to a $R = 70\,\text{nm}$ $SiO_2$ sphere immersed in water. Note that the blue and red curves scale with $\omega_0$ and $z_R$, respectively.

The non-linear nature of the optical force generated by the proposed superposition can be seen when compared with a Gaussian beam, as in Fig.3.12. The normalized red (Gaussian) and blue (non-linear beam) curves have a similar behavior near the origin where the cubic term is negligible when compared with the first-order term. As the particle moves away from the equilibrium point, it experiences a stronger force against its displacement.
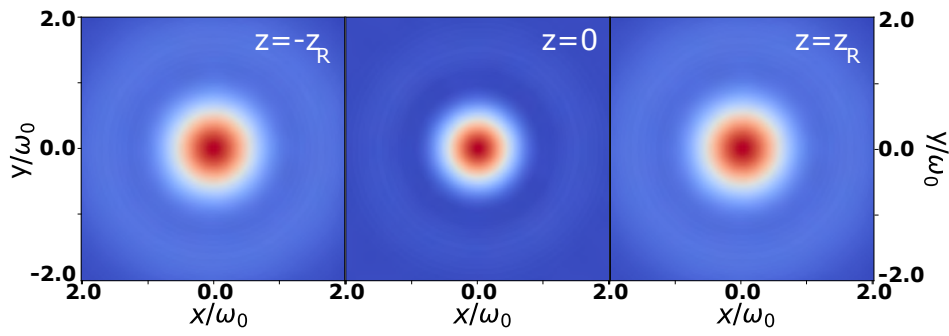
Figure 3.10: Intensity pattern of the non-linear structured light beam in the axial direction.
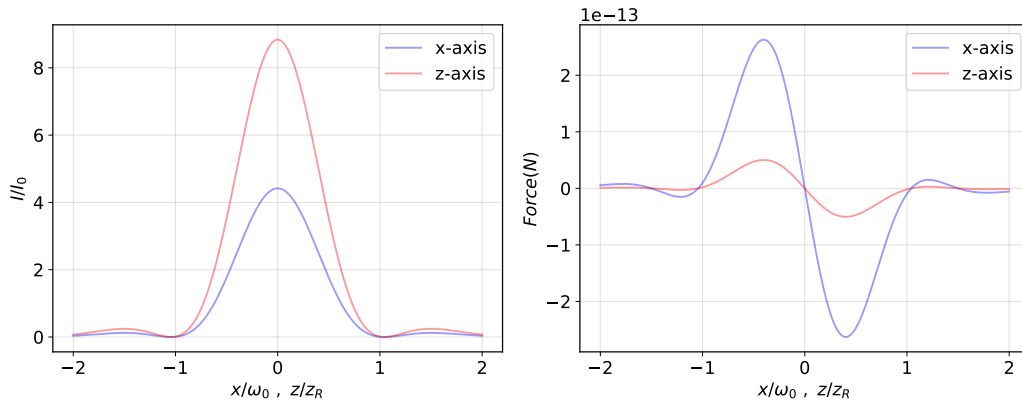


Figure 3.11: Intensity distribution and optical forces generated by the non-linear structured light beam
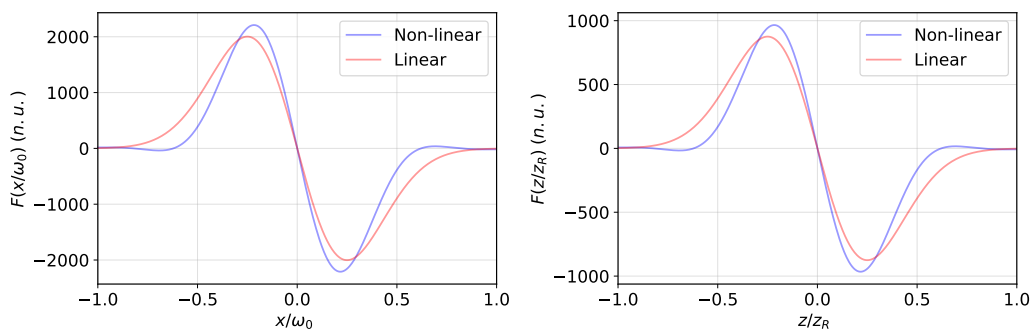


Figure 3.12: Optical forces generated by the Gaussian and the non-linear structured beam

### 3.4.2
### The Bean Beam experiment

An interesting phenomenon occurs for a superposition between a Gaussian and a $LG_{1,0}$ mode. Interfering both electric fields, Eq. (2-8) and Eq.(2-12), with a relative phase of $\theta$ leads us to

$$
\begin{aligned}
\boldsymbol{E}_{Bean} &= \boldsymbol{E}_{Gauss} + e^{i\theta}\boldsymbol{E}_{1,0}^{LG} \\
&= \boldsymbol{E}_{Gauss}\left[1 + \frac{\sqrt{2}\rho}{\omega(z)}e^{i(\theta+\phi-\zeta(z))}\right].
\end{aligned}
\tag{3-21}
$$

The corresponding intensity is,

$$
\begin{aligned}
I_{Bean}(\rho,\phi,z) &= I_{Gauss}\left[1 + \frac{2\sqrt{2}\rho}{\omega(z)}\cos(\theta+\phi-\zeta(z)) + \left(\frac{\sqrt{2}\rho}{\omega(z)}\right)^2\right] \\
&= I_0\frac{\omega_0^2}{\omega(z)^2}\exp\left[-\frac{2\rho^2}{\omega(z)^2}\right]\left[1 + \frac{2\sqrt{2}\rho}{\omega(z)}\cos(\theta+\phi-\zeta(z)) + \left(\frac{\sqrt{2}\rho}{\omega(z)}\right)^2\right].
\end{aligned}
\tag{3-22}
$$

As discussed in Section 2.6, for $m > 1$, particles find equilibrium in the most intense point of a laser beam, which occurs close to the focal plane, allowing us to assume $z = 0$ in the above equation. The resulting intensity at $z = 0$ is then,

$$
I_{Bean}(\rho,\phi,0) = I_0\exp\left[-\frac{2\rho^2}{\omega_0^2}\right]\left[1 + \frac{2\sqrt{2}\rho}{\omega_0}\cos(\theta+\phi) + \left(\frac{\sqrt{2}\rho}{\omega_0}\right)^2\right].
\tag{3-23}
$$

The theoretical patterns are compared to experimental frames in Fig. 3.13 for different values of the phase $\theta$. Note that the pattern has an intensity maxima displaced from the origin, and by adjusting $\theta$ we can rotate the intensity maximum around the $z$-axis. A trapped particle would follow this rotation.
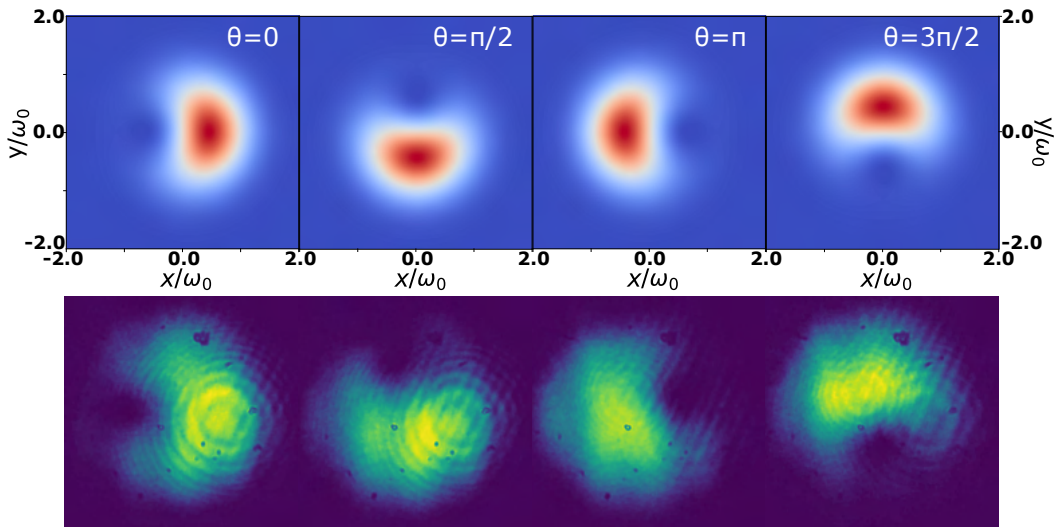


Figure 3.13: Bean Beam pattern. Calculated (top) and experimental (bottom) frames for a varying relative phase $\theta$.

Taking $y = 0$, we can calculate the coordinate of maximum intensity along the $x$ direction, $x_{max}/\omega_0 = \frac{\sqrt{5}-1}{2\sqrt{2}}$. This is approximately the $x$ coordinate of the particle's equilibrium position. When we rotate the bean pattern by changing $\theta$, we expect to observe a circular particle trajectory with diameter given by $2R = 2\frac{\sqrt{5}-1}{2\sqrt{2}}\omega_0$. Given $R$ we then can calculate the NA of the beam,

$$\text{NA} = \frac{\lambda}{\pi n_m}\left(\frac{\sqrt{5}-1}{2\sqrt{2}R}\right). \tag{3-24}$$

This expression provides a mean of measuring the NA from a property of the particle's trajectory, namely its radius $R$.

Estimating the NA of a beam is very important for characterizing optical forces, in particular in our case where the most of the intensity is not concentrated in the central point. In this situation, overfilling the objective lens aperture may introduce border effects that deteriorate the intensity distribution of the incident beam in the focal plane, causing imperfections in the optical trap. To avoid unwanted border and diffraction effects, we need to guarantee the beam NA is smaller than the NA of the objective. Moreover, measuring the NA of a highly focused beam is challenging, due to the fast divergence of the intensity after the focal plane. The Bean Beam presents a solution to this problem, enabling calibration of the beam parameters through measurements of the trapped particle motion. We now describe this calibration technique in detail.

Figure 3.14 shows the result of a rotation experiment using the Bean Beam on a microparticle. Each frame in the image corresponds to a discrete rotation of $\pi/4$. We would like to use this data to measure the beam's NA but to do so, some modelling is required first.

The particle executes a circular motion in a given coordinate system $(x, y, z)$, parameterized by $x = R\cos\phi$, $y = R\sin\phi$ and $z = 0$. What we measure, instead, are the coordinates of the particle in a different reference frame $(x', y', z')$, rotated with respect to $(x, y, z)$. Assuming a generic rotation from the unprimed to primed coordinate systems, the measured trajectory deviates from the perfect circular trajectory by mixing the $\sin\phi$ and $\cos\phi$ quadratures. Define the mixing parameters $\alpha_{ij}$, $A_i$ and $B_i$ as the linear coefficients appearing in,

$$x' = \alpha_{11}R\cos\phi + \alpha_{12}R\sin\phi = A_x\cos\phi + B_x\sin\phi,$$
$$y' = \alpha_{21}R\cos\phi + \alpha_{22}R\sin\phi = A_y\cos\phi + B_y\sin\phi. \tag{3-25}$$

We can measure the $A_i$ and $B_i$ parameters by fitting the observed trajectory with Eq. (3-25).

To figure out the relation between $A_{ij}$ and the rotation angles, consider

Figure 3.14: Microparticle rotation under the Bean Beam.

$M$ as the Euler rotation matrix with $M = M_z(\delta)M_y(\theta)M_x(\psi)$, where $\delta$, $\theta$[1] and $\psi$ are the rotation angles about the $z$, $y$ and $x$ directions. By symmetry, we can assume rotations around the axial direction are irrelevant, thus $\psi = 0$. The matrix $M$ is then

$$
M = \begin{pmatrix} \cos\theta\cos\delta & \sin\psi\sin\theta\cos\delta - \cos\psi\sin\delta & \cos\psi\sin\theta\cos\delta + \sin\psi\sin\delta \\ \cos\theta\sin\delta & \sin\psi\sin\theta\sin\delta + \cos\psi\cos\delta & \cos\psi\sin\theta\sin\delta - \sin\psi\cos\delta \\ -\sin\theta & \sin\psi\cos\theta & \cos\psi\cos\theta \end{pmatrix}
$$

$$
= \begin{pmatrix} \cos\theta & \sin\psi\sin\theta & \cos\psi\sin\theta \\ 0 & \cos\psi & -\sin\psi \\ -\sin\theta & \sin\psi\cos\theta & \cos\psi\cos\theta \end{pmatrix}.
$$

$$(3\text{-}26)$$

By substituting these parameters in Eq. (3-25) we find the desired relations, and using trigonometric identities we arrive at:

$$
\begin{aligned}
A_x^2 &= R^2\cos^2\theta \;\Rightarrow\; R^2\sin^2\theta = R^2 - A_x^2, \\
A_y &= 0, \\
\left.\begin{aligned} B_x^2 &= R^2\sin^2\psi\sin^2\theta \\ B_y^2 &= R^2\cos^2\psi \end{aligned}\right\} & \quad B_x^2 + \sin^2\theta\, B_y^2 = R^2\sin^2\theta.
\end{aligned}
$$

$$(3\text{-}27)$$

After some algebra with the above equations, we find a quadratic function for $R^2$ whose solutions are described as a function of the fitted parameters above,

$$
R = \pm\sqrt{\frac{\alpha \pm \sqrt{\alpha^2 - 4\beta}}{2}}, \tag{3-28}
$$

where we have defined,

$$
\alpha = A_x^2 + B_x^2 + B_y^2, \tag{3-29a}
$$

$$
\beta = A_x^2 B_y^2, \tag{3-29b}
$$

and the physical radius is the positive real solution.

The resulting fit employing this analysis is shown in Fig. 3.15. We find a radius of $R = 0.18\,\mu\text{m}$ from which we calculate $\omega_0 = 0.41\,\mu\text{m}$. This value agrees

---

[1]Note this $\theta$ is **not** the same angle variable as the superposition relative phase in the Bean Beam.

with the expectation for a Bean Beam with estimated size $\omega_c = 1.125\,\text{mm}$ prior to OBJ1. If we assume the geometric optics approximation of Eq. (2-21) for $f = 1.8\,\text{mm}$ then $\omega_{0,g} = 0.40\,\mu\text{m}$. The similarities between both results indicate agreement between the theory and this calibration method. Finally, by using Eq. (3-24) with the refractive index of water $n_m = 1.33$, we find NA= 0.46. As we will see, this value is in agreement with other measurements performed during the dark focus tweezer experiment.
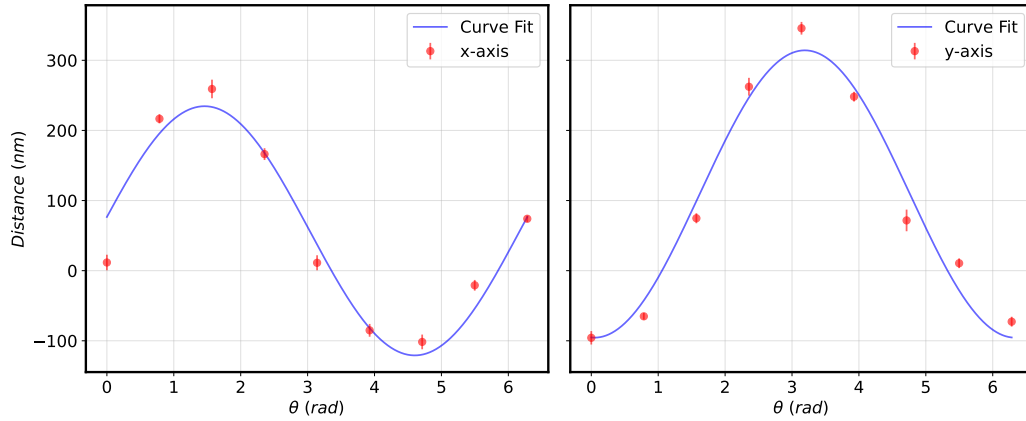


Figure 3.15: Trajectory coordinates for a particle undergoing rotation by the Bean Beam and corresponding fits according to the analysis described in the main text. This data yields a trajectory radius of $R = 0.18\,\mu\text{m}$ and a Bean Beam NA $= 0.46$, in agreement with later measurements in the dark focus tweezer experiment.

## 3.5 Discussion

The addition of structured light beams brings new functionalities to the optical manipulation toolbox. Beyond the static harmonic confining potentials, it is possible to explore non-linear potentials to study the limitations of classical thermodynamics in overdamped systems (such as stochastic heat engines [68]) and in underdamped regimes. In underdamped situations, the surrounding gas is not in thermal equilibrium with the levitated particle, which can provide an experimental platform for new insights into stochastic processes in non-equilibrium physics [69].

Structured light can also be used to implement time-dependent forces. For a periodic set of calculated patterns displayed automatically on SLM's screen, it is possible to create optical beams whose intensity distribution varies in time, as we did to induce motion in the Bean Beam experiment. Due to the limitations of SLM's refresh rate discussed in Section 2.5, modulation frequency cannot

be higher than 60 Hz. However, with the recent advances in nanomaterials and active photonics, spatial light modulators based on thin organic films can reach modulation frequencies as high as 50 MHz [70]. This promising active medium can be used as a high-frequency amplitude modulator in the future – even as a cooling actuator in parametric feedback systems [23, 71, 72], since it can modulate laser beam intensity faster than the particle's natural oscillation frequency achieved in levitated systems [73–75]

Note that the induced rotation generated in the Bean Beam experiment is due to the variation of the relative phase between the $LG_{0,0}$ and $LG_{0,1}$ modes, and not because of a transfer of orbital angular momentum (OAM) between light and matter. Although $LG_{0,1}$ presents an angular momentum of $\hbar$ per photon, to observe a rotation effect the target must be able to convert OAM states of light and yet be transparent enough to enable optical confinement. This happens for anisotropic and inhomogeneous materials, for example q-plates. As we utilize the same kind of $SiO_2$ microparticles during this entire work, we were not able to see such effects.

As discussed in Section 2.6 there is also a third force component due to light's circular polarization that is not explored in this work. The first experiments exploring the exchange of spin angular momentum (SAM) with waveplates dated back almost a hundred years [2] and even today it is widely repeated especially in levitated systems where nanodumbells may reach rotation frequencies of GHz [76]. Polarization is another degree of freedom that can be shaped spatially within a trapping beam and compose a more general class of light fields, commonly known as vector beams. Combining amplitude, phase and polarization modulations facilitates joint orbital and spin angular momentum modification in two- and three-dimensional structured light landscapes being of great interest for trapping polarization-sensitive objects in future applications [28].

# 4
# Dark Tweezers

As first observed by Arthur Ashkin, a Gaussian beam repels air droplets immersed in water [3]. This effect is a demonstration of the repulsive interaction that occurs when the refractive index of the particle is smaller than that of its surrounding medium, $n_p < n_m$. Within the knowledge of engineered optical beams, we can also explore these repulsive optical forces to create an optical trap. As presented in Chapter 2, the OBB is a structured beam with a dark central region surrounded by light in all directions. The idea is to have a particle inside the OBB being subject to multiple repulsion towards an equilibrium point where there is no incidence of light. The dark focus tweezer [34] can present tunable non-harmonic potentials, providing a laboratory for studies of non-linear stochastic dynamics [64, 77]. Moreover, trapping objects in the dark can be extremely beneficial in the fields of active matter and biophysics, where laser damage thresholds limit in-vivo experiments with cells [78–80].

In this chapter we describe the implementation of a dark tweezer for microparticles as the one proposed and theoretically analyzed in [77]. Earlier experiments have employed structured light and optical bottle beams to manipulate atoms in blue-detuned lasers [81–83] and micron-sized objects through photophoretic and thermal forces [84]. Here we demonstrate, to the best of our knowledge for the first time, stable trapping and controlled manipulation of microparticles through optical forces alone, originating from structured light beams forming a dark focus. As we will demonstrate, the DFT induces a strongly non-harmonic potential landscape reflected as non-Gaussianity in the statistical properties of the particle's stochastic trajectory. We probe the particle motion both through the method of power spectrum density formalism as well as potential analysis and reconstruct the optical potential landscape through the matching of data with numerical simulations.

## 4.1
## Experimental setup

The experimental setup for dark tweezers is the same as shown in Fig. 3.1 in Chapter 3 with addition of an auxiliary Gaussian mode. We remove the laser dump in Fig 3.1 and add a telescope (lens L4 and L5) with $L5/L4 = L2/L1$

such that the probe and trapping beam have approximately the same beam radius in order to avoid misplacement in the focal point of the objective. The probe beam thus is reflected in BS2 and using a third half-wave plate $(\lambda/2, 3)$ we control the amount of power sent to the objective. A polarizer is also placed in the front of QPD to filter the scattered beam. Hence, we have access to the information carried by one of the beams alone.
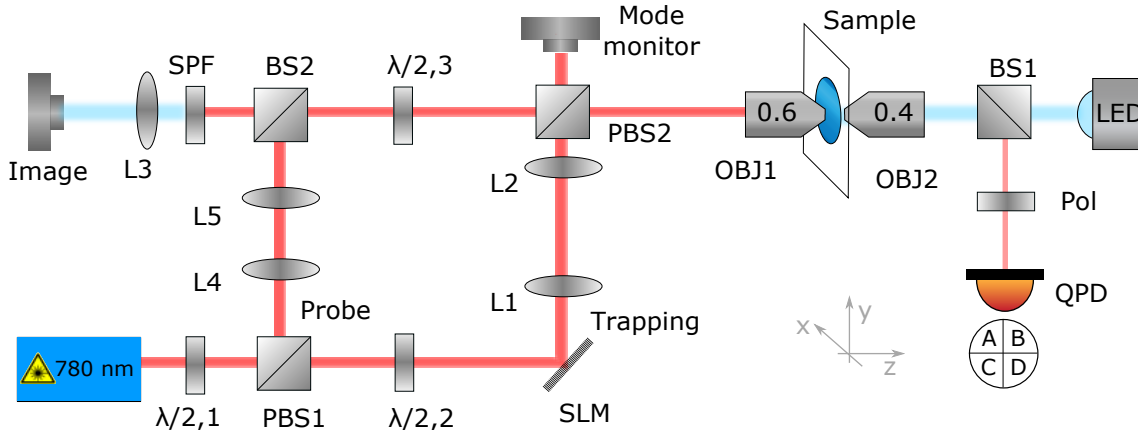


Figure 4.1: Illustrated diagram for experimental optical trapping in a dark focus. Setup is very similar to the one presented in Fig. 3.1 with the addition of an auxiliary beam and a few optical components.

### 4.1.1
### Sample preparation

As we discussed in Chapter 2.6, stable trapping in a dark tweezer requires a medium of refractive index higher than that of the trapped particle. We use silica beads of radius $R = 575\,\text{nm}$ (microParticles GmbH) with refractive index $n_p = 1.45$ at $780\,\text{nm}$. A myriad of possible media exists for this experiment, most notably oils and organic compounds including agar-agar solution and Nujol mineral oil. After careful consideration and tests, clover oil was selected for its refractive index $n_p = 1.53$, relatively low viscosity and convenient antimicrobial properties [85]. The hydrophobic nature of the oil increases the tendency of the silica microspheres to aggregate due to hydrophilic bonds between $SiO_2$ molecules. These ensembles, or microdumbells, appeared a few times in the solution although the experiment was conducted with single microparticles. We measured a clover oil transmission for $780\,\text{nm}$ light of $\eta_{\text{clover}} = 85\%$ which was included in the simulations as a prefactor in the laser power.

Inspired by possible applications in biology, we also tried to prepare samples based on water droplets in oil. Besides being shaped due to environmental conditions and self-propulsion, some microorganisms do not have a rigid structure as a spherical solid and hence an emulsion could be used to emulate

this property inside an optical trap. Moreover, in general, microorganisms have a refractive index very similar to the water [77], thus justifying the use of droplets.

Emulsions were prepared by mixing Nujol oil, water and surfactant. The latter is a chemical compound with hydrophilic and hydrophobic components at each end, responsible for gathering both phases together in a spherical format.

We tried solutions with different concentrations and despite we were able to exert repulsion forces on the particles, we weren't capable of trapping in the DFT due to the natural instability of emulsions and non-homogeneity of the solution, with spheres of several diameters, as shown in Fig. 4.2a. We also observed conglomerates of what we believe to be clusters of droplets that move a large amount of water when traveling trough the sample, Fig. 4.2b.
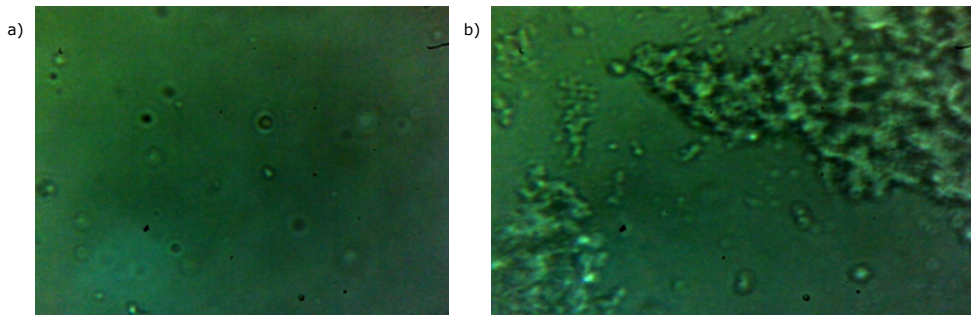


Figure 4.2: Emulsions of oil in water. a) Liquid droplets were non-homogeneous. b) Clusters of droplets disturbing the solution.

### 4.1.2
### Probe beam calibration

In the DFT, a particle is expected to be trapped in the region with no incidence of light, implying a greatly reduced scattering of photons when compared to bright tweezers. The traditional technique of collecting light scattered from the trapping beam as we did in Chapter 3 dos not work for the DFT. To overcome this, we employ an auxiliary probe beam in a Gaussian mode with polarization orthogonal to the trapping beam in such way they do not interfere with one each other.

Being distinguishable and provided it has low power, the probe beam should not significantly alter the properties of the original trap. Moreover, any eventual residual scattering noise due to the trapping beam can be filtered by a polarizer aligned before the detector, as shown in Fig. 4.1, allowing access to the information carried by the probe beam alone.

The alignment of the probe beam was done with the same procedure described in Chapter 3. However, to determine the optimal power of operation

we perform standard Gaussian tweezer experiments with both lasers on. The idea is to probe the particle's movement by reading the scattered light of the auxiliary beam in the QPD. A particle immersed in an aqueous solution is trapped at fixed power of $P_T = 39 \, \text{mW}$. We collect data from QPD and evaluate the PSD which provides a reference corner frequency of $f_c = (428.8 \pm 14) \, \text{Hz}$ (red). We initially turn on the probe beam at $P_P = 91 \, \text{mW}$ and by adjusting the polarizer we find $f_c = (1272.2 \pm 40) \, \text{Hz}$ (blue). Then we progressively decrease the probe beam power. For $P_P = 45 \, \text{mW}$, we have $f_c = (770.8 \pm 19) \, \text{Hz}$ (orange). For $P_P = 19 \, \text{mW}$, we found $f_c = (492.0 \pm 22) \, \text{Hz}$ (green).
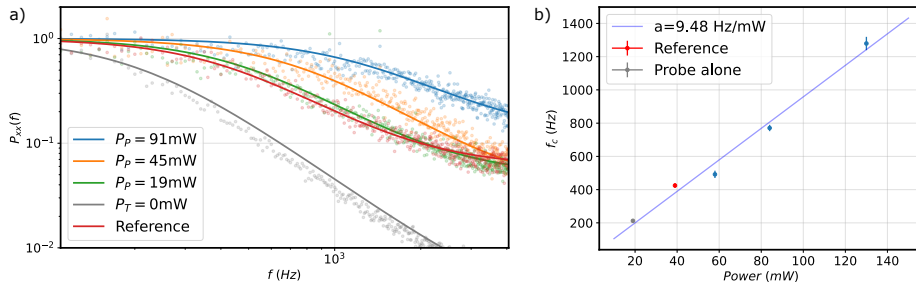


Figure 4.3: Probe beam calibration. a) PSD of probe beam scattering at different intensities for a particle trapped at fixed power $P_T = 39 \, \text{mW}$, with corner frequency $f_c = (428.8 \pm 14) \, \text{Hz}$ (red). The probe beam power $P_P$ is progressively decreased: $P_P = 91 \, \text{mW}$, $f_c = (1272.2 \pm 40) \, \text{Hz}$ (blue); $P_P = 45 \, \text{mW}$, $f_c = (770.8 \pm 19) \, \text{Hz}$ (orange); $P_P = 19 \, \text{mW}$, $f_c = (492.0 \pm 22) \, \text{Hz}$ (green). For comparison, the PSD of the probe beam in the absence of a trap is also shown (grey). Probe beam powers below 19 mW allows for position read-out without significant disturbance to the trap. b) Corner frequency as a function of the total power.

As expected, the measured corner frequency approaches the reference as we decrease the probe beam power. When the reference PSD and probe beam PSD are indistinguishable within error bars, we determine the maximum probe beam power that does not disturb the trap; we find this to be $P_P \leq 19 \, \text{mW}$. For comparison, the PSD of the probe beam in absence of the trapping beam is also shown in grey curve. The minimum power is defined according to the dissipative elements in our experiment in addition to the sensibility of the QPD. We operate near the maximum allowed value in order to increase the signal-noise ratio. All data points as well as the curve fit are displayed in Fig. 4.3 a). Each point is the mean value obtained from 5 PSD's. Each of these PSD's is calculated by averaging 10 measured traces with a sampling frequency of 25kHz. Fig.4.3 b) shows the linear relation between corner frequency and

total power. As the optical beams are orthogonal polarized, optical forces are added together creating a total spring's constant.

## 4.2
## Numerical simulations

To verify the viability of the DFT experiment, we simulate the particle dynamics under realistic parameters. Resulting forces were calculated using the OTT toolbox [50] for an OBB created with a superposition of $LG_{0,0}$ and $LG_{1,0}$ dephased by $\pi$. We consider a trap power of $P = 109\,\mathrm{mW}$ inside the sample and the same particle of $R = 575\,\mathrm{nm}$ as used in the experiment. Fig. 4.4 shows the simulated optical forces in $x$ and $z$ directions for a variety of NA. We observe stronger non-harmonic behavior for lower values of NA and increased amplitude in the optical forces for high values of NA.
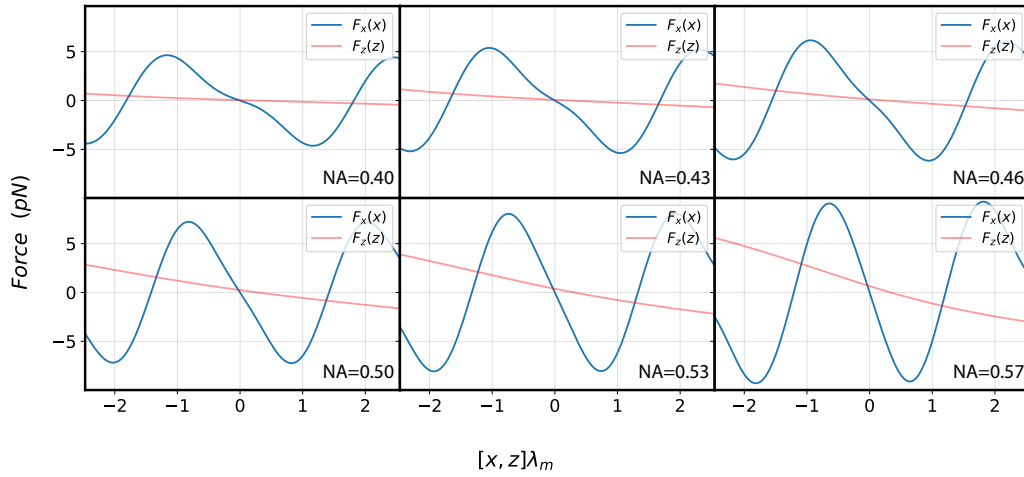


Figure 4.4: Simulated forces acting on a trapped sphere for different laser beam's NA. Curve blue (salmon) shows the force in the $x$ ($z$)direction.

Using the objective lens described in Chapter 3, we can only achieve NA $\leq 0.60$. To achieve maximum NA, we must overfill the objective aperture, but in our case there is a delicate balance between NA and total beam power. If the beam size at the entrance of the objective is too large, unwanted border and diffraction effects start to take place. For this reason we choose to work with a lower NA, producing a trap large enough to accommodate our particles. From beam waist measurements and geometric optics considerations we estimate NA= 0.46.

In our simulations we also consider the effects of the probe beam acting on the sphere by adding an orthogonal-polarized Gaussian mode with $10\,\mathrm{mW}$ of power and NA= 0.46. Fig. 4.5 shows the forces in $x$ and $z$ directions with and without the presence of the probe beam. The top figure displays a decreasing

amplitude in the force acting in the radial direction. Moreover, we can see the Gaussian mode improves the non-harmonic behavior of the force. In the bottom figure, we can see a shift of approximately $0.5\,\mu$m in the equilibrium position in the axial direction due to the action of the additional repulsive probe beam force.
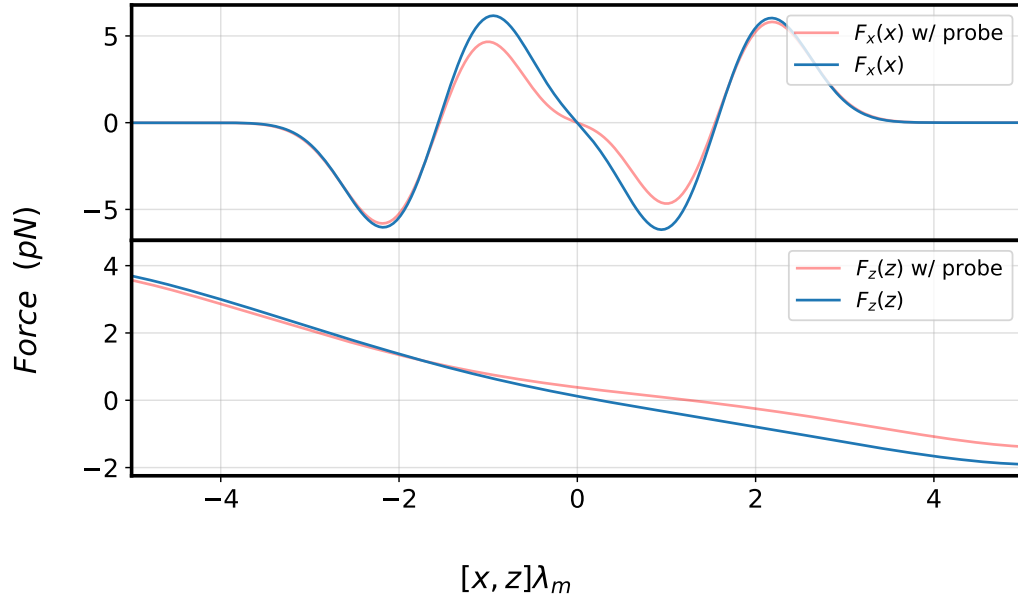
Figure 4.5: Simulated forces on a particle trapped in the OBB on the $x$ (top) and $z$ (bottom) directions. Salmon (blue) color represents the trajectories with (without) action of the probe beam. As expected, the repulsive forces dues to the probe beam decrease the trap depth and shift the equilibrium position aling the axial direction.

Once we know the forces, we can numerically simulate the dynamics of the trapped particle subject to a Langevin equation. Figure 4.6 shows the resulting traces for the $x, y, z$ directions with and without the probe beam. We see the action of the probe beam is to slightly enhance the noise in the $x, y$ directions and shift the equilibrium position along the $z$ direction, as expected.
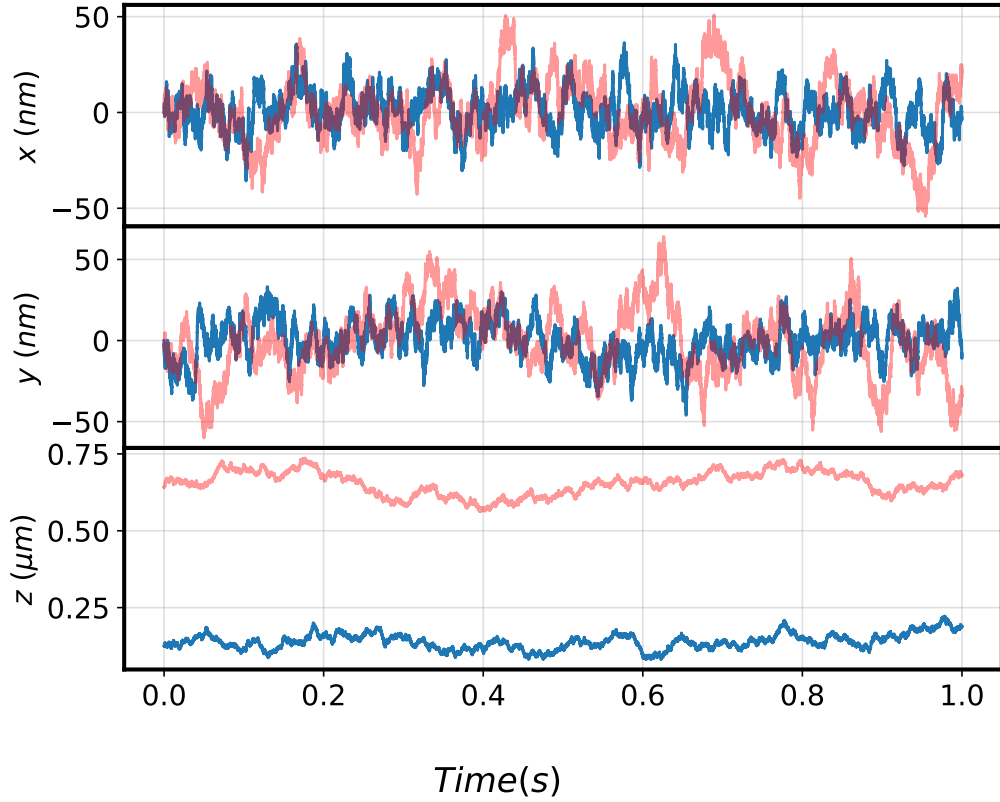
Figure 4.6: Simulated traces of the particle inside DFT for $x, y, z$ direction. Salmon (blue) color represents the trajectories with (without) action of probe beam.

## 4.3
## Non-harmonic potential

As discussed in Section 2.6, for a radius much smaller than the laser wavelength (the dipole regime) $R < \lambda_0/10$, the forces due to a linearly polarized light beam are decomposed into scattering (non-conservative) and gradient (conservative) components.

For the OBB [77], near the origin (i.e. $\rho \ll \omega_0$, $z \ll z_R$), we can expand the potential as a polynomial function,

$$\frac{V(\rho, z)}{V_0} \approx \frac{k_z}{2}z^2 - k_{\rho z}\rho^2 z^2 + \frac{k_\rho}{4}\rho^4, \tag{4-1}$$

where $V_0 = [2\pi n_m R^3 (m^2 - 1)/(c(m^2 + 2))]I_0$, $k_z$, $k_{\rho z}$, $k_\rho$ denote the anharmonic potential strengths. In the dipole regime, these potential parameters are defined in terms of the beam parameters [77],

$$k_z = \frac{4p^2}{z_R^2} \ , \ \ k_{\rho z} = \frac{8p^2(p+1)}{\omega_0^2 z_R^2} \ , \ \ k_\rho = \frac{4p^2}{\omega_0^4} \ . \tag{4-2}$$

In our experiment, particles have a radius of $R = 575\,\text{nm}$, comparable to the wavelength $\lambda_0 = 780\,\text{nm}$, hence the dynamics of a trapped particle must be analyzed numerically via generalized Lorentz-Mie scattering theory. We observe, by simulating the optical potential in this intermediate Lorentz-Mie regime, that the funcional form of the potential in Eq. (4-1) remains the same, albeit with different coefficients from the ones in Eq. 4-2. We can thus use the potential form as an empirical model for the OBB forces.

To validate this polynomial model, we simulated the optical forces considering particles of different radii using the OTT toolbox. We fit a polynomial to the force vectors $f_x$, $f_y$ and $f_z$ obtained from the simulation, returning estimations for each of the components, namely $\hat{f}_x$, $\hat{f}_y$ and $\hat{f}_z$. The quality of the fit in each axis can be evaluated using a root-mean-squared error (RMSE) divided by the root-mean-square force. Finally, an average RMSE over each axis is considered where $N$ represents the number of points used for discretization during simulation,

$$RMSE_{avg} = \frac{1}{3} \sum_{i \in \{x,y,z\}} \left\{ \sqrt{\frac{\sum\limits_{j=1}^{N}(f_i^j - \hat{f}_i^j)^2}{\sum\limits_{j=1}^{N} f_i^{j\,2}}} \right\}, \tag{4-3}$$

Fig. 4.7 shows the $RMSE_{avg}$ as a function of particle radius $R$. Different values of NA were considered to ensure the approximation is valid under variations of the trapping beam focusing. The maximum error encountered is always less than 1.50%, for a particle radius of $350\,\text{nm}$ and an NA of 0.58. For the parameters used in our experiment, the error is 0.416%, validating the quartic potential model within the experimental parameters.
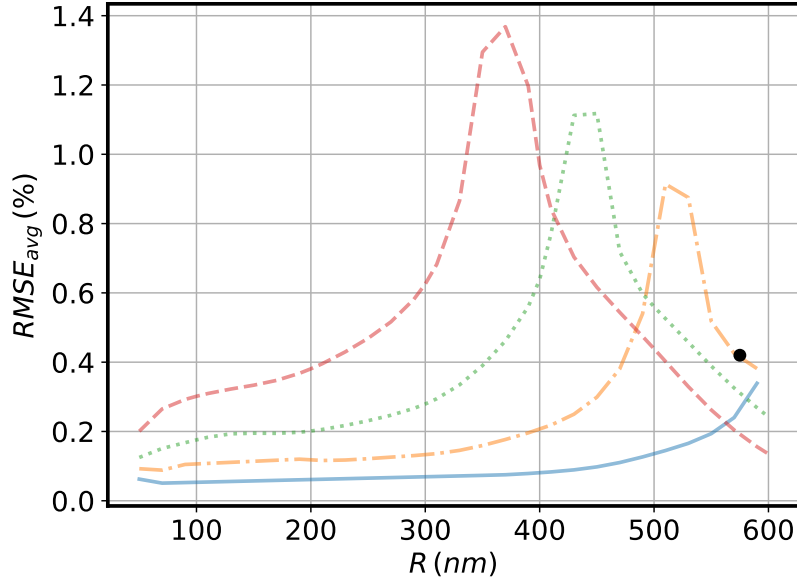
Figure 4.7: $RMSE_{avg}$ of the polynomial fit for the optical forces as a function of the particle radius. Simulations were executed considering NA = 0.40 (——), NA = 0.46 (–··–··), NA = 0.52 (······) and NA = 0.58 (---). The conditions in which the experiment was conducted are represented by the black circle (●).

## 4.4
## Results

### 4.4.1
### Stable trapping

With all the knowledge acquired from numerical simulations and the setup properly aligned, we successfully trapped microparticles in the DFT. As a first evidence of stable trapping, we decided to move the particle in a controlled square trajectory. By adjusting the SLM diffraction angle, we slightly moved the central point of the DFT in the focal plane. Fig. 4.8a-d) shows the iteration of four different trap positions with red dots marking the mean value of a Gaussian distribution in the $x, y$ plane approximately corresponding to the microsphere's center of mass. The trajectory clearly indicates a displacement large enough to be resolved by our imaging system and hence, stable and controllable optical trapping is demonstrated. If the particle is left at a fixed position, it remains there for as long as we let it, up to several hours.

In bright optical tweezers, particles are easily trapped due to the attractive nature of the optical force, but studying a single microparticle for long times can be challenging in a concentrated solution, as additional particles will be

drawn into the trap. Dark tweezers, in contrast, present the opposite effect. Particles trapped in the DFT are shielded from the influence of external objects by a repulsive optical force. This isolation effect allows for arbitrarily long measurements of the particle dynamics. Figs. 4.8e)-h) demonstrates frames of a trapped particle (marked by the white dotted circle) repelling external objects. We observe a microdumbbell (bound pairs of microparticles in the solution, delimited by the black dashed circle) approaching the trapped particle in $t = 0$ and subsequently being repelled by the OBB intensity shield.
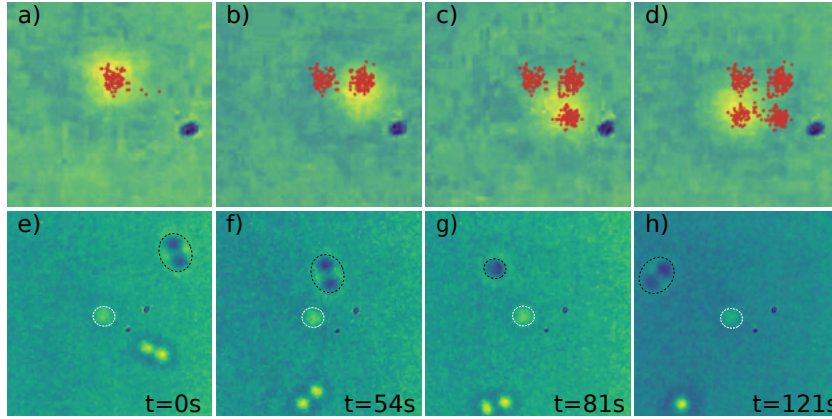


Figure 4.8: a)-d) Stable trapping in the dark focus tweezer: controlled SLM motion of the trapped particle. e)-h) Shielding effect: a dumbbell (black dashed contour) is repelled after approaching a particle trapped (white dashed contour).

## 4.4.2
## PSD analysis

As described in section 3.3, the PSD analysis is one of the most employed techniques to calibrate optical traps due to its simplicity and the possibility of filtering frequency-dependent noise. On the other hand, the shape of the PSD is only precisely known for harmonic potentials, that is, a Lorentzian function. For non-harmonic potentials, such as the DFT, no analytical form of the PSD is known beyond perturbation theory [64].

Nevertheless, numerical simulations of a trapped particle in a quartic potential show that the PSD of the particle motion is well fitted by a Lorentzian function, despite the exact relation between the effective corner frequency $f_{c,DFT}$ of the fit and the trap stiffness is unknown [64]. In fact, the PSD method cannot be directly used to calibrate DFT but we can associate a fitted corner frequency to another beam parameter, the beam's NA, that describes the dark focus dimensions. We verify this effective corner frequency as a consistency check between numerical simulations of the particle in the DFT and experimental

data acquired with the probe beam. Fig. 4.9 shows a typical PSD curve for simulated dynamics in $x$ (left) and $z$ (right) directions for a trapped particle in the DFT. Simulations were made using NA= 0.50, finding $f_{c,x} = (46.0 \pm 8.9)\,\mathrm{Hz}$ and $f_{c,z} = (6.7 \pm 2.4)\,\mathrm{Hz}$. These traces are obtained by taking the mean value of three simulated PSD.
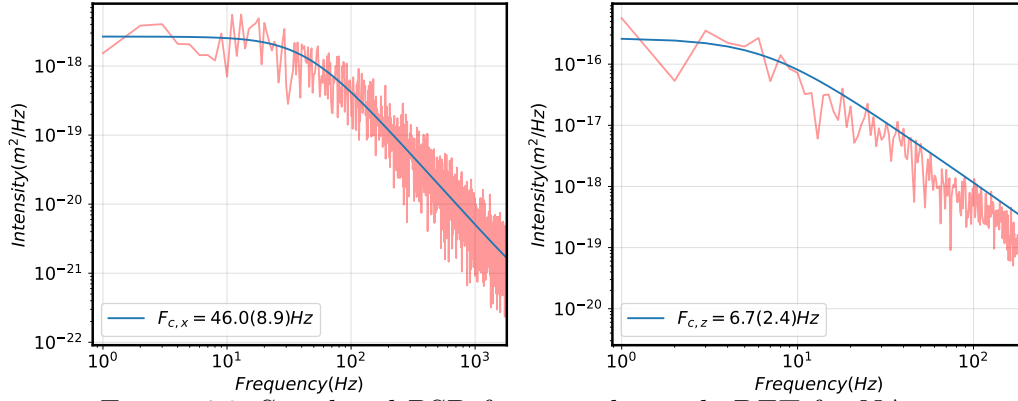


Figure 4.9: Simulated PSD for particle inside DFT for NA= 0.50. Left (right) figure shows the PSD for $x$ ($z$) direction.

Since the probe beam is essential for measuring high sampling rate position data, we also simulated how the PSD changes under its presence for various NA's, as shown in Fig. 4.10. An approximately linear relation between the effective corner frequency and NA is found in the presented interval, $f_{c,DFT} = a\mathrm{NA} + b$. Hence, assuming the relation of NA with width $W$ and height $H$ of the OBB presented in Section 2.4 we can write,

$$W = 2\omega_0 = \frac{2\lambda_0}{\pi\mathrm{NA}} = \frac{2\lambda_0}{\pi\left(\frac{f_{c,DFT}-b}{a}\right)}, \tag{4-4a}$$

$$H = 2z_R = \frac{2n_m\lambda_0}{\pi\mathrm{NA}^2} = \frac{2n_m\lambda_0}{\pi\left(\frac{f_{c,DFT}-b}{a}\right)^2}. \tag{4-4b}$$

These empirical equations reflect a relation between the effective corner frequency and the DFT's dimensions. As the dark focus area decreases, the particle experience higher corner frequencies. Parameters $a$ and $b$ were obtained by fitting a straight line to the simulations accounting for the probe beam (blue curve) in Fig. 4.10, where we find $a = 423.1\,\mathrm{Hz}$ and $b = -179.2\,\mathrm{Hz}$.

Once we measure the effective corner frequency $f_{c,DFT}$ by fitting a Lorentzian curve to the experimental results of the PSD, we can estimate the width and height of the dark optical trap. Figure 4.11 shows the measured PSD of a trapped particle (red dots) and the corresponding fit (red line), together
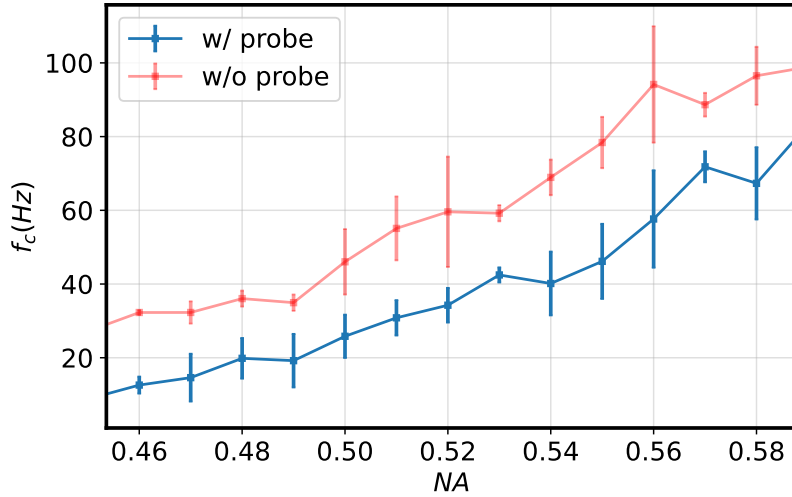
Figure 4.10: Corner frequency $f_c$ of simulated dynamics with (blue) and without (red) the probe beam.

with the background scattering noise (grey dots and line) for comparison. Curves are normalized according to the maximum point of the red line.

We fit a Lorentzian curve to the PSD of the red curve, yielding an effective corner frequency of $f_{c,OBB} = (13.4 \pm 0.7)\,\mathrm{Hz}$ which according to simulations corresponds to an NA between $0.45 - 0.49$. From our empirical Eq. (4-4), we find a $W = (1.09 \pm 0.1)\,\mu\mathrm{m}$ suggesting our particle of diameter $1.15\,\mu\mathrm{m}$ is subject to loose forces within the dark focal region.

Note that this relation does not calibrate the optical trap by itself since it does not provide the parameters of Eq. (4-1). We are mainly comparing the curve fit of the PSD experimental data with simulations in order to estimate the beam's NA, but we don't have enough information to describe the coupled term, for instance. In the next section, we apply the potential analysis formalism as an independent calibration technique leading us to the same NA interval, which demonstrates consistency between both approaches. Moreover, we will be able to record a three-dimensional trace of the particle and fit the parameters of the polynomial potential by performing the potential analysis as described in Section 3.2.
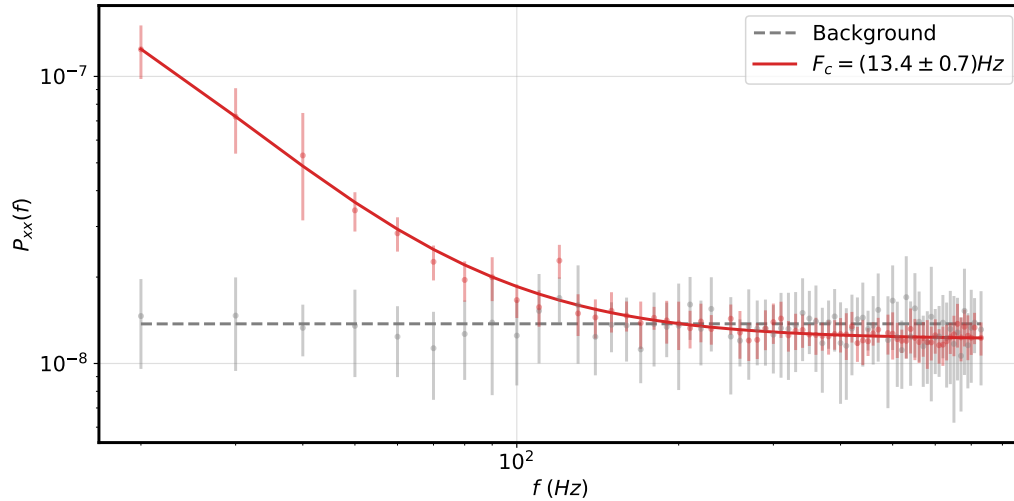
Figure 4.11: PSD of a particle trapped in the dark focus (red) in comparison to background noise (grey).

### 4.4.3
### Potential analysis

As discussed in Section 3.2, potential analysis can be used to calibrate any conservative force that can confine a particle in an equilibrium point, being a promising technique to calibrate the DFT.

Images of the trapped particle are captured by using a previously calibrated CCD camera, the Image Camera discussed in Section 2.5 and shown in Fig.4.1, at a rate of 15.0 frames/s. We extract the particle's centroid and axial coordinates using image processing techniques [53]. Resulting traces can be seen in Fig. 4.12. We note these traces are not Gaussian distributed, as can be directly verified by performing statistical hypothesis tests.
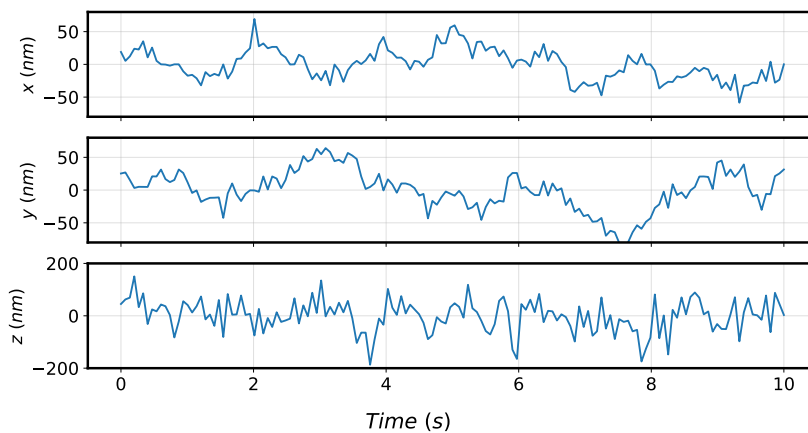


Figure 4.12: Traces of the particle inside the DFT

We acquired a long-duration video of the experiment, from which we

obtain a position probability density function (PDF). As a cross-check, we compare the marginal PDFs of motion along the $x$ and $y$ directions with those obtained from numerical simulations considering different values of the trap NA. We ran several traces of the DFT as a function of NA and find the best match through the minimum value of Kullback–Leibler (KL) divergence as shown in Fig. 4.13. The average value between both directions points to the NA interval between $0.44 - 0.47$ as best describing the measured data. Note that this interval agreed with the interval found in the PSD analysis, this confirms an optimal interval between $0.46 - 0.47$ for describing our experimental results. We selected NA$= 0.46$ for its smaller KL value. The PDF was fitted assuming $P(\rho, z) \propto \exp\left(-V(\rho, z)/k_B T\right)$ where $V(\rho, z)$ is the polynomial potential model described in Eq. (4-1) and it is shown in Fig. 4.14a). This distribution allows us to reconstruct the DFT potential at the trapped sphere's centroid position, obtained by taking the logarithm of the PDF, shown in Fig. 4.14b). A potential depth of $\approx 100 \times k_B T$ is found, evidencing stable trapping. The corresponding fit parameters are shown in Table 1 for the experimental and numerical simulations.
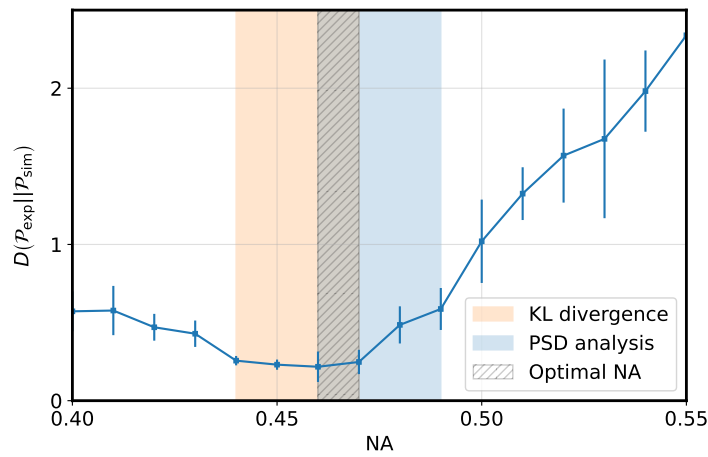
Figure 4.13: Kullback-Leibler divergence $D(\mathcal{P}_{\mathrm{exp}}||\mathcal{P}_{\mathrm{sim}})$ between simulation and experiment as functions of the NA. Area marked in orange reveals the range where both distributions are most similar.
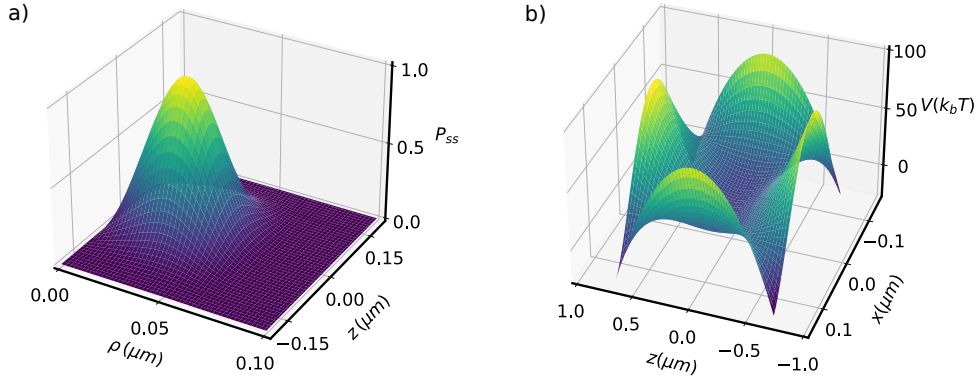
Figure 4.14: Reconstructed potential. a) Fitted normalized PDF of the centroid's position. b) Reconstructed potential landscape for centroid coordinate of a trapped particle in the DFT.

| Parameter | Experiment | Lorentz-Mie simulation |
|-----------|------------|------------------------|
| $k_z$ (N/m) | $(3.86 \pm 0.06) \times 10^{-7}$ | $(2.93 \pm 0.79) \times 10^{-7}$ |
| $k_{\rho z}$ (N/m$^3$) | $(8.81 \pm 0.14) \times 10^7$ | $(8.84 \pm 0.25) \times 10^7$ |
| $k_\rho$ (N/m$^3$) | $(2.26 \pm 0.07) \times 10^8$ | $(1.63 \pm 0.17) \times 10^8$ |

Table 4.1: Reconstructed potential parameters in comparison to numerical simulations of Lorentz-Mie theory. Error bars are obtained by dividing the experimental and simulated data into five sets and taking the standard deviation.

## 4.5 Discussion

In summary, we have implemented a stable structured dark focus optical trap for dielectric microparticles immersed in a high refractive index medium. We have shown stable trapping and isolation from surrounding objects by repulsive optical forces, which induce a non-harmonic potential landscape. We also study the optical potential both through the PSD and potential analysis, and reconstruct the potential parameters in agreement with Lorentz-Mie numerical simulation of the optical trap.

We expect the dark trap will find applications both in fundamental and applied physics. As further discussed in Chapter 5, dark traps could be extended to vacuum levitodynamics through the use of engineered nano and microparticles [86], where the structured light beam could offer controlled or even reduced photon scattering in coherent quantum experiments [87, 88].

Finally, as also discussed in Chapter 5, dark tweezers can provide stable trapping for organisms with greatly reduced laser heating, further extending the optical manipulation toolbox for living matter avoiding laser damage thresholds in living microorganisms [80].

# 5
# Outlook

In this work, we have explored the use of structured light beams in optical tweezers. We have explored both the regime of bright tweezers, where the refractive index of the trapped object is higher than that of its surrounding medium, and the novel regime of dark tweezers, where the refractive index of the medium is higher than that of the object. We presented different experiments employing structured light in both cases, and notably we implemented, to the best of our knowledge, the fist stable dark optical tweezer for micron-sized particles. We have introduced novel methods for characterizing important parameters of the trapping beam as well as the optical potential. From where we stand, several future research directions can be envisioned. We briefly discuss some of these future ideas.

## Dark focus tweezer in vacuum

Ground state cooling has been recently achieved in experiments based on optimal feedback control [23] and coherent scattering [22]. Both these routes to the ground state require operation at high vacuum pressures (below $10^{-8}$ mbar) to reduce damping rates. At this level of environmental isolation, the major sources of decoherence come from photon recoil heating induced by trapping Gaussian beam [87–89] and the black body temperature of the levitated object. Dark tweezers can present an interesting solution to the latter issue by reducing the direct incidence of photons to the trapped particle and hence its bulk temperature. To apply dark focus tweezers to nano- and microparticles, however, we need to overcome the fact that the refractive index of the vacuum is $n_m = 1$.

An interesting possibility is to use nanoparticles doped with atoms that have a transition near the frequency of the trapping beam [90]. In that case, if the trap is blue-detuned with respect to the transition, the atoms will acquire a negative polarizability and provided the doping level is high enough, the nanosphere will be subject to a repulsive force. Decompose the total dipole of such a system according to,

$$\tilde{\boldsymbol{p}} = \tilde{\boldsymbol{p}}_{np} + \tilde{\boldsymbol{p}}_{oc} = \tilde{\alpha}_{np}(\omega)\boldsymbol{E} + \tilde{\alpha}_{oc}(\omega)\boldsymbol{E}, \tag{5-1}$$

where the $\tilde{\alpha}_{np}$ is the complex polarizability of the nanoparticle's bulk material, i.e. $SiO_2$, and $\tilde{\alpha}_{oc}$ is the polarizability associated with an ensemble of optical centers (the atoms) confined in the same volume $V$. Trapping in a dark tweezer requires the effects assosiated to $\tilde{\alpha}_{oc}$ to be larger than those of $\tilde{\alpha}_{np}$. It has been shown that the polarizability of rare-earth ions doped nanocrystals can assume negative values for a blue-detuned wavelength near the optical transition at 972 nm [91]. Moreover, experiments with NV centers presented an increase in the overall trapping force due to collective effects even in a noisy liquid environment [92]. For a blue-detuned laser and assuming the optical centers' effect can be higher than the nanocrystal's bulk, it is then possible to trap objects in a dark tweezer in vacuum.

## Optical binding

Beyond the arbitrary potentials that a phase modulator can induce in a single particle, one can engineer an optical beam with multiple equilibrium points in order to have arrays of optical tweezers [60, 93]. The emerging field of simultaneous trapping of multiple particles promises to lead optomechanics to a new level by exploring not only the light-matter interaction but the light-induced matter-matter interactions in well-isolated systems [94].

A step towards controllable optical interactions between nanoparticles has been recently demonstrated [95], where coherent scattering interaction between levitated nanoparticles was measured as a function of different controllable parameters such as distance, the tweezer's relative phase and polarization. Structured light tweezers add possibilities to this kind of experiment, making it possible to control the scattering of light by mode engineering both in the Rayleigh and intermediate regime.

## Biophysics

Cell membranes are responsible for a series of vital processes ranging from self-division (as in cytokinesis) to absorbing and expelling motions (endocytosis and exocytosis). It also plays a crucial role in motility, signal sensing and the primordial function of protecting the cell's internal environment. Despite being well-known, these processes have no complete mechanical description, even though it is widely believed that acquiring such understanding might lead to valuable insights into the functioning of living beings [13, 16, 96]. The first step

in this direction is to study the membrane's response to external forces. Optical tweezers are a particularly suitable tool to study the physical properties of single microorganisms since it is capable of probing forces at femtonewtons in a range of nano and micron scales

Although a variety of different experiments have been done with cell membranes in the last years [12–15], the data reported in the literature for mechanical properties of living organisms differ by one to three orders of magnitude due to several error sources from experimental issues, such as cell culture conditions or the natural variability of these cells, to imprecise theoretical models. Moreover, a Gaussian optical tweezer induces a high energy density into the microorganisms due to the direct interaction with the highly focused laser beam which can damage the microorganisms during the application and even modify the results of the experiment [80]. A possible approach is to use dark tweezers to confine the target in a region with greatly reduced incidence of light. Assuming a living cell has a refractive index within the range $1.36 - 1.39$ [77], we should find a non-toxic medium such that $n_m > 1.39$. Being highly water-soluble, Iodixanol has been reported as a compound that can tune the refractive index of water to 1.43 without harming the specimens [97]. It would be possible to analyze the motion of the microorganisms with the potential analysis method discussed in Chapter 3 and 4. Furthermore, one could change the dark focus dimensions to study its dynamics or even the cytokinesis process under different levels of optical stress.

Other than optically trapping living cells and measuring their mechanical properties, one can use gradient forces to guide neuronal growth in vitro [79]. For a suitable laser power, it was shown that a lamellipodia - membrane protrusions on the front edge of a motile cell, such as neurons and immune cells - has an enhancing growth into the beam focus, presenting opportunities to control a natural biological process with a simple technique that does not involve any chemical compound or external interactions

We may extend this idea by using structured light beams. Two initially separated neurons can be guided to an intersection point via an engineered beam where they naturally form synapses that can be seen in a high-resolution microscope, as implemented in Chapter 3. Moreover, the fact that neurons grown in a bottom of a thick coverslip suggests the use of external electrodes [98, 99] to measure their emitted signals and hence demonstrate the formation of synapses. The idea of guiding multiple neurons is a first step towards human-controlled neuronal structures that, as a long-term objective, can be applied in nerve repairs of in vivo experiments [79].

# Bibliography

[1] E. F. Nichols and G. F. Hull, "The pressure due to radiation," *Proceedings of the American Academy of Arts and Sciences*, vol. 38, no. 20, p. 559, 1903. [Online]. Available: https://doi.org/10.2307/20021808

[2] R. A. Beth, "Mechanical detection and measurement of the angular momentum of light," *Physical Review*, vol. 50, no. 2, pp. 115–125, Jul. 1936. [Online]. Available: https://doi.org/10.1103/physrev.50.115

[3] A. Ashkin, "Acceleration and trapping of particles by radiation pressure," *Physical review letters*, vol. 24, no. 4, p. 156, 1970.

[4] A. Ashkin, J. M. Dziedzic, J. E. Bjorkholm, and S. Chu, "Observation of a single-beam gradient force optical trap for dielectric particles," *Optics Letters*, vol. 11, no. 5, p. 288, May 1986. [Online]. Available: https://doi.org/10.1364/ol.11.000288

[5] A. Ashkin, "Forces of a single-beam gradient laser trap on a dielectric sphere in the ray optics regime," *Biophysical Journal*, vol. 61, no. 2, pp. 569–582, Feb. 1992. [Online]. Available: https://doi.org/10.1016/s0006-3495(92)81860-x

[6] S. Chu, J. E. Bjorkholm, A. Ashkin, and A. Cable, "Experimental observation of optically trapped atoms," *Physical Review Letters*, vol. 57, no. 3, pp. 314–317, Jul. 1986. [Online]. Available: https://doi.org/10.1103/physrevlett.57.314

[7] W. D. Phillips, "Nobel lecture: Laser cooling and trapping of neutral atoms," *Reviews of Modern Physics*, vol. 70, no. 3, pp. 721–741, Jul. 1998. [Online]. Available: https://doi.org/10.1103/revmodphys.70.721

[8] A. Ashkin and J. M. Dziedzic, "Optical levitation by radiation pressure," *Applied Physics Letters*, vol. 19, no. 8, pp. 283–285, Oct. 1971. [Online]. Available: https://doi.org/10.1063/1.1653919

[9] C. Gonzalez-Ballestero, M. Aspelmeyer, L. Novotny, R. Quidant, and O. Romero-Isart, "Levitodynamics: Levitation and control of microscopic

objects in vacuum," *Science*, vol. 374, no. 6564, Oct. 2021. [Online]. Available: https://doi.org/10.1126/science.abg3027

[10] A. Ashkin and J. M. Dziedzic, "Optical trapping and manipulation of viruses and bacteria," *Science*, vol. 235, no. 4795, pp. 1517–1520, Mar. 1987. [Online]. Available: https://doi.org/10.1126/science.3547653

[11] A. Ashkin, J. M. Dziedzic, and T. Yamane, "Optical trapping and manipulation of single cells using infrared laser beams," *Nature*, vol. 330, no. 6150, pp. 769–771, Dec. 1987. [Online]. Available: https://doi.org/10.1038/330769a0

[12] G. R. d. S. Araújo, N. B. Viana, F. Gómez, B. Pontes, and S. Frases, "The mechanical properties of microbial surfaces and biofilms," *The Cell Surface*, vol. 5, p. 100028, 2019.

[13] B. Pontes, Y. Ayala, A. C. C. Fonseca, L. F. Romão, R. F. Amaral, L. T. Salgado, F. R. Lima, M. Farina, N. B. Viana, V. Moura-Neto, and H. M. Nussenzveig, "Membrane elastic properties and cell function," *PLoS ONE*, vol. 8, no. 7, p. e67708, Jul. 2013. [Online]. Available: https://doi.org/10.1371/journal.pone.0067708

[14] Y. A. Ayala, B. Pontes, D. S. Ether, L. B. Pires, G. R. Araujo, S. Frases, L. F. Romão, M. Farina, V. Moura-Neto, N. B. Viana, and H. M. Nussenzveig, "Rheological properties of cells measured by optical tweezers," *BMC Biophysics*, vol. 9, no. 1, Jun. 2016. [Online]. Available: https://doi.org/10.1186/s13628-016-0031-4

[15] A. Kamgoué, J. Ohayon, and P. Tracqui, "Estimation of cell young's modulus of adherent cells probed by optical and magnetic tweezers: Influence of cell thickness and bead immersion," *Journal of Biomechanical Engineering*, vol. 129, no. 4, pp. 523–530, Dec. 2006. [Online]. Available: https://doi.org/10.1115/1.2746374

[16] G. Y. Lee and C. T. Lim, "Biomechanics approaches to studying human diseases," *Trends in Biotechnology*, vol. 25, no. 3, pp. 111–118, Mar. 2007. [Online]. Available: https://doi.org/10.1016/j.tibtech.2007.01.005

[17] T. Westphal, H. Hepach, J. Pfaff, and M. Aspelmeyer, "Measurement of gravitational coupling between millimetre-sized masses," *Nature*, vol. 591, no. 7849, pp. 225–228, Mar. 2021. [Online]. Available: https://doi.org/10.1038/s41586-021-03250-7

[18] A. A. Geraci, S. B. Papp, and J. Kitching, "Short-range force detection using optically cooled levitated microspheres," *Physical Review Letters*, vol. 105, no. 10, Aug. 2010. [Online]. Available: https://doi.org/10.1103/physrevlett.105.101101

[19] D. delToro and D. E. Smith, "Accurate measurement of force and displacement with optical tweezers using DNA molecules as metrology standards," *Applied Physics Letters*, vol. 104, no. 14, p. 143701, Apr. 2014. [Online]. Available: https://doi.org/10.1063/1.4871005

[20] Y. Mo, M. Fizari, K. Koharchik, and D. E. Smith, "Determining trap compliances, microsphere size variations, and response linearities in single DNA molecule elasticity measurements with optical tweezers," *Frontiers in Molecular Biosciences*, vol. 8, Mar. 2021. [Online]. Available: https://doi.org/10.3389/fmolb.2021.605102

[21] C. Gonzalez-Ballestero, P. Maurer, D. Windey, L. Novotny, R. Reimann, and O. Romero-Isart, "Theory for cavity cooling of levitated nanoparticles via coherent scattering: Master equation approach," *Physical Review A*, vol. 100, no. 1, Jul. 2019. [Online]. Available: https://doi.org/10.1103/physreva.100.013805

[22] U. Delić, M. Reisenbauer, K. Dare, D. Grass, V. Vuletić, N. Kiesel, and M. Aspelmeyer, "Cooling of a levitated nanoparticle to the motional quantum ground state," *Science*, vol. 367, no. 6480, pp. 892–895, Feb. 2020. [Online]. Available: https://doi.org/10.1126/science.aba3993

[23] L. Magrini, P. Rosenzweig, C. Bach, A. Deutschmann-Olek, S. G. Hofer, S. Hong, N. Kiesel, A. Kugi, and M. Aspelmeyer, "Real-time optimal quantum control of mechanical motion at room temperature," *Nature*, vol. 595, no. 7867, pp. 373–377, Jul. 2021. [Online]. Available: https://doi.org/10.1038/s41586-021-03602-3

[24] J. Piotrowski, D. Windey, J. Vijayan, C. Gonzalez-Ballestero, A. de los Ríos Sommer, N. Meyer, R. Quidant, O. Romero-Isart, R. Reimann, and L. Novotny, "Simultaneous ground-state cooling of two mechanical modes of a levitated nanoparticle," *Nature Physics*, Mar. 2023. [Online]. Available: https://doi.org/10.1038/s41567-023-01956-1

[25] H. Rubinsztein-Dunlop, A. Forbes, M. V. Berry, M. R. Dennis, D. L. Andrews, M. Mansuripur, C. Denz, C. Alpmann, P. Banzer, T. Bauer, E. Karimi, L. Marrucci, M. Padgett, M. Ritsch-Marte, N. M. Litchinitser,

N. P. Bigelow, C. Rosales-Guzmán, A. Belmonte, J. P. Torres, T. W. Neely, M. Baker, R. Gordon, A. B. Stilgoe, J. Romero, A. G. White, R. Fickler, A. E. Willner, G. Xie, B. McMorran, and A. M. Weiner, "Roadmap on structured light," *Journal of Optics*, vol. 19, no. 1, p. 013001, Nov. 2016. [Online]. Available: https://doi.org/10.1088/2040-8978/19/1/013001

[26] M. Beijersbergen, R. Coerwinkel, M. Kristensen, and J. Woerdman, "Helical-wavefront laser beams produced with a spiral phaseplate," *Optics Communications*, vol. 112, no. 5-6, pp. 321–327, Dec. 1994. [Online]. Available: https://doi.org/10.1016/0030-4018(94)90638-6

[27] D. GABOR, "A new microscopic principle," *Nature*, vol. 161, no. 4098, pp. 777–778, May 1948. [Online]. Available: https://doi.org/10.1038/161777a0

[28] E. Otte and C. Denz, "Optical trapping gets structure: Structured light for advanced optical manipulation," *Applied Physics Reviews*, vol. 7, no. 4, p. 041308, Dec. 2020. [Online]. Available: https://doi.org/10.1063/5.0013276

[29] Y. Yang, Y. Ren, M. Chen, Y. Arita, and C. Rosales-Guzmán, "Optical trapping with structured light: a review," *Advanced Photonics*, vol. 3, no. 3, p. 034001, 2021.

[30] L. Allen, M. W. Beijersbergen, R. J. C. Spreeuw, and J. P. Woerdman, "Orbital angular momentum of light and the transformation of laguerre-gaussian laser modes," *Physical Review A*, vol. 45, no. 11, pp. 8185–8189, Jun. 1992. [Online]. Available: https://doi.org/10.1103/physreva.45.8185

[31] N. B. Simpson, K. Dholakia, L. Allen, and M. J. Padgett, "Mechanical equivalence of spin and orbital angular momentum of light: an optical spanner," *Optics Letters*, vol. 22, no. 1, p. 52, Jan. 1997. [Online]. Available: https://doi.org/10.1364/ol.22.000052

[32] M. Padgett and R. Bowman, "Tweezers with a twist," *Nature Photonics*, vol. 5, no. 6, pp. 343–348, May 2011. [Online]. Available: https://doi.org/10.1038/nphoton.2011.81

[33] V. Garcés-Chávez, D. McGloin, M. J. Padgett, W. Dultz, H. Schmitzer, and K. Dholakia, "Observation of the transfer of the local angular momentum density of a multiringed light beam to an optically trapped particle," *Physical Review Letters*, vol. 91, no. 9, Aug. 2003. [Online]. Available: https://doi.org/10.1103/physrevlett.91.093602

[34] F. Almeida, I. Sousa, O. Kremer, B. P. da Silva, D. S. Tasca, A. Z. Khoury, G. Temporão, and T. Guerreiro, "Trapping microparticles in a structured dark focus," 2023. [Online]. Available: https://arxiv.org/abs/2302.01953

[35] M. C. T. B. E. A. Saleh, *Fundamentals of Photonics.* Wiley, 2007.

[36] F. Pampaloni and J. Enderlein, "Gaussian, hermite-gaussian, and laguerre-gaussian beams: A primer," 2004. [Online]. Available: https://arxiv.org/abs/physics/0410021

[37] A. T. O'Neil, I. MacVicar, L. Allen, and M. J. Padgett, "Intrinsic and extrinsic nature of the orbital angular momentum of a light beam," *Physical Review Letters*, vol. 88, no. 5, Jan. 2002. [Online]. Available: https://doi.org/10.1103/physrevlett.88.053601

[38] B. P. da Silva, V. Pinillos, D. Tasca, L. Oxman, and A. Khoury, "Pattern revivals from fractional gouy phases in structured light," *Physical Review Letters*, vol. 124, no. 3, Jan. 2020. [Online]. Available: https://doi.org/10.1103/physrevlett.124.033902

[39] J. Arlt and M. J. Padgett, "Generation of a beam with a dark focus surrounded by regions of higher intensity: the optical bottle beam," *Optics letters*, vol. 25, no. 4, pp. 191–193, 2000.

[40] B. Pinheiro, "Padrões ressurgentes em luz estruturada," Ph.D. dissertation, Universidade Federal Fluminense, 2021.

[41] B. Melo, "Cavities and tweezers: Developing tools for an optomechanics laboratory." Master's thesis, Pontifícia Universidade Católica do Rio de Janeiro, 2019.

[42] J. Pavlin, N. Vaupotič, and M. Čepič, "Liquid crystals: a new topic in physics for undergraduates," *European Journal of Physics*, vol. 34, no. 3, pp. 745–761, Apr. 2013. [Online]. Available: https://doi.org/10.1088/0143-0807/34/3/745

[43] B. R. Boruah, "Dynamic manipulation of a laser beam using a liquid crystal spatial light modulator," *American Journal of Physics*, vol. 77, no. 4, pp. 331–336, Apr. 2009. [Online]. Available: https://doi.org/10.1119/1.3054349

[44] A. Forbes, A. Dudley, and M. McLaren, "Creation and detection of optical modes with spatial light modulators," *Advances in Optics and Photonics*, vol. 8, no. 2, p. 200, Apr. 2016. [Online]. Available: https://doi.org/10.1364/aop.8.000200

[45] J. Jackson, *Classical Electrodynamics. New York: John Wiley& Sons.* Inc, 1998.

[46] P. Jones, O. Maragó, and G. Volpe, *Optical tweezers.* Cambridge University Press Cambridge, UK, 2015.

[47] S. M. Barnett, "Resolution of the abraham-minkowski dilemma," *Physical Review Letters*, vol. 104, no. 7, Feb. 2010. [Online]. Available: https://doi.org/10.1103/physrevlett.104.070401

[48] I. Brandão, "Harnessing optomechanical interactions: From trapping organisms to entangling nanospheres." Master's thesis, Pontifícia Universidade Católica do Rio de Janeiro, 2021.

[49] D. J. Griffiths, *Introduction to Electrodynamics.* Cambridge University Press, Jun. 2017. [Online]. Available: https://doi.org/10.1017/9781108333511

[50] T. A. Nieminen, V. L. Loke, A. B. Stilgoe, G. Knöner, A. M. Brańczyk, N. R. Heckenberg, and H. Rubinsztein-Dunlop, "Optical tweezers computational toolbox," *Journal of Optics A: Pure and Applied Optics*, vol. 9, no. 8, p. S196, 2007.

[51] L. M. Manojlović, "Quadrant photodetector sensitivity," *Applied Optics*, vol. 50, no. 20, p. 3461, Jul. 2011. [Online]. Available: https://doi.org/10.1364/ao.50.003461

[52] L. Novotny and B. Hecht, *Principles of Nano-Optics.* Cambridge University Press, Sep. 2012. [Online]. Available: https://doi.org/10.1017/cbo9780511794193

[53] D. A. Forsyth and J. Ponce, *Computer vision: a modern approach.* prentice hall professional technical reference, 2002.

[54] R. C. Gonzalez and R. E. Woods, *Digital image processing.* Upper Saddle River, N.J.: Prentice Hall, 2008. [Online]. Available: http://www.worldcat.org/search?qt=worldcat_org_all&q=013505267X

[55] J. Gieseler, J. R. Gomez-Solano, A. Magazzù, I. P. Castillo, L. P. García, M. Gironella-Torrent, X. Viader-Godoy, F. Ritort, G. Pesce, A. V. Arzola, K. Volke-Sepúlveda, and G. Volpe, "Optical tweezers — from calibration to applications: a tutorial," *Advances in Optics and Photonics*, vol. 13, no. 1, p. 74, Mar. 2021. [Online]. Available: https://doi.org/10.1364/aop.394888

[56] K. Berg-Sørensen and H. Flyvbjerg, "Power spectrum analysis for optical tweezers," *Review of Scientific Instruments*, vol. 75, no. 3, pp. 594–612, Mar. 2004. [Online]. Available: https://doi.org/10.1063/1.1645654

[57] E. M. Purcell, "Life at low reynolds number," *American Journal of Physics*, vol. 45, no. 1, pp. 3–11, Jan. 1977. [Online]. Available: https://doi.org/10.1119/1.10903

[58] F. Tebbenjohanns, M. Frimmer, and L. Novotny, "Optimal position detection of a dipolar scatterer in a focused field," *Physical Review A*, vol. 100, no. 4, Oct. 2019. [Online]. Available: https://doi.org/10.1103/physreva.100.043821

[59] C. Gonzalez-Ballestero, J. A. Zielińska, M. Rossi, A. Militaru, M. Frimmer, L. Novotny, P. Maurer, and O. Romero-Isart, "Suppressing recoil heating in levitated optomechanics using squeezed light," 2022. [Online]. Available: https://arxiv.org/abs/2209.05858

[60] T. W. Penny, A. Pontin, and P. F. Barker, "Sympathetic cooling and squeezing of two colevitated nanoparticles," *Physical Review Research*, vol. 5, no. 1, Jan. 2023. [Online]. Available: https://doi.org/10.1103/physrevresearch.5.013070

[61] B. Melo, F. Almeida, G. Temporão, and T. Guerreiro, "Relaxing constraints on data acquisition and position detection for trap stiffness calibration in optical tweezers," *Optics Express*, vol. 28, no. 11, pp. 16 256–16 269, 2020.

[62] C. Braunsmann, V. Prucker, and T. E. Schäffer, "Optical knife-edge displacement sensor for high-speed atomic force microscopy," *Applied Physics Letters*, vol. 104, no. 10, p. 103101, Mar. 2014. [Online]. Available: https://doi.org/10.1063/1.4868043

[63] L. Paterson, M. P. MacDonald, J. Arlt, W. Sibbett, P. E. Bryant, and K. Dholakia, "Controlled rotation of optically trapped microscopic particles," *Science*, vol. 292, no. 5518, pp. 912–914, May 2001. [Online]. Available: https://doi.org/10.1126/science.1058591

[64] B. Suassuna, B. Melo, and T. Guerreiro, "Path integrals and nonlinear optical tweezers," *Physical Review A*, vol. 103, no. 1, Jan. 2021. [Online]. Available: https://doi.org/10.1103/physreva.103.013110

[65] J. Gieseler, L. Novotny, and R. Quidant, "Thermal nonlinearities in a nanomechanical oscillator," *Nature Physics*, vol. 9, no. 12, pp. 806–810, Nov. 2013. [Online]. Available: https://doi.org/10.1038/nphys2798

[66] J. Flajšmanová, M. Šiler, P. Jedlička, F. Hrubý, O. Brzobohatý, R. Filip, and P. Zemánek, "Using the transient trajectories of an optically levitated nanoparticle to characterize a stochastic duffing oscillator," *Scientific Reports*, vol. 10, no. 1, Sep. 2020. [Online]. Available: https://doi.org/10.1038/s41598-020-70908-z

[67] M. T. Cuairan, J. Gieseler, N. Meyer, and R. Quidant, "Precision calibration of the duffing oscillator with phase control," *Physical Review Letters*, vol. 128, no. 21, May 2022. [Online]. Available: https://doi.org/10.1103/physrevlett.128.213601

[68] V. Blickle and C. Bechinger, "Realization of a micrometre-sized stochastic heat engine," *Nature Physics*, vol. 8, no. 2, pp. 143–146, Dec. 2011. [Online]. Available: https://doi.org/10.1038/nphys2163

[69] J. Millen, T. Deesuwan, P. Barker, and J. Anders, "Nanoscale temperature measurements using non-equilibrium brownian dynamics of a levitated nanosphere," *Nature Nanotechnology*, vol. 9, no. 6, pp. 425–429, May 2014. [Online]. Available: https://doi.org/10.1038/nnano.2014.82

[70] I.-C. Benea-Chelmus, M. L. Meretska, D. L. Elder, M. Tamagnone, L. R. Dalton, and F. Capasso, "Electro-optic spatial light modulator from an engineered organic layer," *Nature Communications*, vol. 12, no. 1, Oct. 2021. [Online]. Available: https://doi.org/10.1038/s41467-021-26035-y

[71] J. Gieseler, B. Deutsch, R. Quidant, and L. Novotny, "Subkelvin parametric feedback cooling of a laser-trapped nanoparticle," *Physical Review Letters*, vol. 109, no. 10, Sep. 2012. [Online]. Available: https://doi.org/10.1103/physrevlett.109.103603

[72] G. P. Conangla, F. Ricci, M. T. Cuairan, A. W. Schell, N. Meyer, and R. Quidant, "Optimal feedback cooling of a charged levitated nanoparticle with adaptive control," *Physical Review Letters*, vol. 122, no. 22, Jun. 2019. [Online]. Available: https://doi.org/10.1103/physrevlett.122.223602

[73] D. Windey, C. Gonzalez-Ballestero, P. Maurer, L. Novotny, O. Romero-Isart, and R. Reimann, "Cavity-based 3d cooling of a levitated nanoparticle via coherent scattering," *Physical Review Letters*, vol. 122, no. 12, Mar. 2019. [Online]. Available: https://doi.org/10.1103/physrevlett.122.123601

[74] U. Delić, M. Reisenbauer, D. Grass, N. Kiesel, V. Vuletić, and M. Aspelmeyer, "Cavity cooling of a levitated nanosphere by coherent

scattering," *Physical Review Letters*, vol. 122, no. 12, Mar. 2019. [Online]. Available: https://doi.org/10.1103/physrevlett.122.123602

[75] A. Pontin, H. Fu, M. Toroš, T. S. Monteiro, and P. F. Barker, "Simultaneous cavity cooling of all six degrees of freedom of a levitated nanoparticle," *Nature Physics*, Apr. 2023. [Online]. Available: https://doi.org/10.1038/s41567-023-02006-6

[76] J. Ahn, Z. Xu, J. Bang, Y.-H. Deng, T. M. Hoang, Q. Han, R.-M. Ma, and T. Li, "Optically levitated nanodumbbell torsion balance and GHz nanomechanical rotor," *Physical Review Letters*, vol. 121, no. 3, Jul. 2018. [Online]. Available: https://doi.org/10.1103/physrevlett.121.033603

[77] B. Melo, I. Brandão, R. Rodrigues, A. Khoury, T. Guerreiro *et al.*, "Optical trapping in a dark focus," *Physical Review Applied*, vol. 14, no. 3, p. 034069, 2020.

[78] H. Zhang and K.-K. Liu, "Optical tweezers for single cells," *Journal of the Royal Society interface*, vol. 5, no. 24, pp. 671–690, 2008.

[79] A. Ehrlicher, T. Betz, B. Stuhrmann, D. Koch, V. Milner, M. Raizen, and J. Käs, "Guiding neuronal growth with light," *Proceedings of the National Academy of Sciences*, vol. 99, no. 25, pp. 16 024–16 028, 2002.

[80] A. Blázquez-Castro, "Optical tweezers: Phototoxicity and thermal stress in cells and biomolecules," *Micromachines*, vol. 10, no. 8, p. 507, Jul. 2019. [Online]. Available: https://doi.org/10.3390/mi10080507

[81] P. Xu, X. He, J. Wang, and M. Zhan, "Trapping a single atom in a blue detuned optical bottle beam trap," *Optics Letters*, vol. 35, no. 13, p. 2164, Jun. 2010. [Online]. Available: https://doi.org/10.1364/ol.35.002164

[82] D. Barredo, V. Lienhard, P. Scholl, S. de Léséleuc, T. Boulier, A. Browaeys, and T. Lahaye, "Three-dimensional trapping of individual rydberg atoms in ponderomotive bottle beam traps," *Physical Review Letters*, vol. 124, no. 2, Jan. 2020. [Online]. Available: https://doi.org/10.1103/physrevlett.124.023201

[83] P. Zhang, Z. Zhang, J. Prakash, S. Huang, D. Hernandez, M. Salazar, D. N. Christodoulides, and Z. Chen, "Trapping and transporting aerosols with a single optical bottle beam generated by moiré techniques," *Optics Letters*, vol. 36, no. 8, p. 1491, Apr. 2011. [Online]. Available: https://doi.org/10.1364/ol.36.001491

[84] L. Gong, W. Liu, Q. Zhao, Y. Ren, X. Qiu, M. Zhong, and Y. Li, "Controllable light capsules employing modified bessel-gauss beams," *Scientific reports*, vol. 6, no. 1, pp. 1–12, 2016.

[85] K. A. Hammer, C. F. Carson, and T. V. Riley, "Antimicrobial activity of essential oils and other plant extracts," *Journal of applied microbiology*, vol. 86, no. 6, pp. 985–990, 1999.

[86] S. Lepeshov, N. Meyer, P. Maurer, O. Romero-Isart, and R. Quidant, "Levitated optomechanics with meta-atoms," *arXiv preprint arXiv:2211.08235*, 2022.

[87] J. P. Gordon and A. Ashkin, "Motion of atoms in a radiation trap," *Physical Review A*, vol. 21, no. 5, pp. 1606–1617, May 1980. [Online]. Available: https://doi.org/10.1103/physreva.21.1606

[88] V. Jain, J. Gieseler, C. Moritz, C. Dellago, R. Quidant, and L. Novotny, "Direct measurement of photon recoil from a levitated nanoparticle," *Physical Review Letters*, vol. 116, no. 24, Jun. 2016. [Online]. Available: https://doi.org/10.1103/physrevlett.116.243601

[89] F. Gerbier and Y. Castin, "Heating rates for an atom in a far-detuned optical lattice," *Physical Review A*, vol. 82, no. 1, Jul. 2010. [Online]. Available: https://doi.org/10.1103/physreva.82.013615

[90] M. L. Juan, G. Molina-Terriza, T. Volz, and O. Romero-Isart, "Near-field levitated quantum optomechanics with nanodiamonds," *Physical Review A*, vol. 94, no. 2, Aug. 2016. [Online]. Available: https://doi.org/10.1103/physreva.94.023841

[91] X. Shan, F. Wang, D. Wang, S. Wen, C. Chen, X. Di, P. Nie, J. Liao, Y. Liu, L. Ding *et al.*, "Optical tweezers beyond refractive index mismatch using highly doped upconversion nanoparticles," *Nature Nanotechnology*, vol. 16, no. 5, pp. 531–537, 2021.

[92] M. L. Juan, C. Bradac, B. Besga, M. Johnsson, G. Brennen, G. Molina-Terriza, and T. Volz, "Cooperatively enhanced dipole forces from artificial atoms in trapped nanodiamonds," *Nature Physics*, vol. 13, no. 3, pp. 241–245, 2017.

[93] E. R. Dufresne, G. C. Spalding, M. T. Dearing, S. A. Sheets, and D. G. Grier, "Computer-generated holographic optical tweezer arrays," *Review of Scientific Instruments*, vol. 72, no. 3, p. 1810, 2001. [Online]. Available: https://doi.org/10.1063/1.1344176

[94] I. Brandão, D. Tandeitnik, and G. T, "Coherent scattering-mediated correlations between levitated nanospheres," *Quantum Science and Technology*, vol. 6, no. 4, p. 045013, Sep. 2021. [Online]. Available: https://doi.org/10.1088/2058-9565/ac1a01

[95] J. Rieser, M. A. Ciampini, H. Rudolph, N. Kiesel, K. Hornberger, B. A. Stickler, M. Aspelmeyer, and U. Delić, "Tunable light-induced dipole-dipole interaction between optically levitated nanoparticles," *Science*, vol. 377, no. 6609, pp. 987–990, Aug. 2022. [Online]. Available: https://doi.org/10.1126/science.abp9941

[96] C. Arbore, L. Perego, M. Sergides, and M. Capitanio, "Probing force in living cells with optical tweezers: from single-molecule mechanics to cell mechanotransduction," *Biophysical Reviews*, vol. 11, no. 5, pp. 765–782, Oct. 2019. [Online]. Available: https://doi.org/10.1007/s12551-019-00599-y

[97] T. Boothe, L. Hilbert, M. Heide, L. Berninger, W. B. Huttner, V. Zaburdaev, N. L. Vastenhouw, E. W. Myers, D. N. Drechsel, and J. C. Rink, "A tunable refractive index matching medium for live imaging cells, tissues and model organisms," *eLife*, vol. 6, Jul. 2017. [Online]. Available: https://doi.org/10.7554/elife.27240

[98] J. Pine, "Recording action potentials from cultured neurons with extracellular microcircuit electrodes," *Journal of Neuroscience Methods*, vol. 2, no. 1, pp. 19–31, Feb. 1980. [Online]. Available: https://doi.org/10.1016/0165-0270(80)90042-4

[99] C. Liang, Y. Liu, W. Lu, G. Tian, Q. Zhao, D. Yang, J. Sun, and D. Qi, "Strategies for interface issues and challenges of neural electrodes," *Nanoscale*, vol. 14, no. 9, pp. 3346–3366, 2022. [Online]. Available: https://doi.org/10.1039/d1nr07226a